

LOCAL DISPLACEMENTS AND LOAD TRANSFER
OF SHAPE MEMORY ALLOYS IN POLYMERIC MATRICES

BY

KRISHNA D. JONNALAGADDA

B.Tech., Institute of Technology, Banaras Hindu University, 1991
M.S., University of Kentucky, 1993

THESIS

Submitted in partial fulfillment of the requirements
for the degree of Doctor of Philosophy in Theoretical and Applied Mechanics
in the Graduate College of the
University of Illinois at Urbana-Champaign, 1997

Urbana, Illinois

Report Documentation Page

Form Approved
OMB No. 0704-0188

Public reporting burden for the collection of information is estimated to average 1 hour per response, including the time for reviewing instructions, searching existing data sources, gathering and maintaining the data needed, and completing and reviewing the collection of information. Send comments regarding this burden estimate or any other aspect of this collection of information, including suggestions for reducing this burden, to Washington Headquarters Services, Directorate for Information Operations and Reports, 1215 Jefferson Davis Highway, Suite 1204, Arlington VA 22202-4302. Respondents should be aware that notwithstanding any other provision of law, no person shall be subject to a penalty for failing to comply with a collection of information if it does not display a currently valid OMB control number.

1. REPORT DATE

1997

2. REPORT TYPE

3. DATES COVERED

00-00-1997 to 00-00-1997

4. TITLE AND SUBTITLE

Local Displacements and Load Transfer of Shape Memory Alloys in Polymeric Matrices

5a. CONTRACT NUMBER

5b. GRANT NUMBER

5c. PROGRAM ELEMENT NUMBER

6. AUTHOR(S)

5d. PROJECT NUMBER

5e. TASK NUMBER

5f. WORK UNIT NUMBER

7. PERFORMING ORGANIZATION NAME(S) AND ADDRESS(ES)

University of Illinois at Urbana-Champaign, Department of Theoretical and Applied Mechanics, Urbana, IL, 61801

8. PERFORMING ORGANIZATION REPORT NUMBER

9. SPONSORING/MONITORING AGENCY NAME(S) AND ADDRESS(ES)

10. SPONSOR/MONITOR'S ACRONYM(S)

11. SPONSOR/MONITOR'S REPORT NUMBER(S)

12. DISTRIBUTION/AVAILABILITY STATEMENT

Approved for public release; distribution unlimited

13. SUPPLEMENTARY NOTES

14. ABSTRACT

Shape memory alloy (SMA) materials can be embedded in a host matrix to induce active shape control, alter the stiffness, or change the modal response and provide vibration control. The interaction between the SMA and the host material is critical to applications requiring transfer of loads or strain from the SMA to the host. Although there has been a significant amount of research dedicated to the characterizing and modeling of SMAs alone little research has been focused on the transformation behavior of embedded SMAs. The phase transformation in an SMA is a function of both stress and temperature. Since an SMA in a composite is subject to a complex stress field by the surrounding matrix, the embedded behavior is significantly different from that of a free SMA. Various experimental techniques were utilized to obtain insight into the behavior of embedded SMAs and to provide quantitative data for evaluation of theoretical models. Average interfacial bond strength between an embedded SMA and an epoxy matrix were measured using pullout tests. The effects of various mechanical and chemical surface treatments on the bond strengths were examined. In-situ out-of-plane displacements of two-way trained SMA wires in epoxy were measured using heterodyne microinterferometry. The interfacial bond strengths from the pullout tests were correlated with the maximum wire displacements. The transient load transfer behavior of a one-way SMA ribbon in a room temperature cured polymer matrix was quantified using twodimensional photoelasticity. The effects of residual stress were examined using high temperature cured matrices. In-plane displacements of room temperature cured SMA ribbon composites were obtained using moiré interferometry. Displacements due to thermal expansion were separated from displacements due to SMA actuation. An experimental value for the velocity of propagation of the SMA actuation front was calculated. A finite element model based on one-dimensional constitutive equations was developed for ribbon composites. Displacements and stresses in the ribbon were compared with experimental values.

15. SUBJECT TERMS

16. SECURITY CLASSIFICATION OF:			17. LIMITATION OF ABSTRACT Same as Report (SAR)	18. NUMBER OF PAGES 173	19a. NAME OF RESPONSIBLE PERSON
a. REPORT unclassified	b. ABSTRACT unclassified	c. THIS PAGE unclassified			

Standard Form 298 (Rev. 8-98)
Prescribed by ANSI Std Z39-18

LOCAL DISPLACEMENTS AND LOAD TRANSFER OF SHAPE MEMORY ALLOYS IN POLYMERIC MATRICES

Krishna D. Jonnalagadda, Ph.D.
Department of Theoretical and Applied Mechanics
University of Illinois at Urbana-Champaign, 1997
Nancy R. Sottos, Advisor

ABSTRACT

Shape memory alloy (SMA) materials can be embedded in a host matrix to induce active shape control, alter the stiffness, or change the modal response and provide vibration control. The interaction between the SMA and the host material is critical to applications requiring transfer of loads or strain from the SMA to the host. Although there has been a significant amount of research dedicated to the characterizing and modeling of SMAs alone, little research has been focused on the transformation behavior of embedded SMAs. The phase transformation in an SMA is a function of both stress and temperature. Since an SMA in a composite is subject to a complex stress field by the surrounding matrix, the embedded behavior is significantly different from that of a free SMA. Various experimental techniques were utilized to obtain insight into the behavior of embedded SMAs and to provide quantitative data for evaluation of theoretical models.

Average interfacial bond strength between an embedded SMA and an epoxy matrix were measured using pullout tests. The effects of various mechanical and chemical surface treatments on the bond strengths were examined. In-situ out-of-plane displacements of two-way trained SMA wires in epoxy were measured using heterodyne microinterferometry. The interfacial bond strengths from the pullout tests were correlated with the maximum wire displacements. The transient load transfer behavior of a one-way SMA ribbon in a room temperature cured polymer matrix was quantified using two-dimensional photoelasticity. The effects of residual stress were examined using high

temperature cured matrices. In-plane displacements of room temperature cured SMA ribbon composites were obtained using moiré interferometry. Displacements due to thermal expansion were separated from displacements due to SMA actuation. An experimental value for the velocity of propagation of the SMA actuation front was calculated. A finite element model based on one-dimensional constitutive equations was developed for ribbon composites. Displacements and stresses in the ribbon were compared with experimental values.

ACKNOWLEDGMENTS

I would like to acknowledge the financial support provided by the of the Office of Naval Research (under contract monitor R. Barsoum).

I would like to express my appreciation and gratitude to my advisor, Prof. Nancy R. Sottos, for her advice, encouragement and patience throughout the course of my research and graduate studies. In addition to guiding me through the technical aspects of the research, Professor Sottos taught me the importance of persistence, thoroughness and originality in research. I wish to thank Prof. Scott R. White for his advice and guidance. His insight into the behavior of shape memory alloys was extremely helpful in interpreting experimental data. I would also like to thank Prof. James W. Phillips for serving on my dissertation committee.

I would like to thank my parents, whose love and support have always been my greatest assets. Finally, I wish to thank my friends Venkat, Dinesh, Sandhya, Ravi, Raj, and most of all Aarti, for their continued support and encouragement.

TABLE OF CONTENTS

LIST OF TABLES	viii
LIST OF FIGURES	ix
1. INTRODUCTION	1
1.1 Shape Memory Effect	1
1.2 Shape Memory Alloy Composites	5
1.2.1 Background	5
1.2.2 SMA/Host Interaction	7
1.2.3 Residual Stresses	8
1.2.4 Constitutive Behavior	8
1.3 Project Overview	10
2. SMA/POLYMER ADHESION	13
2.1 Introduction	13
2.2 Pullout Tests	13
2.3 Sample Preparation	15
2.4 Effects of Surface Treatments	16
2.5 Conclusions	21
3. OUT-OF-PLANE DISPLACEMENT	22
3.1 Introduction	22
3.2 Microinterferometric Method	23
3.2.1 Apparatus	23
3.2.2 Principle of Operation	27
3.3 Transient Displacement Measurements—150 μ m wires	29
3.3.1 Sample Preparation	29
3.3.2 Displacement Measurements	33
3.4 Transient Displacement Measurements—50 μ m wires	39
3.5 Conclusions	49
4. LOAD TRANSFER	50
4.1 Introduction	50
4.2 Experimental Setup	50
4.3 Load Transfer—High Temperature Cure Matrix	52
4.3.1 Sample Preparation	52
4.3.2 Sample Actuation and Discussion	55
4.4 Load Transfer—Room Temperature Cure Matrix	63
4.4.1 Sample Preparation	65
4.4.2 Heating and Actuation	65
4.4.3 Experimental Stress Analysis	69
4.5 Conclusions	76
5. IN-PLANE DISPLACEMENTS	77
5.1 Principle of Moiré Interferometry	77
5.2 Sample Preparation	83
5.3 Experimental Setup and Procedure	87
5.4 Displacement Measurements Using Moiré Interferometry	90
5.4.1 Temperature Measurements	90
5.4.2 Steady State Displacements	92

5.4.3	Transient Displacements	108
5.5	Conclusions	119
6.	COMPARISON WITH THEORETICAL MODELS	120
6.1	Overview of constitutive models	120
6.2	1-D Constitutive Model	122
6.2.1	General Formulation	122
6.2.2	Adaptation Embedded SMA	128
6.3	Finite Element Analysis	128
6.3.1	Solution Procedure	128
6.3.2	Analysis and Discussion	134
6.4	Conclusions	144
7.	CONCLUSIONS AND FUTURE WORK	146
7.1	Conclusions	146
7.2	Future Work	149
	BIBLIOGRAPHY	152
	VITA	162

LIST OF TABLES

Table 1.1	Average interfacial debond strength for different surface treatments.....	20
Table 3.1	Material properties for epoxy matrix and SMA wire.....	31
Table 3.2	Maximum displacements of embedded wires with various surface treatments.	41
Table 4.1	Material properties of SMA ribbon in austenitic and martensitic phases.....	54
Table 4.2	Material properties of high temperature and room temperature cure polymer matrices.....	68

LIST OF FIGURES

Figure 1.1	Schematic of crystal orientations during shape memory behavior.....	2
Figure 1.2	One-way and two-way effects in shape memory alloys.....	4
Figure 1.3	Effect of applied stress on SMA transformation behavior.....	6
Figure 2.1	Schematic of typical pullout test.....	14
Figure 2.2	A typical experimental pullout curve for an SMA sample.....	17
Figure 2.3	Comparison of interfacial debond strengths for different surface treatments.	19
Figure 3.1	Schematic of heterodyne interferometric setup.....	24
Figure 3.2	Schematic of the signal processing apparatus.....	26
Figure 3.3	Schematic of the displacement and optical path relation.....	28
Figure 3.4	Schematic of 150 μm sample with dimensions $d = 32$ mm, $h_1 = 2$ mm and $h_2 = 15$ mm.....	30
Figure 3.5	Temperature profile adjacent to SMA wire during heating.....	34
Figure 3.6	Typical transient displacement curve for embedded 150 μm SMA wire in epoxy.....	36
Figure 3.7	Transient displacement behavior of 150 μm embedded SMA wire upon heating and cooling.....	37
Figure 3.8	Repeatability of normalized displacements of embedded, untreated, 50 μm wires in epoxy.....	38
Figure 3.9	Maximum displacement of SMA wire for different surface treatments	40
Figure 3.10	Photoelastic image of sectioned 150 μm wire sample without embedded lead wire, showing a negligible stress field.....	42
Figure 3.11	Photoelastic image of sectioned 150 μm wire sample with embedded lead wire, showing stress concentration around the lead.....	43
Figure 3.12	Schematic of 50 μm sample.....	45
Figure 3.13	Transient displacement profiles of annealed and embedded	

	50 μm SMA wires.....	47
Figure 3.14	Transient displacement profiles of two-way trained and embedded 50 μm SMA wires.....	48
Figure 4.1	Schematic of circular polariscope.....	51
Figure 4.2	Schematic of photoelastic sample.....	53
Figure 4.3	Schematic description of thermal contraction on cooling from a cure temperature of 150°C to a room temperature of 25°C.....	56
Figure 4.4	Photoelastic images of aluminum ribbon sample at different temperatures: (a) $T = 25^\circ\text{C}$ and (b) $T = 45^\circ\text{C}$	58
Figure 4.5	Photoelastic images of processed SMA sample at different temperatures: (a) $T = 25^\circ\text{C}$ and (b) $T = 80^\circ\text{C}$	59
Figure 4.6	Photoelastic images of annealed SMA sample at different temperatures: (a) $T = 25^\circ\text{C}$, (b) $T = 50^\circ\text{C}$ and (c) $T = 80^\circ\text{C}$	61
Figure 4.7	Schematic description of the effect of actuation in high temperature cure SMA ribbon composites.....	62
Figure 4.8	Photoelastic images of two-way trained sample at different temperatures: (a) $T = 25^\circ\text{C}$, (b) $T = 50^\circ\text{C}$ and (c) $T = 80^\circ\text{C}$	64
Figure 4.9	Heating of SMA ribbons: (a) Infrared image of SMA ribbon sample; (b) Temperature profile along sample in isotherm units.....	66
Figure 4.10	Temperature profile on the SMA sample surface adjacent to the ribbon during heating and cooling.....	67
Figure 4.11	Photoelastic images of room temperature cured SMA ribbon composites at various times: (a) $t = 0$; (b) $t = 120$ s; (c) $t = 240$ s.....	70
Figure 4.12	(a) Photoelastic stress contours for 1% prestrained sample at time $t = 0$; (b) Locations of stress contours for the symmetric top half of the photoelastic image.....	71
Figure 4.13	(a) Photoelastic stress contours for 1% prestrained sample at time $t = 60$ s;	

	(b) Locations of stress contours for the symmetric top half of the photoelastic image.....	72
Figure 4.14	(a) Photoelastic stress contours for 1% prestrained sample at time $t = 120$ s; (b) Locations of stress contours for the symmetric top half of the photoelastic image.....	73
Figure 4.15	(a) Photoelastic stress contours for 1% prestrained sample at time $t = 180$ s; (b) Locations of stress contours for the symmetric top half of the photoelastic image.....	74
Figure 4.16	(a) Photoelastic stress contours for 1% prestrained sample at time $t = 240$ s; (b) Locations of stress contours for the symmetric top half of the photoelastic image.....	75
Figure 5.1	Diffraction from a reflective grating.....	78
Figure 5.2	Principle of moiré interferometry.....	80
Figure 5.3	Change in optical path length with deformation: (a) Wavefront 1; (b) Wavefront 2.....	81
Figure 5.4	Schematic of sample for moiré interferometry.....	84
Figure 5.5	Photograph of grating separation fixture.....	86
Figure 5.6	Schematic illustration of the moiré interferometer.....	88
Figure 5.7	Schematic illustration of sample fixtures.....	89
Figure 5.8	Temperature profiles of the sample surface at different power inputs.....	91
Figure 5.9	Moiré images of annealed ribbon sample with a power input of 1.50 A: (a) Prior to heating; (b) At steady state temperature; and (c) After cooldown.....	93
Figure 5.10	Displacement profile of annealed SMA ribbon with a current input of 1.50 A at steady state temperature.....	94
Figure 5.11	Moiré images of 1% prestrained ribbon sample with a current input of 1.50 A: (a) Prior to heating; (b) At steady state temperature; and	

	(c) After cooldown.....	96
Figure 5.12	Displacement profiles of 1% prestrained SMA ribbon with a current input of 1.50 A at steady state temperature and after cooldown.....	97
Figure 5.13	(a) Axial stress in embedded SMA ribbon on heating; (b) Effect of applied stress on transformation temperatures of SMA ribbons.....	99
Figure 5.14	Moiré images of 1% prestrained ribbon sample at steady state temperature for different current inputs: (a) $I = 1.50$ A; (b) $I = 1.55$ A; and (c) $I = 1.65$ A.....	101
Figure 5.15	Displacement profiles of 1% prestrained SMA ribbons at steady state temperature for different current inputs.....	102
Figure 5.16	Moiré images of 1% prestrained ribbon sample after cooldown for different current inputs: (a) $I = 1.50$ A; (b) $I = 1.55$ A; and (c) $I = 1.65$ A.....	103
Figure 5.17	Displacement profiles of 1% prestrained SMA ribbons after cooldown for different current inputs.....	104
Figure 5.18	Schematic of displacements in prestrained SMA ribbon sample: (a) Prior to heating; (b) At steady state temperature; and (c) After cooldown	106
Figure 5.19	The stress–strain curve of a typical shape memory alloy at $M_s < T < A_s$	107
Figure 5.20	Transient moiré images of 1% prestrained ribbon sample with a current input of 1.50 A: (a) $t = 0$; (b) $t = 15$ s; (c) $t = 30$ s.....	110
Figure 5.20	Transient moiré images of 1% prestrained ribbon sample with a current input of 1.50 A: (d) $t = 45$ s; (e) $t = 60$ s; (f) $t = 75$ s.....	111
Figure 5.20	Transient moiré images of 1% prestrained ribbon sample with a current input of 1.50 A: (g) $t = 90$ s; (h) $t = 105$ s; (i) $t = 120$ s.....	112
Figure 5.20	Transient moiré images of 1% prestrained ribbon sample with a current input of 1.50 A: (j) $t = 135$ s; (k) $t = 150$ s; (l) $t = 165$ s.....	113
Figure 5.20	Transient moiré images of 1% prestrained ribbon sample with a current input of 1.50 A: (m) $t = 180$ s; (n) $t = 195$ s; (o) $t = 210$ s.....	114

Figure 5.20	Transient moiré images of 1% prestrained ribbon sample with a current input of 1.50 A: (p) $t = 210$ s; (q) $t = 240$ s.....	115
Figure 5.21	Change in location of the saddle point with time for SMA ribbon sample with a power input 1.50 A.....	116
Figure 5.22	Transient moiré images of 1% prestrained ribbon sample reheated with a power input of 1.55 A: (a) $t = 0$; (b) $t = 10$ s; and (c) $t = 60$ s.....	118
Figure 6.1	Schematic of sample geometry and boundary conditions for the thermal problem.....	130
Figure 6.2	Finite element mesh for quarter-symmetric ribbon composite.....	131
Figure 6.3	Contours of constant temperature contours at steady state.....	132
Figure 6.4	Schematic of sample geometry and boundary conditions for the mechanical problem.....	133
Figure 6.5	Schematic of finite element solution procedure for SMA ribbon composites.....	135
Figure 6.6	Comparison of experimental and finite element displacement profiles at a steady state temperature of 44°C	136
Figure 6.7	Displacement profiles along SMA ribbon for different steady state temperatures.....	139
Figure 6.8	Stress contours along SMA ribbon for different steady state temperatures.....	140
Figure 6.9	Displacement profiles along SMA ribbon for different stress–temperature coefficients.....	141
Figure 6.10	Displacement profiles along SMA ribbon or different values of the coefficient of thermal expansion.....	143

1. INTRODUCTION

1.1 Shape Memory Effect

The shape memory effect was first observed in nickel–titanium alloys of nearly equiatomic composition by Buehler and co-workers of the Naval Ordnance Labs in 1962 (Melton, 1989).^{*} Since then, other shape memory alloys (SMAs) such as Cu-Zn-Al alloys have been discovered, although Ni-Ti alloys are still used for most applications. Shape memory materials undergo a diffusionless, isochoric, solid–solid transformation between an austenite and a martensite phase (Wayman, 1989). When heated, a shape memory alloy transforms to the austenite phase, which has a body center cubic (BCC) microstructure. Upon cooling, the SMA transforms to a martensite phase with a less rigid monoclinic structure, which permits the coexistence of multiple variants of martensite.

The transformation involves two processes—the Bain strain and the lattice-invariant shear. The Bain strain incorporates small movements of atoms needed to produce the new crystal structure of martensite. The lattice-invariant shear mechanism accommodates the different shape of the new martensite within the transformed austenite. The uniqueness of shape memory lies in the fact that the lattice-invariant shear step of this transformation occurs almost solely by twinning (Wayman, 1989). Twinning forces the BCC shape into a monoclinic phase with no volume change and no broken bonds. The tilted monoclinic shape forms alternate bands, producing a herringbone effect. When stress is applied to this structure, the alternate bands align in the same direction by a process called detwinning. When the material is again heated to the austenitic phase, the detwinned crystal structure transforms back to BCC austenite and regains its original shape. The transformation and reorientation are shown schematically in Figure 1.1. Because no slip or dislocation

^{*} References are listed alphabetically by author at the end of the thesis, beginning on page 149.

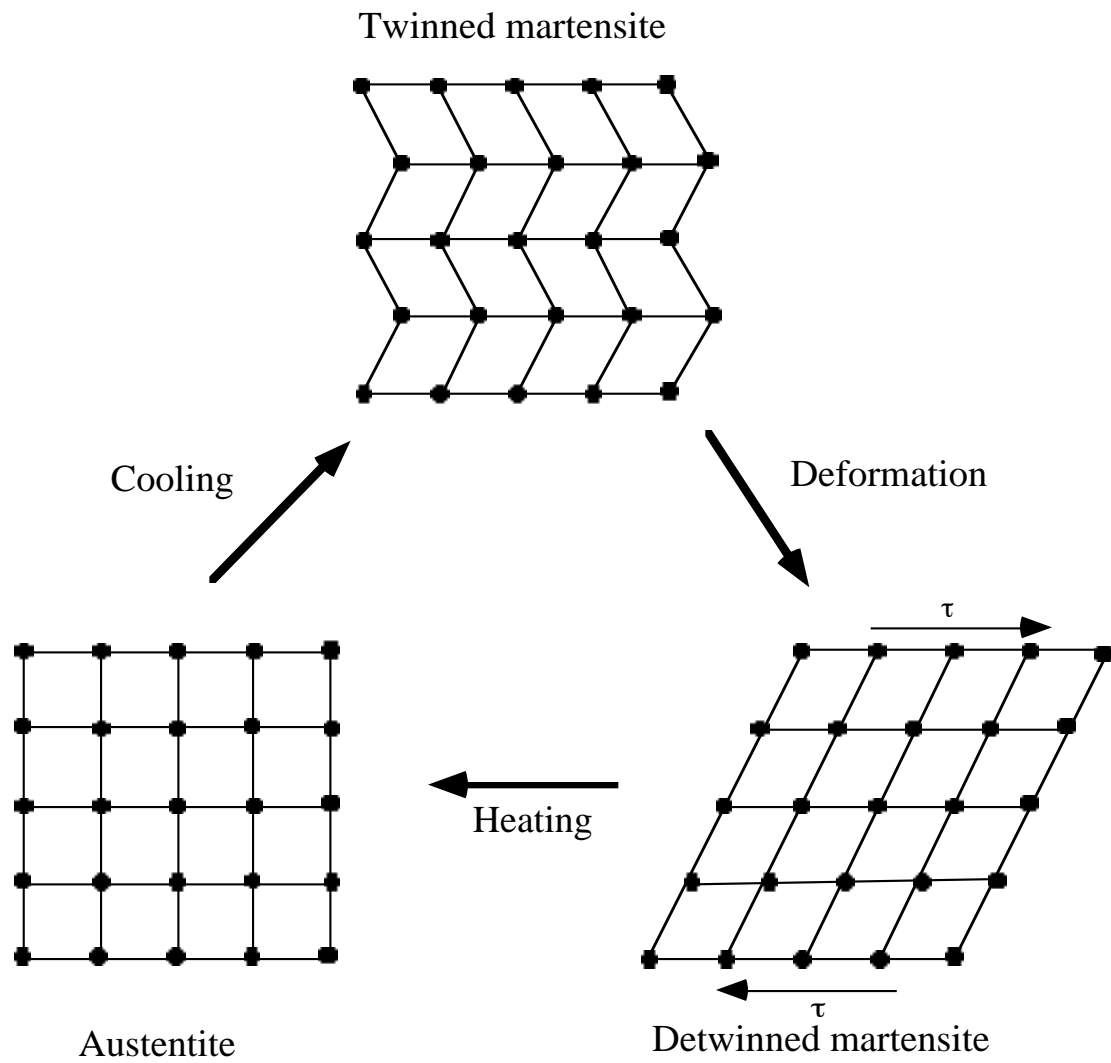


Figure 1.1. Schematic of crystal orientations during shape memory behavior.

entanglements have been introduced into the microstructure during the cooling or deformation stage, the process is completely reversible.

Shape memory behavior can be classified into two distinct categories based on material response to thermal cycling. One-way shape memory occurs when an SMA is deformed at its martensitic temperature and, upon heating to an austenitic temperature, changes back to its original shape, eliminating the original deformation. In order to change back to the deformed configuration, mechanical loading is required. A two-way shape memory effect can be induced by cyclic thermomechanical transformation training of the SMA (Perkins and Hodgson, 1989). Training creates a favorable residual stress field that leads to a reversible martensite-austenite transformation. Stress-free cooling of the austenite produces a transformation strain that is hysteretically recovered during stress-free heating of the martensite as shown schematically in Figure 1.2. The significant transformation temperatures representing the start and finish of transformation are austenite finish (A_f), austenite start (A_s), martensite start (M_s) and martensite finish (M_f). Two-way trained wires have two inherent advantages. First, the transformation cycles from martensite-to-austenite and vice-versa are repeatable, thereby providing multiple readings from the same sample. Secondly, most matrix materials used in practice need to be cured at elevated temperatures, which would actuate the one-way wires, making them useless for testing. Hence, fabrication of SMA composites can be greatly simplified by using the two-way shape memory effect (Hebda et al., 1995). The disadvantage however, is that with increasing cross-sectional area, it becomes harder to train the wires due to a size effect. Further, the recoverable strain in two-way trained SMAs is about 2% while one-way wires can recover as much as 8% strain.

Applied stress has a significant effect on the transformation characteristics of shape memory alloys (Schuerch, 1968). In martensitic transformations, there is an equivalence

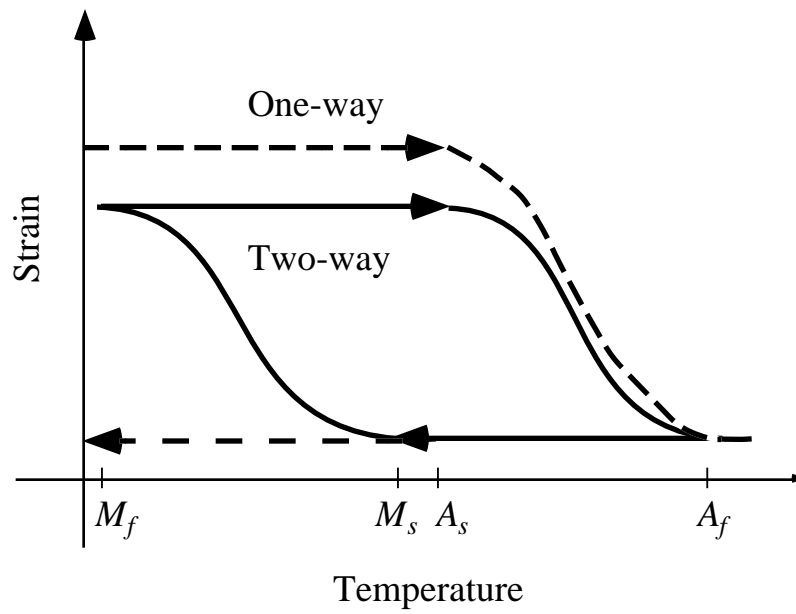


Figure 1.2. One-way and two-way effects in shape memory alloys.

between stress and temperature. A decrease in temperature is equivalent to an increase in stress, both stabilizing martensite. The transformation temperatures increase approximately linearly with applied stress as shown schematically in Figure 1.3 (Wayman, 1989). The slopes C_M and C_A are called the stress–temperature coefficients for martensite and austenite, respectively. The linear behavior is observed until a stress level is reached where the moving of dislocations in the crystal structure becomes energetically more favorable to forming stress-induced martensite and plastic deformation follows.

1.2 Shape Memory Alloy Composites

1.2.1 Background

Since around 1990, there has been considerable interest in the area of SMA composites. Since SMAs are characterized by large actuation strains, they were envisioned for active shape control of a structure by actuating embedded wires, films, or ribbons. An example for application of SMA composites is to change the shape of an graphite/epoxy aircraft wing. A particular wing shape is ideal for take-off and landing of an aircraft while a different shape is optimal at cruise speeds. Embedded SMAs could be used to change the shape of the wing mid-flight depending on the flight conditions. Initially, manufacturing and processing difficulties hampered the development of SMA composites. Attempts by Liang, Jia and Rogers (1989) to embed nitinol wires into polymers proved largely unsuccessful due to poor interfacial bonding. Subsequently, Baz and Ro (1992) and Chaudry and Rogers (1991) incorporated SMA wires using coupling sleeves and mechanical fasteners, respectively. Paine and Rogers (1991) studied the effects of processing on the performance of SMA actuators in composites. Hebda et al. (1995) examined issues in manufacturing, such as void content and SMA training effects. This work demonstrated that the reversibility of two-way shape memory effect leads to a much simpler fabrication procedure for an SMA composite. With two-way trained wires, there is no need to constrain the wires during cure or use sleeves. The unrestrained wires undergo

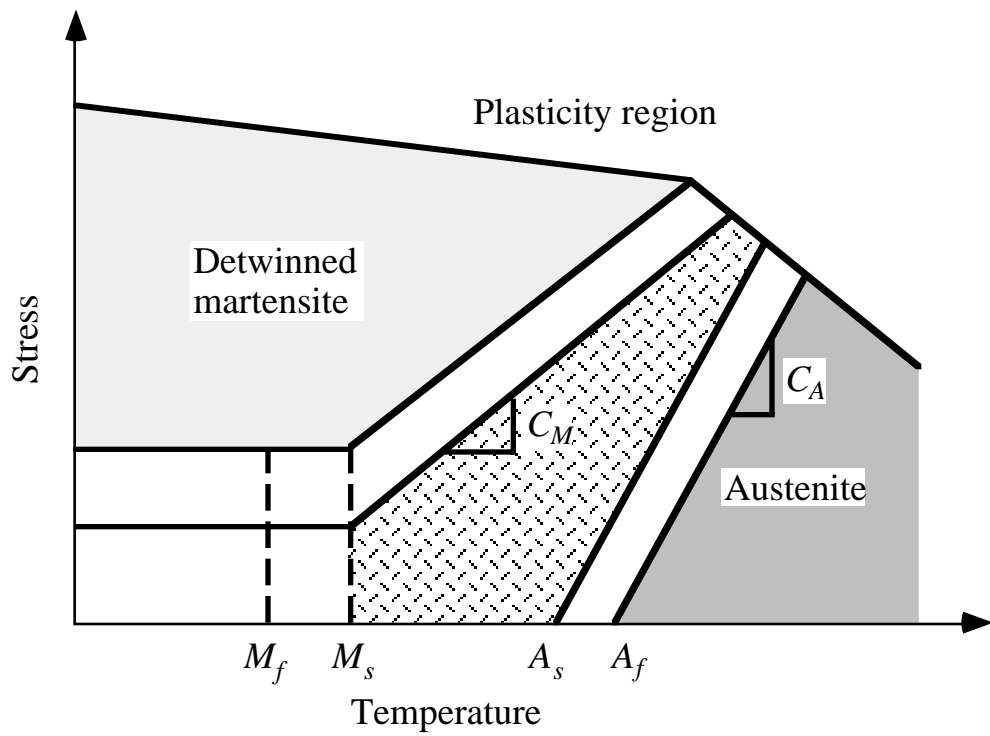


Figure 1.3. Effect of applied stress on SMA transformation behavior.

martensite-to-austenite transformation after the processing temperature rises above A_s , while during cooldown from the cure temperature the reverse transformation is initiated. The strains that occur as a result of the austenite-to-martensite transformation lead to the development of residual stresses that can be relieved by heating the laminate and the wires. After cure, the wires can be cycled between austenite and martensite by thermal and mechanical loading.

1.2.2 *SMA/Host Interaction*

Although there has been a significant amount of research dedicated to the characterizing and modeling of SMAs alone, little work has been done to understand the behavior of SMAs in composites. The interaction between the embedded SMA and the host material is critical since most applications require transfer of load or strain from the wire to the host. Paine, Jones and Rogers (1992) have asserted the importance of interfacial adhesion between embedded SMA wires and the host material. When the SMA wires are actuated, large shear strains are generated at the SMA/host interface. The stronger the interface, the greater the transfer of strain from the actuator to the host material.

Just as for a structural composite, the interface between the embedded SMA and the surrounding matrix has a significant effect on the overall response. A higher interfacial bond strength facilitates greater load transfer to the host material and therefore, increased response of the composite structure. Paine and Rogers (1993) demonstrated that the interfacial adhesion between the SMA and a polymeric host material was largely mechanical. However, a comprehensive study of the effect of different surface treatments is lacking and needs to be addressed. Further, Bidaux et al. (1993) measured significant differences in dynamic behavior between plain SMA wires and SMAs in polymer composites. This change in response was analyzed in terms of the SMA/matrix interaction.

1.2.3 *Residual Stresses*

An additional complication with SMA composites is that the embedded SMAs are usually subjected to a multiaxial residual stress field upon curing. The effect of a uniaxial stress field on the transformation temperatures is shown in Figure 1.3 but studies on the effect of a multiaxial stress field on an SMA are unavailable in the literature. Accurate predictions of the embedded behavior are therefore difficult. For example, the embedded SMA may not uniformly recover the prestrain due to the constraint of the matrix. The stress applied by the surrounding matrix on the wire due to partial actuation might be adequate to shift the transformation temperatures enough to prevent further transformation of the SMA. Bidaux et al. (1993) observed changes in the dynamic behavior only at the ends of an actuated composite, indicating that the whole wire might not be transforming. Paine and Rogers (1993) recently reported that process-induced residual stresses alter the martensite and austenite start temperatures of SMA wires embedded in an elastomeric composite. Hebda et al. (1995) have also discussed the issue of local residual stresses with regard to manufacturing high quality SMA composites.

1.2.4 *Constitutive Behavior*

In recent years, a number of constitutive models have been developed for SMAs. Most of the available models describe 1-D behavior although a few 3-D models have been recently developed. A whole class of 1-D models are based on pioneering work by Tanaka (1985), who derived the constitutive relations of an SMA from continuum mechanics and thermodynamics. An exponential function was assumed to describe the transformation hysteresis. Müller (1989) used statistical mechanics to model the constitutive behavior. Ortin (1989) adopted the Preisach (1935) phenomenological approach to describe pseudoelasticity. Boyd and Lagoudas (1995a) derived a model that introduces a transformation surface that expands or contracts based on the applied load and temperature. A more detailed discussion of these models is deferred to Chapter 6. Most of the models

have not yet been adapted to study composite behavior. To the author's knowledge, only Boyd and Lagoudas (1995b) have attempted to modify their model to study composite behavior.

Since the discovery of nitinol, a large volume of literature has been devoted to the experimental characterization of pristine shape memory alloys. Buehler, Gilfritch and Riley (1963) examined the physical properties of nitinol. Jackson, Wagner and Wasilewski (1972) and Ling and Kaplow (1981) studied the metallurgy of the material. Goldstein, Kabacoff and Tydings (1987) examined the effect of stress on phase transformations. Miyazaki (1989) studied the thermal cycling effects and fatigue properties of SMAs. Otsuka (1989) worked on the *R*-phase transitions. Shaw and Kyriakides (1995) observed the phase transformation fronts and the effects of stress, temperature and strain rate on the nucleation and travel of the transformation fronts. There is, however, a limited amount of literature available on the experimental characterization of SMA composites. Paine and Rogers (1991, 1993) studied the effect of adhesion on load transfer in graphite/epoxy and APC-2 composites as well as the effects of processing on composite behavior. Investigation of the in-situ behavior of SMA composites and acquisition of data for comparison with theoretical models are topics that need to be examined.

The transient behavior of SMA composites also presents an unexplored area of research. The SMA transformation is athermal, in the sense that the amount of transformation is dependent only on the current temperature and is independent of the amount of time at a given temperature. The speed of the transformation front is limited only by the speed of sound. The transformation temperatures, and therefore the amount of transformation at a particular temperature, are functions of the surrounding stress field. Shape memory alloys are often used for step load applications to change the shape or stiffness of the structure. In a composite however, the stress state changes continuously as

the SMA is actuated. Understanding the transient behavior of the SMA composite is important for designing a structure with a given response time for a step load. Also, in two way trained wires, the thermal and recovery strains could be of the same order of magnitude, though usually opposite in direction. It is essential to understand the response time for each type of strain for a given power input. Such measurements have to be made with non-contact techniques since any applied load changes the stress state and therefore the transformation behavior of the SMA.

1.3 Project Overview

Since SMA composites represent a relatively recent field of study, there are a number of unresolved issues regarding their behavior. Strain and load transfer capability of an SMA to the surrounding matrix is of critical importance in most applications since SMAs are used primarily as actuators. The amount of load transfer is usually determined by the strength of the SMA/polymer interface. Little experimental data are available regarding the interfacial adhesion between SMAs and polymers. Mechanisms to improve adhesion need to be studied. Shape memory alloys are actuated thermally and therefore an understanding of the interaction between the thermal and SMA strains is necessary to predict the actuation behavior. Thermal strains assume greater importance in polymer composites, which can have large coefficients of thermal expansion. Further, there is also a lack of experimental data with which to compare theoretical models, particularly with regard to the amount of load transfer and the local displacements in SMA composites.

The first objective of the current work was to study the effect of various surface treatments on the interfacial bond strength of the SMA composite. A high bond strength is desirable for most actuator applications, although a lower bond strength might be beneficial in some sensor applications. The strength of the interface was determined using pullout tests, and the results are discussed in Chapter 2. Prior to embedding, SMA wires were

subjected to various chemical, mechanical and plasma surface treatments and their effect on the interfacial bond strength was observed.

In Chapter 3, heterodyne microinterferometry is used to determine the in-situ out-of-plane displacements of two-way trained SMA wires in a polymer. Transient measurements of wire displacement were made in order to obtain a qualitative understanding of the rate at which thermal and SMA displacements occur. The effect of selected surface treatments on the displacement of the wires was determined and compared with the results of the interfacial bond strength obtained from the pullout tests.

Photoelasticity was utilized to study the load transfer characteristics of SMA composites and the results are discussed in Chapter 4. Sandblasted ribbons were embedded in a polymer and quantitative measurements of the load transfer to the matrix when the ribbon is actuated were obtained. The objective was to provide a set of experimental results for transient load transfer in SMA composites. Currently, there are hardly any experimental data to compare with theoretical models of SMA composites. The data in Chapter 4 are designed to serve as a benchmark for future theoretical calculations.

Chapter 5 deals with the application of moiré interferometry to obtain the transient in-plane displacements of SMA ribbon composites. Whole-field displacement measurements of an SMA ribbon in a polymer matrix are made. Thermal and SMA effects are determined independently and correlated. The displacements also provide data to compare with theoretical models.

In Chapter 6, the 1-D constitutive model of Liang and Rogers (1991) is applied to SMA ribbon composites. A discussion on the various theoretical models currently

available in the literature is included. Numerical values are compared with experimental data for load transfer and displacements.

Finally, Chapter 7 summarizes the important conclusions of the current work. Recommendations for future work are also presented.

2. SMA/POLYMER ADHESION

2.1 Introduction

Most SMA composite applications require transfer of strain from the wire to the matrix. In these applications, maximum interfacial adhesion between the SMA wire and the polymer matrix is highly desirable. A strong interfacial bond also increases the structural integrity of the final composite. Therefore, it is essential to have some measure of the interfacial bond strength between the SMA wire and host matrix for the evaluation of mechanical response and the development of well designed interfaces. Adhesive strength is commonly regarded as the mechanical resistance to separation of the adhesive from the substrate. Interfacial adhesion can be attributed to five main mechanisms (Wake, 1978). These include adsorption and wetting, interdiffusion, electrostatic attraction, chemical bonding, and mechanical interlocking. Due to the nature of these mechanisms, adhesive failure normally proceeds in a weak boundary layer or interface region near a polymer/solid interface. The level of adhesion can be controlled by applying an appropriate surface treatment to alter this interface region.

2.2 Pullout Tests

There are a number of testing methods designed to determine the interfacial shear strength of composites. Most methods involve pulling or pushing on one fiber or a number of fibers in a composite section in the direction parallel to the fibers. Some of the better known methods include the single fiber critical length test (Drzal et al., 1980), fiber pushout test (Laughner et al., 1988), microdrop test (Miller, Muri and Rebenfield, 1987), and the fiber pullout test, discussed below.

The single fiber pullout test is one of the simplest tests devised to determine the interfacial shear strength of the fiber-matrix interface. A schematic of a typical pullout test

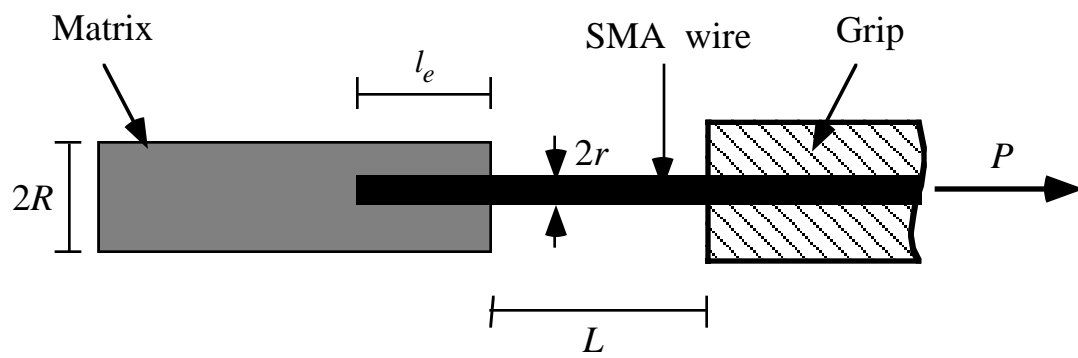


Figure 2.1. Schematic of typical pullout test.

is shown in Figure 2.1. A length l_e of the fiber is embedded in the matrix. The free length L of the fiber between the matrix and the grips is an important parameter that determines whether the fiber breaks or pulls out. Piggott, Chua and Andison (1985) have shown that there is a maximum permissible free length beyond which the fiber breaks rather than pulls out. The diameter of the matrix surrounding the fiber is given by $2R$.

The literature abounds with studies of fiber/matrix adhesion in polymer composites. Representative studies include those of Chua and Piggot (1985) for shear strengths of glass/polymer interfaces, Penn, Bystry and Marchionni (1983) for kevlar/epoxy composites, and Drzal, Rich and Lloyd (1982) for interfacial adhesion between graphite fibers and epoxy matrices. The literature on the adhesion of embedded smart materials is much more limited. Li, Durkin and Sottos (1994) used fiber pushout tests to characterize the adhesion of PZT rods to polymer matrices. Paine, Jones and Rogers (1992) were the first to address the issue of adhesion in shape memory alloy composites. They performed pullout experiments to measure the bond strength of SMA wires in graphite/epoxy and APC-2 composites.

The work of Paine and Rogers (1993) indicated that the bonding between the SMA fiber and the host material was largely mechanical. They examined the effects of sandblasting, handsanding and acid cleaning on the debond strength of SMAs in composite materials. No coupling agents were used in their study. The focus of the current work was to measure the interfacial strength for SMAs in a pure polymer. Several different surface treatments were used including silane coating, plasma treating, as well as those studied by Paine and Rogers (1993).

2.3 Sample Preparation

Nitinol SMA wires with a composition of 55% nickel and 45% titanium (Mondotronics) were chosen for this study. The 150 μm diameter wires had an austenite start temperature A_s of 55°C, an austenite finish temperature A_f of 70°C, and a martensite finish temperature M_f of 5°C. Five different surface treatments were applied to the wires: Acid etching, handsanding, sandblasting, plasma treating and silane coating. Acid etching was done by first cleaning the wire and then immersing it in a 70% HNO_3 solution for five minutes. Handsanded wires were prepared by sanding the wires for about 12 passes with a 400 grit sandpaper. Handsanding was done such that the resulting grooves on the surface of the wire were lengthwise. Grooves perpendicular to the wire axis could not be made due to the small wire diameter used. Sandblasted sample wires were blasted with fine-grain sand for one minute. Plasma treating of the wires was done by a proprietary process at Adherent Technologies, Albuquerque, New Mexico. For silane coating, three passes were made with a tissue paper dipped in Dow Corning Z-6032. After the surface treatments, all mechanically treated wires were thoroughly rinsed in isopropyl alcohol to remove grease and other impurities. Samples were fabricated by embedding a single nitinol wire in an epoxy matrix (Shell EPON Resin 828 cured with AMICURE PACM). The embedded length l_e was chosen to be 1.27 mm (0.5 in) and the free length L was 4.0 to 5.0 cm. The outer diameter of the sample, $2R$, measured 1.91 cm (0.75 in). Samples were cured for 1 hour at 80°C followed by 1 hour at 150°C. Ten samples of each surface treatment were tested along with ten samples containing untreated wires.

2.4 Effect of Surface Treatments

The pullout tests were performed with an Instron machine using a crosshead speed of 0.1 mm/s. A typical load–displacement curve is plotted in Figure 2.2. Debonding is characterized by a sudden drop in the load carried by the sample. The maximum load is

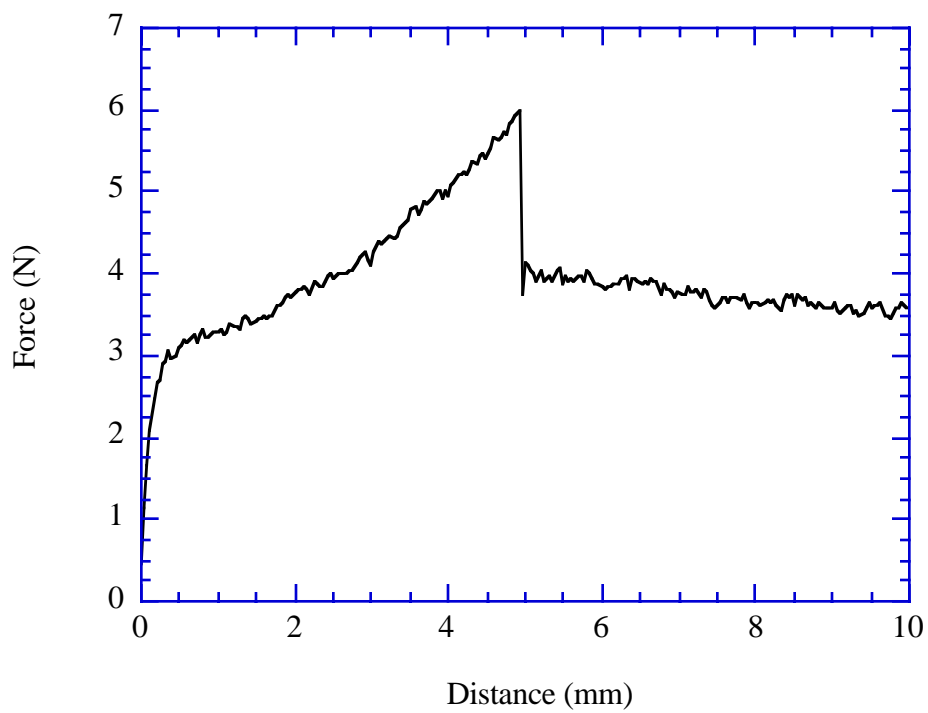


Figure 2.2. A typical experimental pullout curve for an SMA sample.

referred to as the pullout force F_A . Following the work of Penn and Lee (1989), the pullout force can be expressed in terms of the interfacial work of fracture G_i as

$$F_A = 2\pi r^2 \sqrt{\frac{E_f G_i}{r}} \tanh(ns) \quad (2.1)$$

where

$$n^2 = \frac{E_m}{E_f(1 + \nu_m) \ln(R/r)}, \quad s = \frac{l_e}{r} \quad (2.2)$$

in which E_f, ν_f and E_m, ν_m are the elastic moduli and the Poisson ratios of the fiber and the matrix, respectively. Neglecting interfacial friction, the interfacial debond stress τ_d is given by (Piggott, 1991)

$$\tau_d = n \sqrt{\frac{E_f G_i}{r}}. \quad (2.3)$$

The material properties were taken to be $E_f = 49.0$ GPa, $E_m = 2.5$ GPa, $\nu_f = 0.33$ and $\nu_m = 0.30$.

The debond stress was calculated from Equations (2.1)–(2.3) using the average pullout force for each of the surface treatments. The results are shown in Figure 2.3 for comparison and actual values are listed in Table 2.1. Sandblasting increased the bond strength 190% over the untreated wire. The acid etched and handsanded surfaces, however, showed a decrease in interfacial bond strength of 22% and 14%, respectively. These trends are similar to those reported by Paine and Rogers (1992) although the sandblasted wires in the current work displayed a greater quantitative increase in bond strength compared with the untreated wires. The silane coating did not significantly alter the interfacial bond strength while the plasma coating decreased the strength by 6%. Although the embedded SMA wires were activated thermally for experiments discussed in subsequent chapters, the mechanical pullout tests should

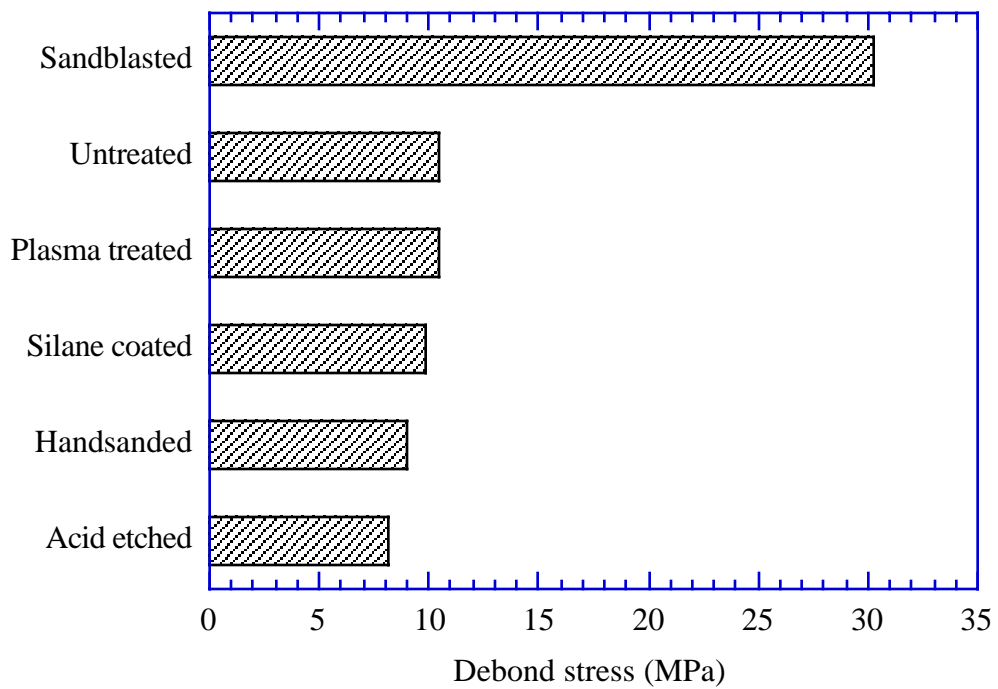


Figure 2.3. Comparison of interfacial debond strengths for different surface treatments.

Table 2.1. Average interfacial debond strength for different surface treatments.

Surface Treatment	Debond Stress (MPa)
Sandblasted	30.3
Untreated	10.5
Silane coated	10.5
Plasma treated	9.8
Handsanded	9.0
Acid etched	8.1

measure of adhesion and ranking of the effectiveness of the surface treatments. For well bonded wires, such as the sandblasted wires, the thermal recovery strains are not high enough to cause debonding. The fact that only the surface roughening of the wires led to an increase in bond strength indicates that the bonding is primarily mechanical in nature.

Further, the age of the curing agent had a measurable effect on the interfacial bond strength. When the pullout tests were repeated with a curing agent that had been on the shelf for about eight months, the interfacial bond strength values nearly doubled. However, the trends persisted. Sandblasted wires still displayed the highest strength while acid etched wires had the lowest. Samples had to be cured with PACM that had not exceeded its shelf life in order to reproduce results reported in Table 2.1.

2.5 Conclusions

The interfacial bond between the SMA wire and the polymer matrix is largely due to mechanical rather than chemical bonding. Increasing the surface roughness of the wire was the only method that effectively raised the bond strength. Sandblasting the wires induced a significant increase in the bond strength while handsanding and acid etching actually decreased it. Silane coatings did not have a significant effect on the bond strength, and the plasma coating reduced the strength slightly.

3. OUT-OF-PLANE DISPLACEMENT

3.1 Introduction

Since SMA materials are used primarily for large-strain applications, the performance of an SMA composite is usually determined by the displacement of the embedded SMA and of the composite matrix. In-situ displacement measurements of the embedded wire are important for evaluating the composite behavior. Li, Durkin and Sottos (1994) have demonstrated that the strength of the interface can be correlated with the local displacements of PZT rods embedded in a polymer matrix. In the current work, the interfacial bond strengths for the SMA/polymer system discussed in Chapter 2 are correlated with in-situ displacement measurements. If the sample geometry and loading fixtures are such that all the boundary conditions can be clearly stated for theoretical analysis, in-situ displacement measurements are ideal for comparison with theoretical models.

Measurement of in-situ SMA displacements is a challenging problem. Because the embedded wires have such a small diameter and any applied load affects the transformation behavior, a non-contact measuring technique is required. Previous investigations by Sottos, Scott and McCullough (1991) have demonstrated the utility of heterodyne microinterferometry for nondestructively measuring displacements in the interfacial region of carbon fiber/polymer matrix composites. More recently, interferometric techniques have been used to measure displacement behavior in piezocomposites (Li, 1995) and magnetostrictive materials (Bellessis et al., 1993). The current investigation adapts heterodyne interferometry to investigate the transient two-way displacements of embedded SMA wires. Local displacements are then correlated with interfacial adhesion.

3.2 Microinterferometric Method

3.2.1 Apparatus

A scanning heterodyne microinterferometer similar to that described by Sottos, Scott and McCullough (1991) is utilized to measure the surface displacements of SMA composite samples. A schematic diagram of the scanning heterodyne microinterferometer is shown in Figure 3.1. A single, linearly polarized light beam of wavelength 514.5 nm from an argon laser (Lexel Laser 3500) is incident upon a 40 MHz acousto-optic modulator (AOM) producing two beams that are sent along different arms of the interferometer. The first beam, which follows path A in Figure 3.1, is shifted in frequency by 40 MHz and is used as a reference beam. The second beam with the same frequency as the beam incident upon the AOM is directed along path B in Figure 3.1 and is used to illuminate the sample surface. The sample serves as a mirror in this arm of the interferometer. The sample is mounted on a translation and rotation stage, such that only the outer edges of the back face of the sample are actually touching the fixture. This arrangement allows the sample to displace freely. The sample is manually adjusted for angular tilt when aligning the interferometer.

The combination of the polarizing beam splitter and the quarter-wave plate allows the sample to be illuminated at normal incidence without excessive light loss. The polarizing cube reflects vertically polarized light, and transmits horizontally polarized light. The vertically polarized light incident upon the cube is reflected through the quarter-wave plate, which circularly polarizes it. After reflection from the sample, the beam passes back through the quarter-wave plate, producing a horizontally polarized beam that passes through the polarizing cube toward the nonpolarizing beam splitter. The half-wave plate in the reference arm rotates the polarization of the modulated beam to match that of the beam from the sample arm. The two beams are recombined at the nonpolarizing beam splitter.

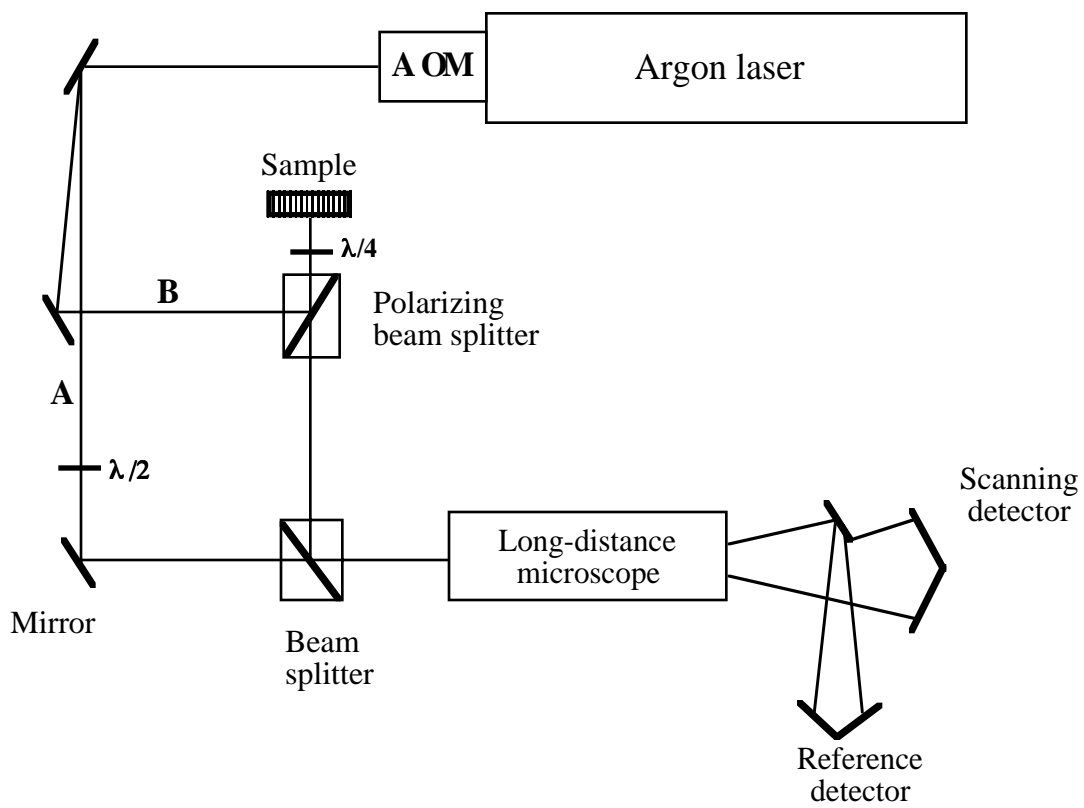


Figure 3.1. Schematic of heterodyne interferometric setup.

The combined beams then arrive at the primary lens of the long-distance microscope (Infinity K2) placed before the eyepiece lens as shown in Figure 3.1. An image (interferogram) of the sample surface is magnified onto the image plane with this long-distance microscope, where a photodiode detector scans the magnified image. The large numerical aperture of the long-distance microscope increases the light gathering power and permits high-resolution imaging. Through the use of different lenses, magnifications from 1x to 100x are attainable. Depending on the magnification of the image, the in-plane resolution is limited either by the optical system or by the diameter of the detector window.

A dynamic image which travels at a 40 MHz beat signal across the image plane is formed because of the difference in frequency between the sample and reference beams. One corner of the image plane is reflected by a mirror onto a second photodetector. The signal at this stationary photodetector is used as a phase reference signal. The phase of the image signal is continuously compared with the phase of the reference signal. As a result, such dynamic disturbances as air turbulence, mechanical vibration, and thermal drift, that occur within the interferometer but away from the sample, do not affect the measurements.

The signal processing unit of the interferometer is shown schematically in Figure 3.2. The scanning photodiode detector is moved across the magnified sample image to the required location using two actuators that are perpendicular to each other. A high-frequency lock-in amplifier (EG&G PARC 5202) is used to measure the phase of the image signal. The output signal from the lock-in amplifier is digitized by a digital oscilloscope (Tektronix TDS 420). Both the oscilloscope and the motion controller are interfaced with a central control unit, a Power Macintosh, via the IEEE-488.2 interface. The sweep rate of the oscilloscope is synchronized to the scanning of the photodetector by a Virtual Instrument (VI) program written in LabView (National Instruments V3.1) graphic language.

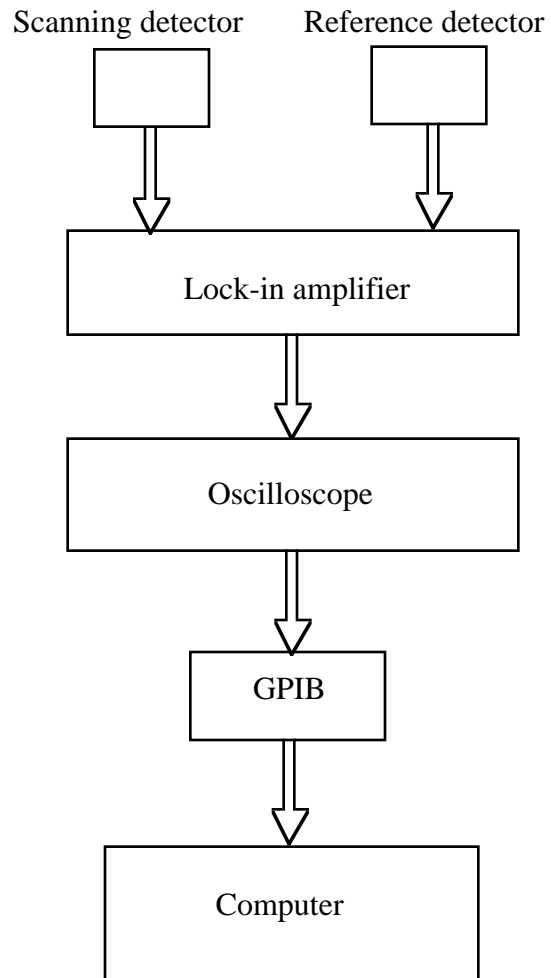


Figure 3.2. Schematic of the signal processing apparatus.

3.2.2 Principle of Operation

The principle of operation of the interferometer was summarized by Li (1995) and is described here briefly. To calculate the change in optical path length produced by out-of-plane motions, one assumes that the incident wave is assumed to be planar, which is a reasonable assumption in the focal zone of a Gaussian beam. With reference to Figure 3.3, the formula that relates the change of optical path length ΔOPL to surface displacement \mathbf{u} can be shown to be as (Monchalin et al., 1989)

$$\Delta\text{OPL} = (\mathbf{k}^i - \mathbf{k}^o) \cdot \mathbf{u} \quad (3.1)$$

Here \mathbf{k}^i is the unit vector in the incident direction while \mathbf{k}^o is that of the observation direction. For detecting out-of-plane displacement w , as in this study, the angle between \mathbf{k}^i and \mathbf{k}^o is 180° . Then, Equation (3.1) is simplified to

$$\Delta\text{OPL} = 2w. \quad (3.2)$$

Let A_o denote the sample beam and A_r be the reference beam. On the image plane (xy plane) A_o and A_r are expressed as

$$A_o = a_o(x, y) \exp\left[i\left[2\pi f_o t + \psi_o(x, y)\right]\right] \quad (3.3)$$

$$A_r = a_r(x, y) \exp\left[i\left[2\pi f_r t + \psi_r(x, y)\right]\right] \quad (3.4)$$

where $a_o(x, y)$ and $a_r(x, y)$ are the amplitudes of A_o and A_r respectively. The symbols f_o , ψ_o and f_r , ψ_r denote the frequency and phase of the sample and reference beam, respectively.

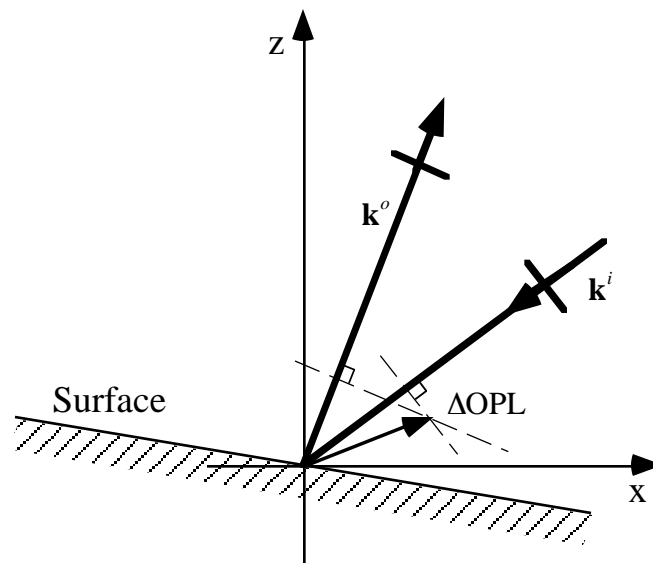


Fig. 3.3. Schematic of the displacement and optical path relation.

The intensity of the superposed sample wave and reference wave, which is detected by the photodetector, is given as

$$I = a_o^2 + a_r^2 + 2a_o a_r \cos[2\pi(f_r - f_o)t + (\psi_r - \psi_o)]. \quad (3.5)$$

Here the frequency difference $f_r - f_o$ is set by the AOM at 40 MHz. The phase of the scanning detector output current, $\psi = \psi_r - \psi_o$, is measured with reference to the stationary detector. Any out-of-plane displacement of the sample surface produces a phase shift in the 40 MHz beat signal at the corresponding image plane. The relation between this phase shift $\Delta\psi$ and the change of optical path length ΔOPL due to out-of-plane displacement w is

$$\Delta\psi = \frac{2\pi}{\lambda} \Delta\text{OPL} \quad (3.6)$$

where λ is the wavelength of the laser light (Li, 1995). The displacement w can then be calculated from this phase shift using Equation (3.2). Obtaining a $\lambda/100 \approx 5$ nm sensitivity would require a phase measurement accuracy of approximately 7° , which is within the specifications of the lock-in amplifier used.

3.3 Transient Displacement Measurements—150 μm Wires

3.3.1 Sample Preparation

Samples for the displacement measurements consisted of a single, surface treated 150 μm SMA wire embedded in an epoxy matrix as shown in Figure 3.4. The material properties of the wire are listed in Table 3.1. Prior to embedding in the matrix, the SMA wires were trained to exhibit the two-way shape memory effect. Among the different training procedures described in the literature (Perkins and Hodgson, 1989), the method of constrained temperature cycling was used to train the wires. The two-way training procedure has four basic steps. First, the wires are placed in a training fixture and cooled

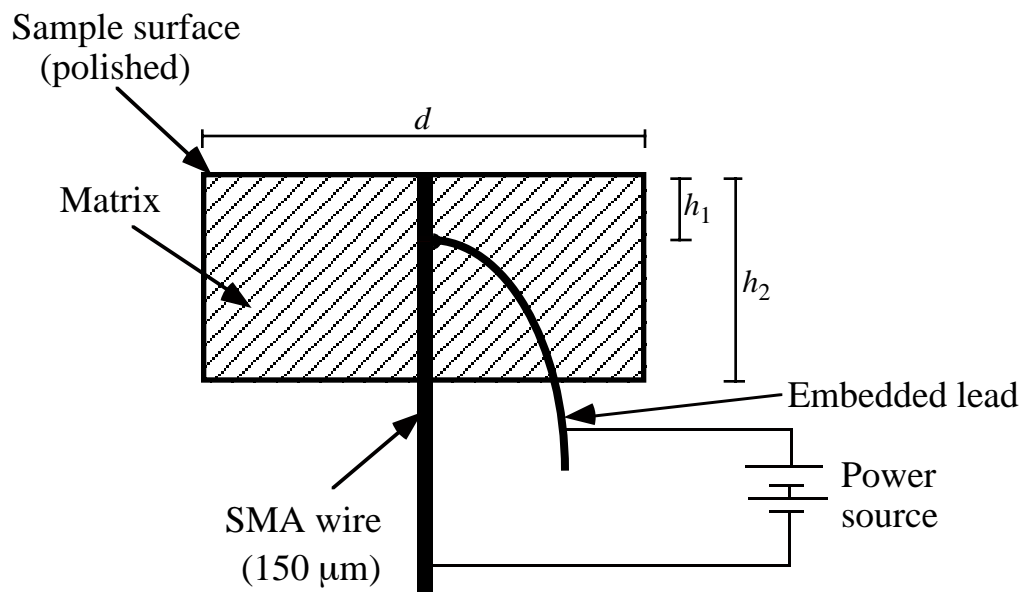


Figure 3.4. Schematic of 150 μm sample with dimensions

$$d = 32 \text{ mm}, h_1 = 2 \text{ mm and } h_2 = 15 \text{ mm}$$

Table 3.1. Material properties for epoxy matrix and SMA wire.

Material Property	Epoxy Matrix	SMA Wire
E (GPa)	2.5	49.0*
ν	0.33	0.3*
α ($\times 10^{-6}/^{\circ}\text{C}$)	68.0	10.9*
K (W/m $^{\circ}\text{C}$)	0.18	18.0*
A_f ($^{\circ}\text{C}$)	-----	70
A_s ($^{\circ}\text{C}$)	-----	55
M_s ($^{\circ}\text{C}$)	-----	35
M_f ($^{\circ}\text{C}$)	-----	5

* Austenite values are listed.

to below the martensite finish temperature M_f with liquid nitrogen. An initial strain of 5% is then introduced to produce stress-induced martensite. The wires are held at this strain and resistively heated to above the austenite finish temperature. This temperature cycle is repeated from above A_f to below M_f about thirty times. The training results in about 1.5 to 2% memory strain, which can be cycled by heating and cooling. To reduce the variability in memory strain, all the samples for the interferometric measurements were made from a single long wire that was cut into four different parts after training. One part was left untreated while the other three were subjected to handsanding, acid etching or sandblasting. Displacement measurements were not made for silane coated and plasma treated wires since the pullout tests in Chapter 2 did not indicate a significant difference in bond strengths compared with those of the untreated wires.

The wires were embedded in an EPON Resin 828 epoxy matrix cured with PACM as described previously for the pullout samples. The samples were polished and a thin layer of gold (approximately 1000 Å) evaporated on to the surface to provide a flat, reflective surface for use in the interferometer. The two-way shape memory effect was induced by heating the embedded wires. The wires were heated electrically to provide a repeatable, easily controlled heating method with minimal convection into the interferometer path. A relatively large current of 0.4 A was required to heat the wires above A_f .

Ideally, the layer of evaporated gold could serve as a conduction path for the current to heat the wire. However, the gold was too thin (even with multiple evaporations) to withstand the high current requirement for the wires in the current study. To remedy this difficulty, a lead was carefully attached to the wire below the sample surface as shown in Figure 3.4. Prior to embedding, the lead was looped around the SMA wire and a small amount of conductive paint applied to ensure good contact. A drop of glue was added at the point of contact to prevent damage during cure. After embedding and polishing, the

lead was located approximately 2 mm from the top surface and the total embedded length of the wire was 15 mm. The portion of the wire from the embedded lead to the free end was resistively heated while the remaining section (about 15% of the total length) of the wire from the lead to the measurement surface was heated more slowly by conduction.

An endeavor was made to measure the temperature change along the SMA wire as it was heated. Type K thermocouples approximately 25 μm in diameter (75 μm junction) were carefully embedded near the surface of the wire in one of the samples. These were the smallest thermocouples available that could be embedded reliably without breaking. Because the thermocouples could not be placed directly on the resistively heated portion of the wire, they were positioned with a multi-axis stage as close to the wire as possible prior to embedding—approximately 10 μm from the wire surface. In Figure 3.5, the temperature profiles are plotted from two different thermocouple locations along the wire. The first thermocouple was located midway along the portion of the wire heated resistively. The temperature of this section rose uniformly to 53°C in 400 seconds. The same temperature profile was obtained at several points along the length of this section, indicating a constant temperature rise. The second thermocouple was located adjacent to the portion of the wire heated by conduction at a point 2 mm away from the resistively heated end (just below the surface of the sample). As expected, this portion of the wire heated much more slowly, reaching a temperature of only 30°C in 400 seconds. Because of the relative size of the thermocouple junction to the SMA wire and the location just next to the wire, the temperatures recorded are probably lower than the actual temperatures in the wire. However, the profiles do give an indication of how the wire was heated.

3.3.2 *Displacement Measurements*

Transient wire displacements were recorded continuously during heating and cooling of the wire. A typical transient displacement curve for an untreated wire is shown

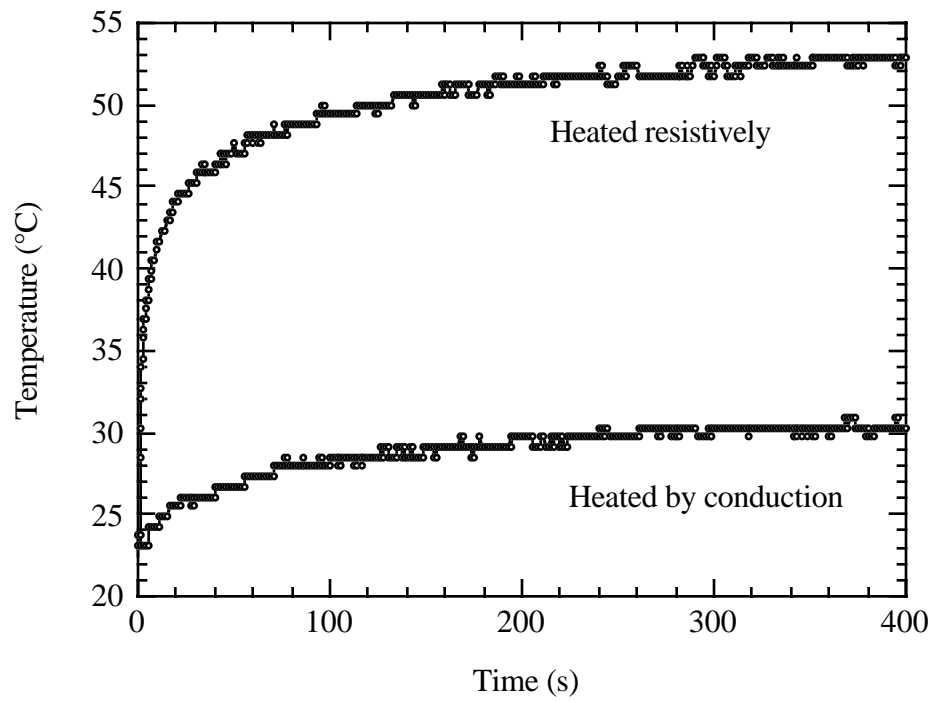


Figure 3.5. Temperature profile adjacent to SMA wire during heating.

in Figure 3.6. The current is switched on at point A and off at point C. As the wire heats up to the austenite start temperature A_s of about 55°C, an initial thermal expansion occurs from point A to point B. Martensite-to-austenite transformation results in contraction of the wire, leading to an inward movement from point B to C. The B–C portion of the curve is the “actuation” of the wire. The wire displaces slowly due to the fact that the point of observation (top surface of the wire) is not heated resistively but rather by heat conducted from the portion of the wire below the lead. When the current is switched off at point C, the wire continues to move inward due to thermal contraction resulting from a decrease in temperature. As the martensite start temperature M_s is reached at D, reverse transformation begins and the wire moves outward.

Comparison of the slopes of B–C and D–E shows that the reverse transformation from austenite to martensite takes longer than transformation from martensite to austenite. Cooling of the wire occurs more slowly by conduction alone. Additionally, the austenite-to-martensite transformation occurs over a wider temperature range. The slower rate of reverse transformation is clearly evident in Figure 3.7 where the normalized (thermal expansion and contraction deleted) heating and cooling curves are plotted. Figure 3.7 also shows that not all the transformation strain is recovered during cooling since M_f is below room temperature.

Displacements were measured for at least two samples for each surface treatment. More than five actuation cycles were necessary before repeatable displacement profiles were achieved for a given sample. Figure 3.8 shows the repeatability of the normalized displacements. The continued repeatability of the displacement profiles with repetitive actuation indicated no loss of recovery strain with continued cycling. White et al. (1995) have investigated the effects of long term thermal cycling on the transformational

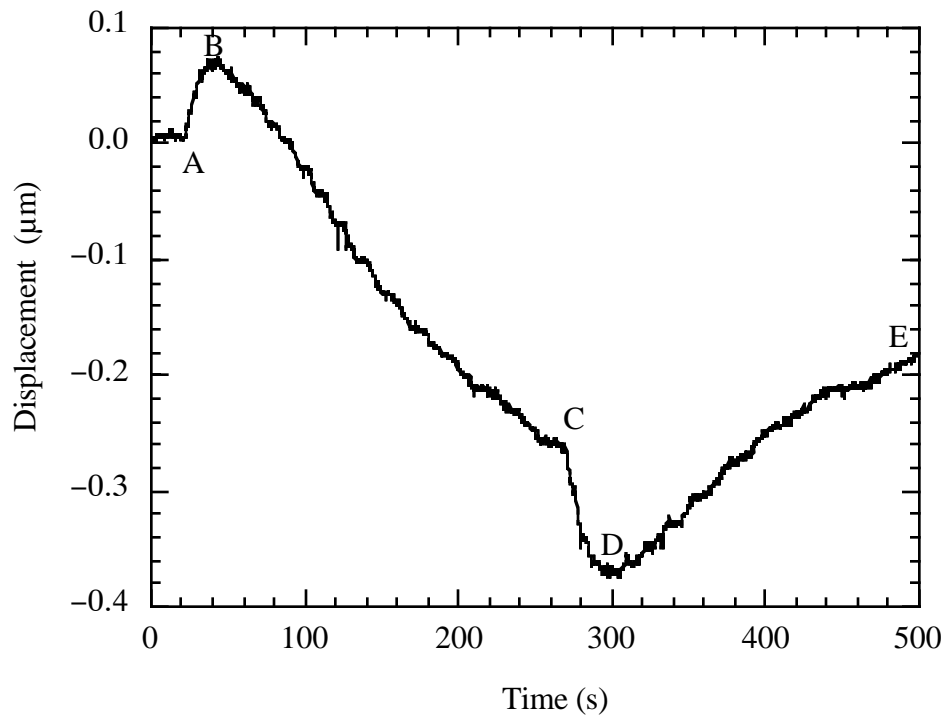


Figure 3.6. Typical transient displacement curve for embedded 150 µm SMA wire in epoxy.

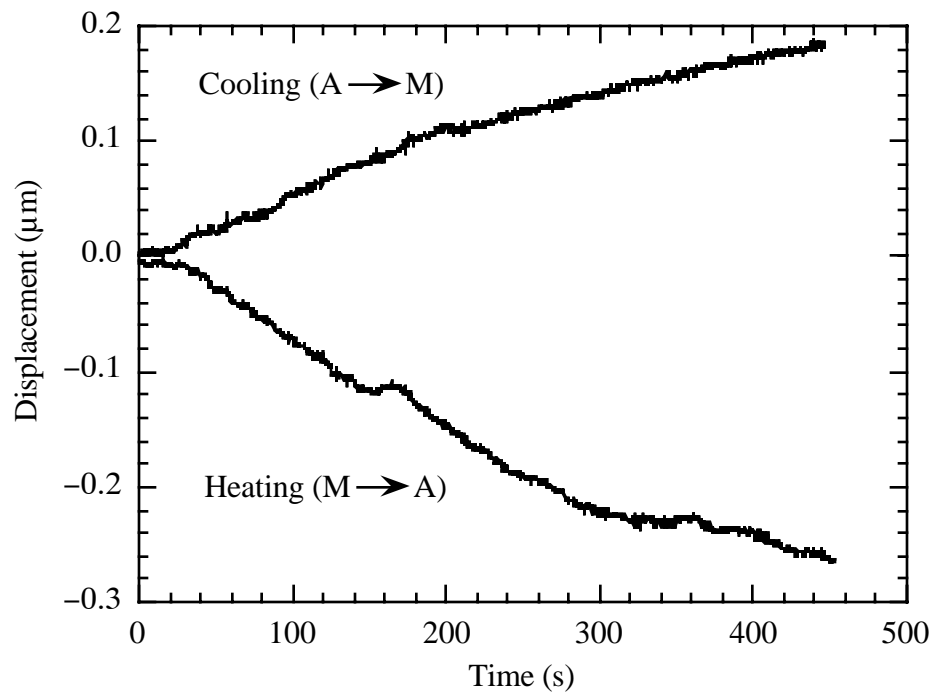


Figure 3.7. Transient displacement behavior of 150 μm embedded SMA wire upon heating and cooling.

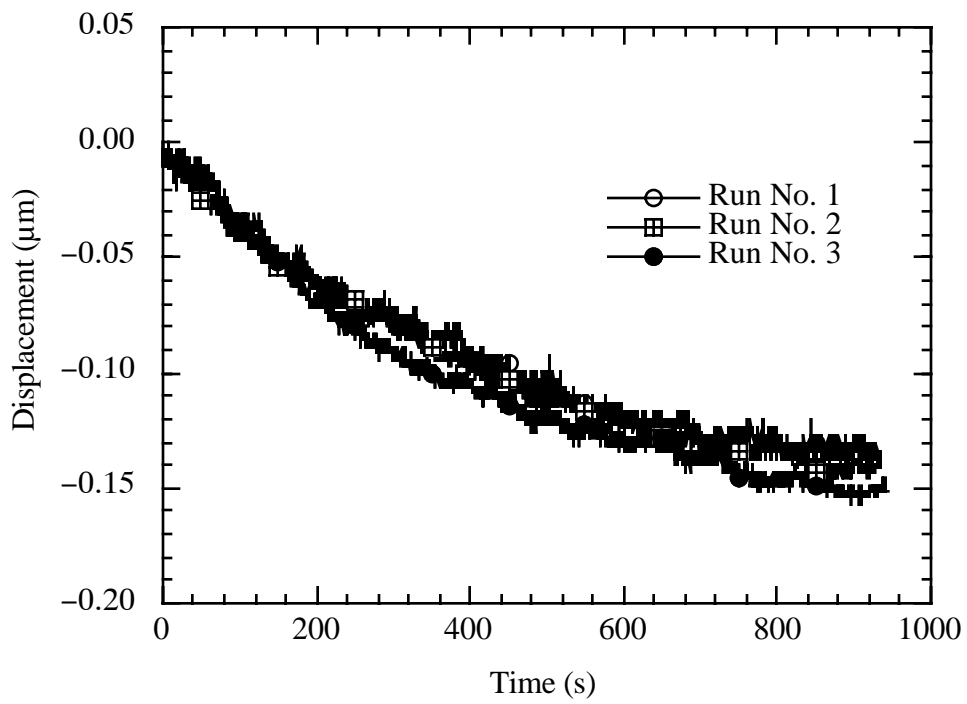


Figure 3.8. Repeatability of normalized displacements of embedded, untreated, 150 μm wires in epoxy.

behavior of two-way trained SMA wires. They reported no degradation in recovery strain over 10,000 thermal cycles.

Several consecutive displacement measurements were made on a sample. The average value of the maximum normalized displacement due to the martensite-to-austenite transformation (B–C) is plotted in Figure 3.9 and listed in Table 3.2 for each surface treatment. The acid etched wires show the maximum displacement, followed by handsanded, untreated and sandblasted wires, in that order. Comparison of maximum displacement with pullout data in Table 2.1 indicates that displacement values increase with decreasing interfacial adhesion. Displacements measured for acid etched wires were approximately three times larger than the displacements observed for sandblasted wires. Because all of the embedded wires had identical recovery strain, each wire exerts nearly the same recovery stress on the interface upon actuation. A strong interfacial bond resulted in greater resistance by the matrix to the movement of the actuating wire. Consequently, the sandblasted wire, which had the highest interfacial bond strength, had the lowest displacement. Similarly, the acid etched wire had the highest displacement.

3.4 Transient Displacement Measurements—50 μm Wires

In Section 3.3, it was necessary to embed a lead wire below the surface of the sample in order to supply the current required to transform the 150 μm SMA wire. While interesting results were obtained from the interferometric measurements, the presence of the lead precludes the use of displacement data for simple comparison with theoretical models. Photoelastic images of sectioned 150 μm samples with and without a lead are shown in Figure 3.10 and Figure 3.11 respectively. There is a negligible stress field near the wire without the lead prior to actuation. The photoelastic fringe pattern around the lead in Figure 3.11, however, indicates that the lead acts as a stress concentration point and would

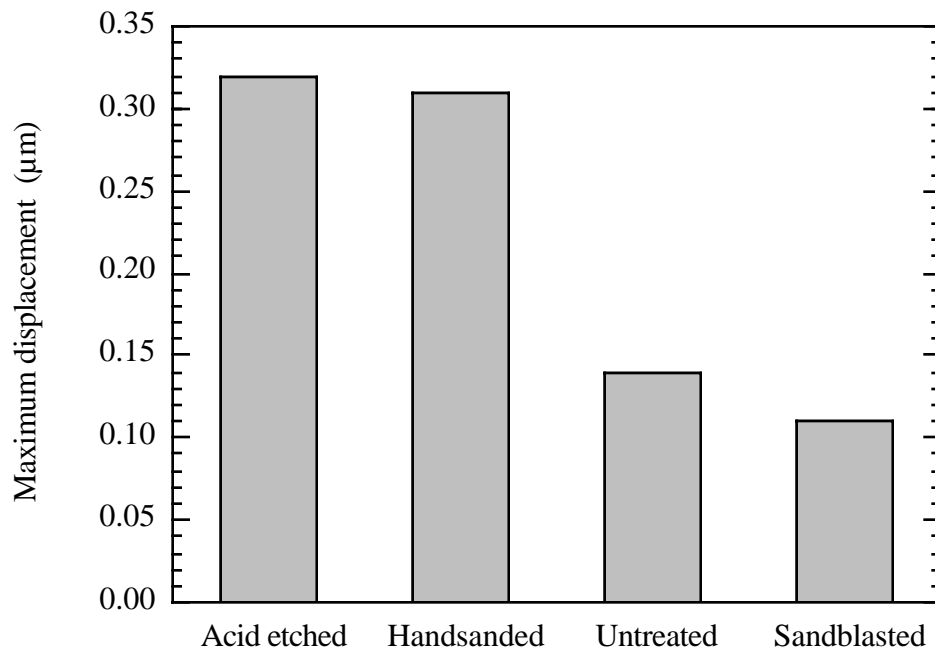


Figure 3.9. Maximum displacement of SMA wire for different surface treatments.

Table 3.2. Maximum displacements of embedded wires with various surface treatments.

Surface treatment	Maximum displacement (μm)
Sandblasted	0.11
Untreated	0.14
Handsanded	0.31
Acid etched	0.32

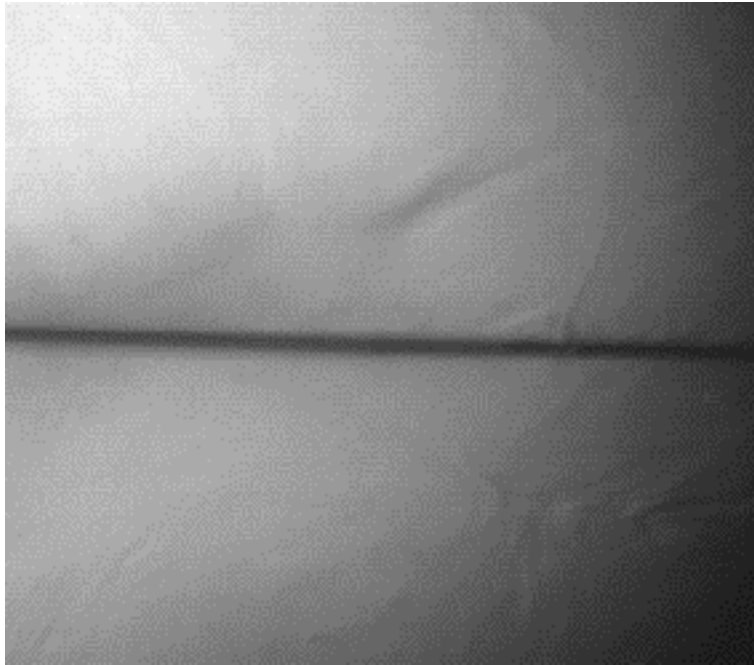


Fig. 3.10. Photoelastic image of sectioned 150 μm wire sample without embedded lead wire, showing a negligible stress field.

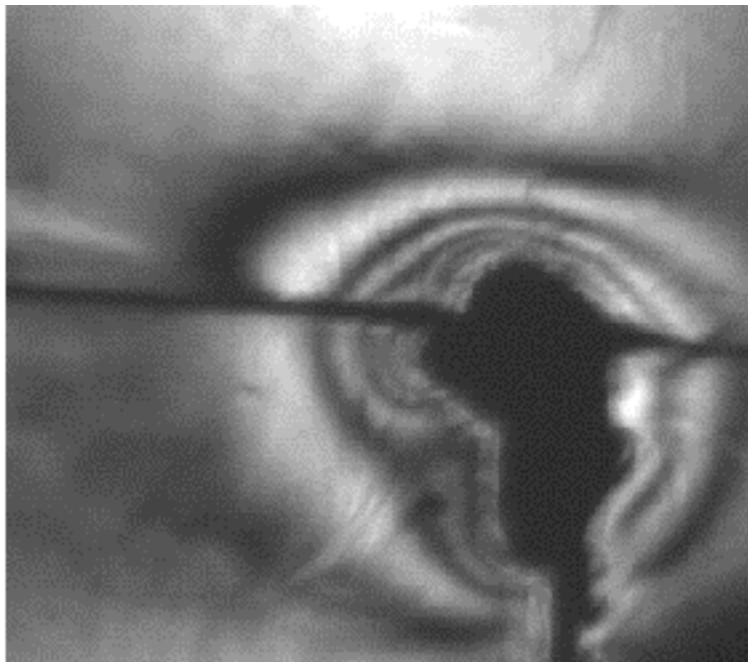


Figure 3.11. Photoelastic image of sectioned 150 μm wire sample with embedded lead wire, showing stress concentration around the lead.

influence the displacement of the wire. The effect of the lead on the displacements cannot be readily quantified.

An alternative approach is to use smaller diameter wires so that the power requirements for actuation are reduced. The gold layer on the surface of the sample could then be used as a conduction path to heat the sample resistively. SMA wires with a diameter of 50 μm were obtained from Mondotronics. The current requirement was reduced to about 0.1 A for the new 50 μm wires with the same transformation temperatures as for the 150 μm wires.

Preliminary experiments indicated that the 0.1 A current requirement was still too large for conduction through the gold surface. To circumvent this problem, a portion of the wire was coated with conductive silver/epoxy and cured at room temperature for 24 hours prior to embedding in the epoxy matrix. The sample was then cut and polished. The final sample configuration had silver/epoxy surrounding the wire from the surface to a depth of about 2 mm as shown in Figure 3.12. The sample diameter d and the embedded length h_2 remained at 32 mm and 15 mm, respectively. A thin line of conductive silver imprinting paint was drawn on the surface of the sample, leading from the silver/epoxy around the wire to the lead connected to the power source. On drying, the silver paint served as the path for conduction of current to the silver/epoxy and the SMA wire. After the paint was dry, a thin layer of gold was evaporated on to the surface of the sample. The gold was again used only to provide a reflective surface for interferometry and not as a conductive path. While the sample may not be heated uniformly due to the presence of the silver/epoxy, the lead wire was no longer required.

Results from Chapter 2 indicated that sandblasting was the only way to increase adhesion, with the other treatments having little effect. Due to small wire diameters, it was

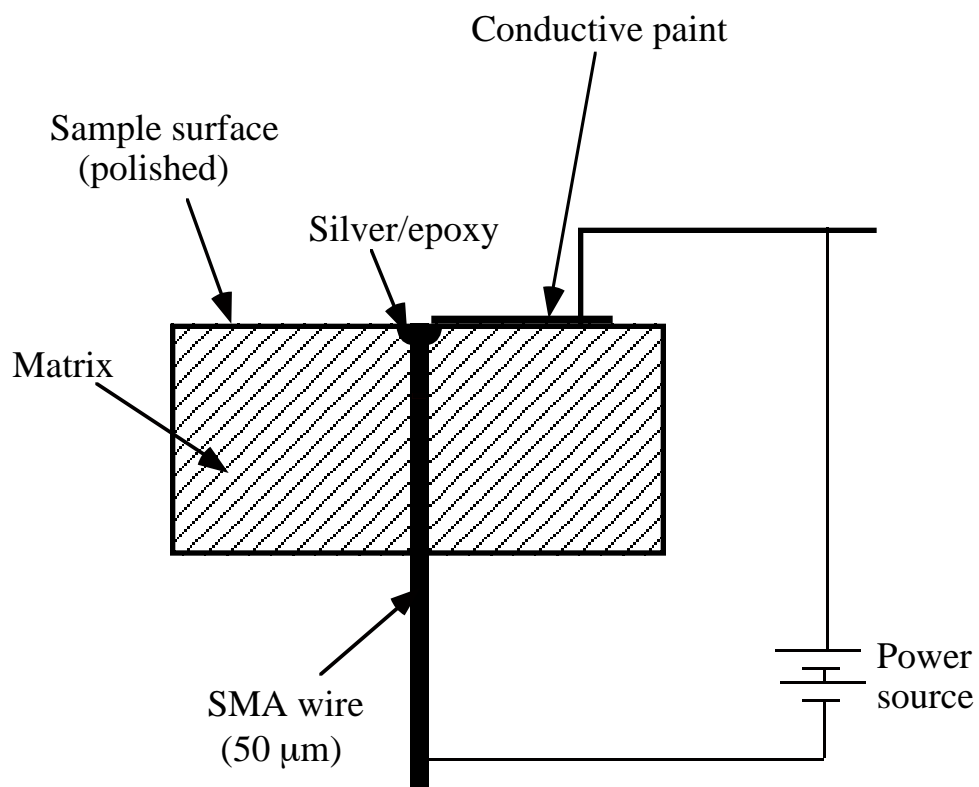


Figure 3.12. Schematic of 50 μm sample.

impossible to sandblast or handsand the 50 μm wires without causing severe plastic deformations. Therefore, all the experiments with 50 μm wires were performed with untreated wires.

Initially, annealed SMA wires were embedded in the polymer matrix in order to obtain a transient thermal displacement profile with no SMA actuation. The results are shown in Figure 3.13. Theoretical predictions of the wire displacement were obtained from the model by Sottos and McCullough (1992) using the material properties listed in Table 3.1. A steady state out-of-plane displacement of 0.269 μm was predicted for the wire. The measured thermal displacements are in good agreement with this theoretical prediction.

When similar experiments were attempted for trained SMA wires in epoxy matrix, the results were unrepeatable and inconclusive. Figure 3.14 shows the displacement profiles for three different samples with trained and embedded 50 μm SMA wires. There was a significant variability in the displacement profiles. Most samples behaved as if there was no induced training and only thermal displacement profiles were observed (curve A). A few samples showed minor actuation (curve B). Only one sample in about 50 showed significant actuation following the thermal displacement (curve C). The lack of repeatable actuation was attributed to the small diameter of the wires with small recovery forces that could not induce significant actuation. Sectioning of the only sample that actuated indicated an unusually large number of air bubbles. However, samples that were made subsequently with high air bubble content (obtained by not degassing the epoxy/curing agent mixture before curing) did not show any actuation. It is also possible that there was some local debonding near the top of the wire for the sample corresponding to curve C, although this conjecture could not be verified.

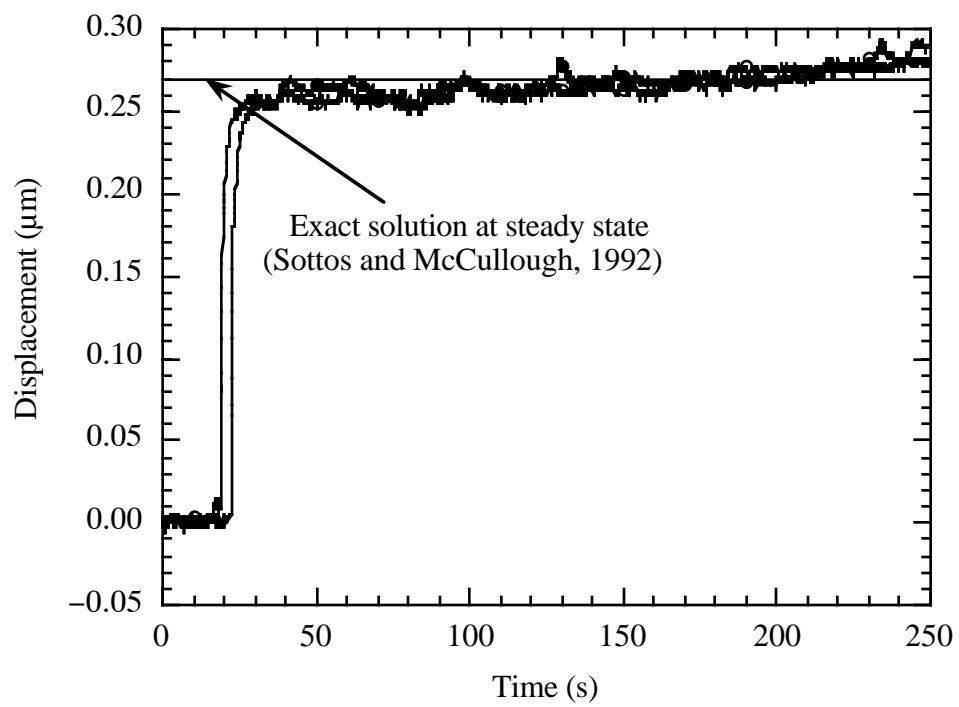


Figure 3.13. Transient displacement profiles of annealed and embedded $50\ \mu\text{m}$ SMA wires.

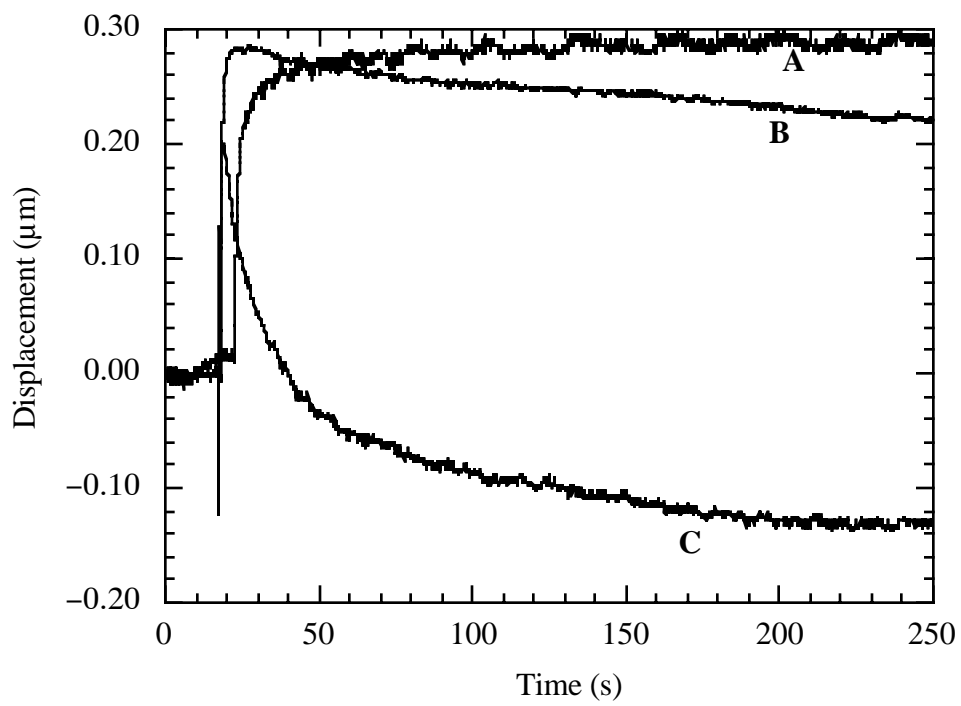


Figure 3.14. Transient displacement profiles of two-way trained and embedded 50 μm SMA wires.

3.5 Conclusions

Heterodyne interferometry was successfully employed to provide a qualitative understanding of the transient behavior of SMA composites. Experiments with 150 μm SMA wires in polymers indicated that thermal expansion happens much faster than SMA actuation for the geometry and loading conditions considered. The interfacial bond strengths from pullout tests were correlated with maximum wire displacements. The sandblasted wires, which exhibited the highest interfacial bond strength (30.3 MPa), recorded the smallest displacements (0.11 μm). The acid etched wires, which had the lowest bond strength (4.1 MPa), had the largest displacement (0.32 μm). The restraining effect of the matrix increased with increasing bond strength, causing a decrease in the wire displacement. Experiments with 50 μm SMA wires showed that larger diameter wires may be necessary for inducing significant strain in the matrix.

4. LOAD TRANSFER

4.1 Introduction

Understanding the interaction between the embedded SMA materials and the host material is critical for designing a reliable smart structure. Measurement of the stresses induced in the host material is particularly important for assessing the effects of the host on SMA performance. A recent study by Kline (1995) utilized photoelasticity to investigate the maximum shear stress induced in a polymer matrix due to SMA wire actuation. The maximum shear stress was correlated with the interfacial bond strength of the SMA/polymer interface. As the level of interfacial adhesion increased, the stresses in the matrix also increased. The sample geometry used by Kline (1995) provided qualitative data for correlating load transfer with interfacial bond strength but was not suitable for calculation of induced shear stresses. In the current study, the photoelastic technique is used to quantify the time dependent stresses in the matrix induced by the actuation of SMA ribbons.

4.2 Experimental Setup

A polariscope was constructed as shown schematically in Figure 4.1 using a 1W argon laser (Lexel 3500) as the light source. Since coherent light can create interference fringes, a spinning ground-glass disk was used as a coherency scrambler. A collimated beam of light was passed through a polarizer, which vertically polarized the light, and then through a quarter-wave plate with its fast axis at 45° to the axis of the polarizer, producing circularly polarized light. After passing through the specimen, the light beam traversed a second quarter plate 90° out of phase with the first and then through a second polarizer, thus eliminating isoclinic fringes from the resulting image. Two lenses were used to expand the diameter of the beam, permitting a larger field of view. The focus of the first lens, with a focal length of 2 cm, was placed at the focus of the second lens,

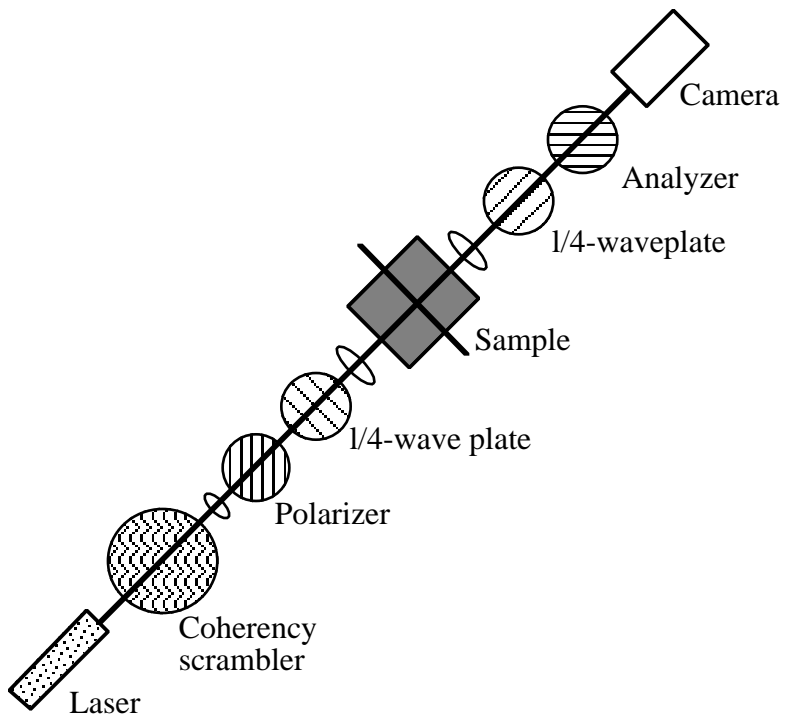


Figure 4.1. Schematic of circular polariscope.

which had a focal length of 20 cm, increasing the diameter of the beam from 2.5 mm to 25 mm. A VCR (Mitsubishi U82) was connected to a CCD camera (Panasonic BL200) to record the development of fringes. A 640 pixel by 480 pixel frame grabber was used to store the recorded eight-bit gray scale images at discrete time increments of 15 seconds.

4.3 Load Transfer—High Temperature Cure Matrix

Chapter 3 discussed the out-of-plane displacements of SMA wires in PACM/epoxy. The present section examines the load transfer behavior of SMAs in the same polymer matrix. The main objective is to obtain quantitative data for comparison with theoretical models for embedded SMAs. Since the PACM/epoxy system displays temporary double refraction under applied load, it is readily adaptable for photoelastic applications. In order to fabricate samples that satisfy the plane stress approximation of two-dimensional photoelasticity, SMA ribbons rather than wires were embedded in the host material.

4.3.1 Sample Preparation

A single SMA ribbon (55% Ni, 45% Ti, Shape Memory Alloys, Inc.), 1.27 mm wide and 0.3 mm thick, was embedded in an epoxy matrix. A schematic of the sample is shown in Figure 4.2. The transformation temperatures of the ribbons were measured using a differential scanning calorimeter (DSC) and are listed in Table 4.1. All the ribbons were sandblasted prior to embedding in order to maximize the interfacial adhesion. Since the host material was cured at elevated temperature, it was necessary to two-way train the ribbons before embedding them. The training procedure is identical to the training of SMA wires described in Chapter 3 except for modified end grips in the training fixture required to hold the ribbons. Also, a larger power source was necessary to heat the ribbons, which have a greater cross-sectional area than the wires in Chapter 3. Upon training a number of ribbons with this procedure, the recovery strains were usually less than 1% .

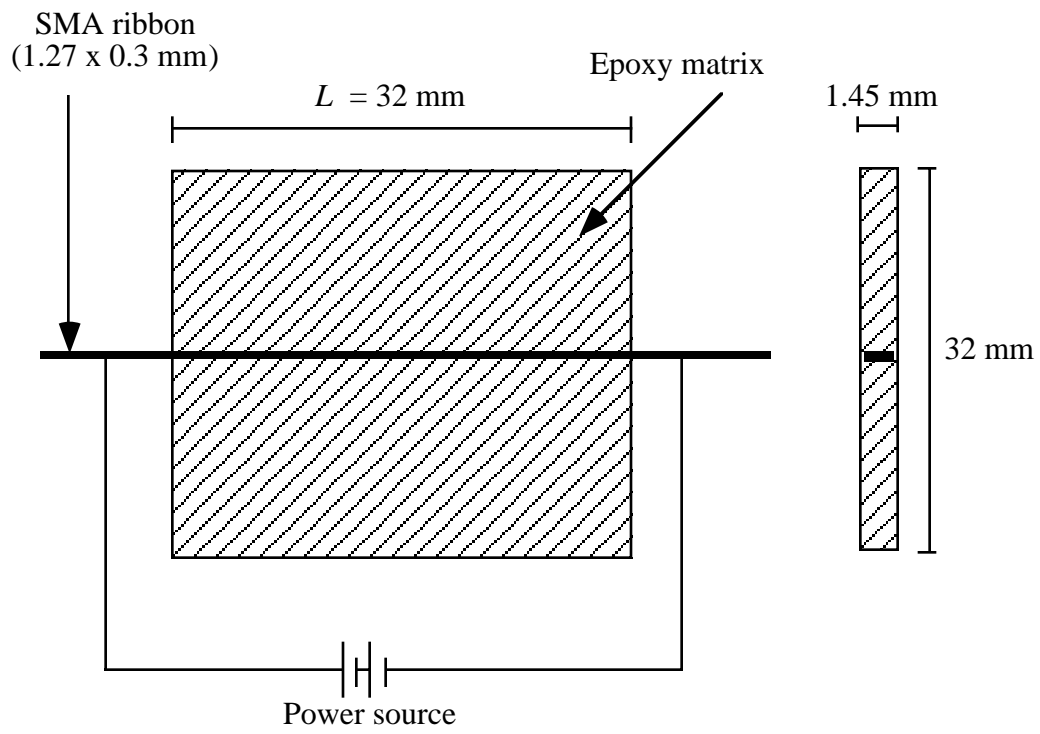


Figure 4.2. Schematic of photoelastic sample.

Table 4.1. Material properties of SMA ribbon in austenitic and martensitic phases.

Material property	Austenite	Martensite
E (GPa)	49.0	10.9
ν	0.3	0.3
α (x 10 ⁻⁶ /°C)	22.5	22.5
K (W/m°C)	18.0	8.5
ρ (Kg/m ³)	6450	6450
C_A (MPa/°C)	----	13.5
C_M (MPa/°C)	13.5	----
A_f (°C)	----	57.0
A_s (°C)	----	35.0
M_s (°C)	21.0	----
M_f (°C)	-12.0	----

The ribbons were embedded in EPON 828 matrix cured with PACM as described previously for the out-of-plane displacement samples. As a consequence of the meniscus that formed around the edge of the samples, it was impossible to pour the sample thinner than about 5 mm. Polishing of the samples was necessary to diminish their thickness and to provide a flat surface for use in the polariscope. Prepared samples were approximately 1.45 mm in thickness. An additional set of control samples was prepared in a fashion similar to that described above. In this case, however, the ribbons were annealed at 600°C for ten minutes to remove any shape memory effect. Further, aluminum strips with cross-sections identical to the SMA ribbons were fabricated and embedded in an epoxy matrix. Samples were also made with SMA ribbons as received from the manufacturer. These ribbons have large internal stresses due to plastic flow during processing. The processed ribbons have no shape memory effect at all and cannot be two-way trained without first removing the internal stresses by annealing. The untrained SMA ribbons and the embedded aluminum samples provide a basis for comparison of load transfer due to thermal and SMA effects.

4.3.2 *Sample Actuation and Discussion*

The coefficients of thermal expansion for the SMA ribbons and polymer matrix as listed in Tables 4.1 and 4.2 are 22.5 $\mu\text{m}/\text{m}^\circ\text{C}$ and 68.0 $\mu\text{m}/\text{m}^\circ\text{C}$, respectively. The value of the coefficient of thermal expansion (CTE) for aluminum is 23.6 $\mu\text{m}/\text{m}^\circ\text{C}$ (ASM Metals Handbook, 1990). Due to differences in CTEs, residual stresses develop when the cured sample is cooled from a stress free state at 150°C to room temperature. As the sample cools to room temperature, the SMA ribbon contracts. The matrix, which has a higher value of CTE, undergoes greater contraction. After cooling to room temperature, the ribbon is in compression and the matrix in tension, both for SMA and aluminum samples. The displacements at the cure and room temperatures are schematically illustrated in Figure 4.3.

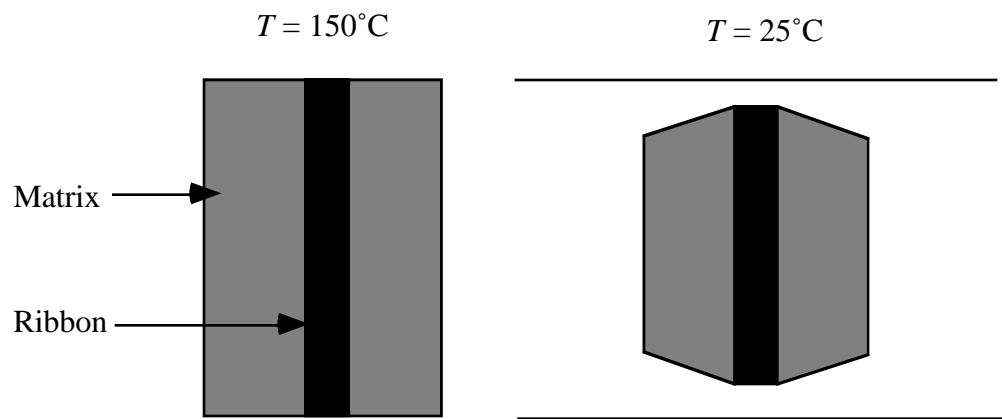
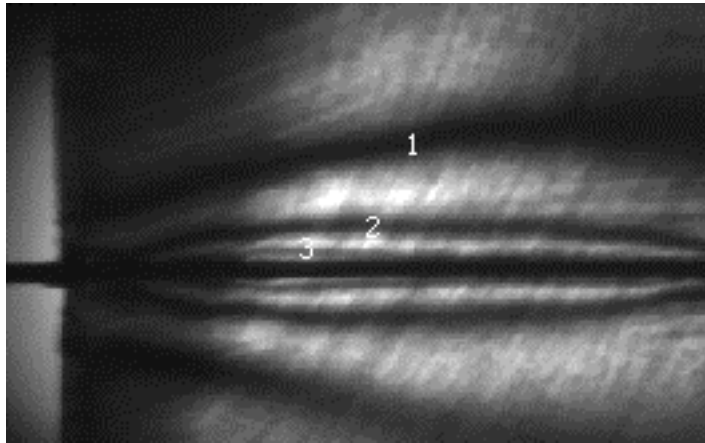


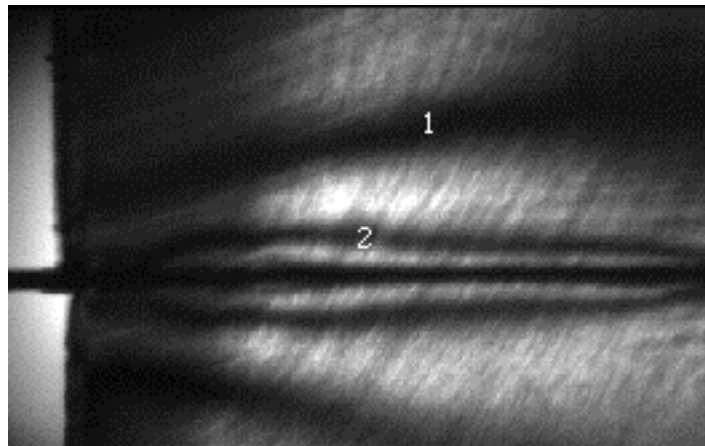
Figure 4.3. Schematic description of thermal contraction on cooling from a cure temperature of 150°C to a room temperature of 25°C .

Resistively heated embedded aluminum ribbon samples were used to examine the behavior of a material with a coefficient of thermal expansion similar to that of the SMA but without any shape memory effect. Figure 4.4 (a) shows a photoelastic image of a symmetric half sample with an embedded aluminum ribbon at room temperature. The fringes are numbered, with the outermost fringe being the first. Three distinct fringes, indicating residual stresses, are observed in the matrix. A current of 7 A was used to heat the aluminum ribbon. Due to the high electrical conductivity of aluminum and the relatively large cross-sectional area of the ribbon, it was not possible to raise the temperature of the ribbon by more than 20°C with the wiring used in the experimental setup. Figure 4.4 (b) shows a photoelastic image of the resistively heated aluminum ribbon at a steady state temperature of 45°C. The number of fringes decreases from three to two following an inward movement of the fringes from the top and bottom edges of the sample towards the SMA ribbon. Reduction in the number of fringes indicates stress relief in the matrix. When the ribbon is heated resistively, aluminum expands. However, the surrounding matrix, which has a higher CTE, is heated by conduction and undergoes greater expansion than aluminum, relieving some of the residual stresses induced during cooldown from cure temperature.

The next set of experiments was performed with processed SMA ribbons (as received from the manufacturer). Photoelastic images of the sample before and after heating are shown in Figures 4.5 (a) and 4.5 (b), respectively. The ribbons were heated to a steady state temperature of 80°C by a current of 2.25 A. A CTE value of 11.5 $\mu\text{m}/\text{m}^\circ\text{C}$ was calculated for the processed SMA by obtaining the CTEs of nickel and titanium separately (ASM Metals Handbook, 1990) and taking a weighted average based on the composition of the nitinol alloy (55% nickel, 45% titanium). Since the difference in the CTEs of the polymer and the processed SMA is higher than the difference between the CTEs of the polymer and aluminum, greater residual stresses are observed at room

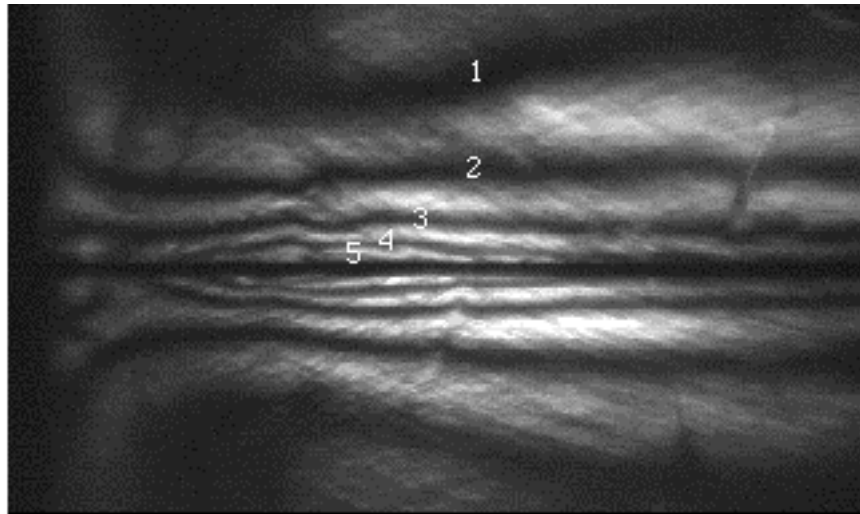


(a)

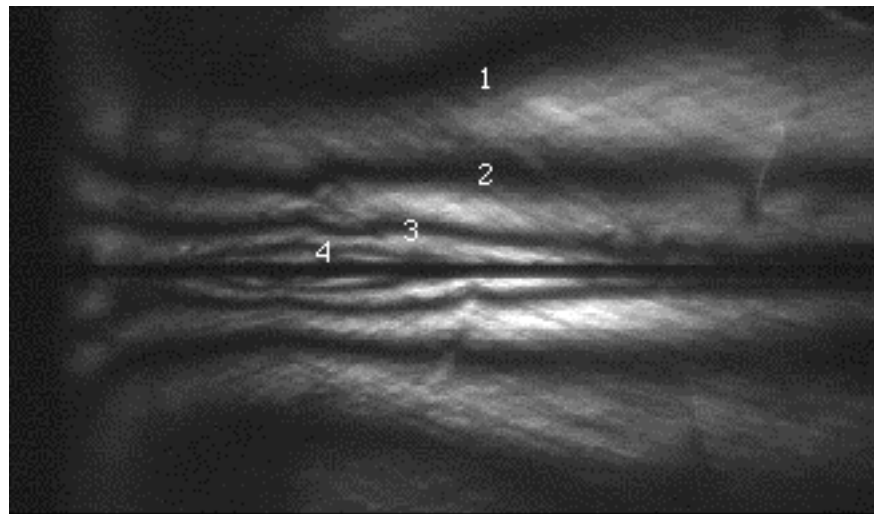


(b)

Figure 4.4. Photoelastic images of aluminum ribbon sample at different temperatures: (a) $T = 25^{\circ}\text{C}$ and (b) $T = 45^{\circ}\text{C}$.



(a)



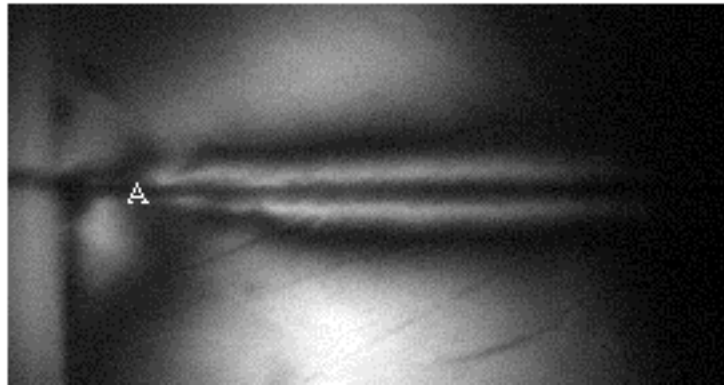
(b)

Figure 4.5. Photoelastic images of processed SMA sample at different temperatures: (a) $T = 25^{\circ}\text{C}$ and (b) $T = 80^{\circ}\text{C}$.

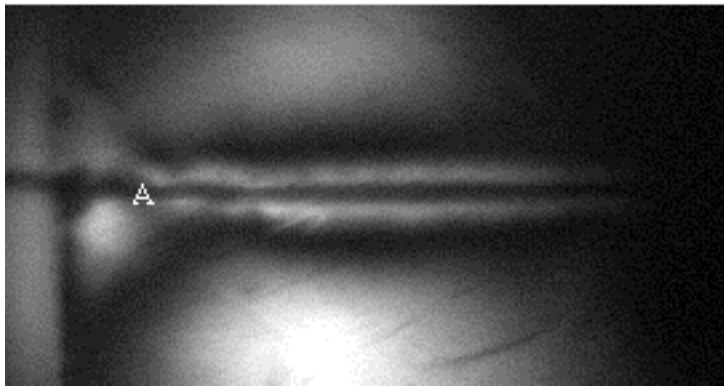
temperature in processed SMA samples. Upon heating, stress is again relieved, as indicated by a decrease in the number of fringes from five to four. The fringes again move inward towards the ribbon from the top and bottom edges of the sample.

The sample responses with annealed ribbons and two-way trained ribbons were quite different. Photoelastic images of an annealed ribbon at different temperatures are shown in Figure 4.6. The samples were heated to a maximum temperature of 80°C, which is well above the austenite finish temperature of 57°C. An immediate observation from Figure 4.6 (a) is that there is a marked reduction in residual stresses at room temperature compared with those in the processed SMA sample. Also, since the CTE values of aluminum and the annealed SMA ribbon are numerically close, a residual stress field similar to that of the aluminum sample would be expected. The lower residual stress field in the annealed and two-way trained samples results from reorientation of the martensite phase to accommodate some of the residual stresses, thus providing stress relief. There is a slight outward movement of fringes from the ribbon to the top and bottom edges of the sample with increasing temperature. This effect is clearly seen at point A in Figure 4.6. The outward movement is in contrast to the aluminum and processed SMA samples where the fringes moved inward upon heating.

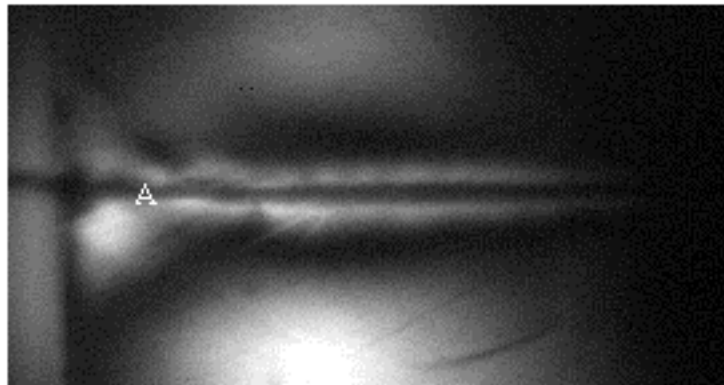
The residual stresses in the composite at room temperature are such that the ribbon is in compression and the matrix is in tension. As discussed earlier, when the ribbon is heated, stress relief indicated by an inward movement of the fringes is observed due purely to the thermal effect. A schematic description of the shape memory effect on sample displacements is given in Figure 4.7. No actuation takes place until the austenite start temperature A_s . As the temperature increases beyond A_s , the ribbon starts to contract, further relieving the stresses until a temperature $T_c < A_f$, when the residual stresses completely relax. Further increase in temperature results in stress buildup due to actuation.



(a)



(b)



(c)

Figure 4.6. Photoelastic images of annealed SMA sample at different temperatures: (a) $T = 25^{\circ}\text{C}$, (b) $T = 50^{\circ}\text{C}$ and (c) $T = 80^{\circ}\text{C}$.

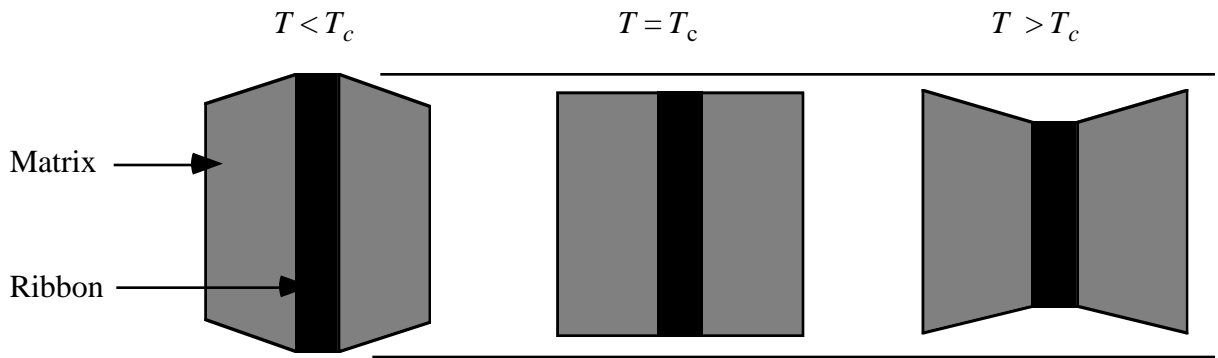


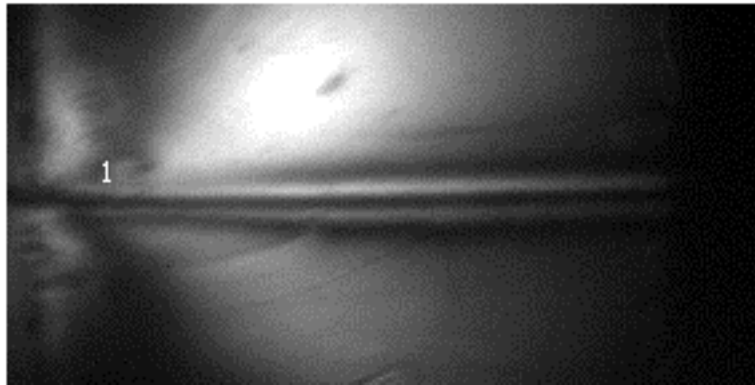
Figure 4.7. Schematic description of the effect of actuation in high temperature cure SMA ribbon composites.

The matrix is subject to compression from the actuating ribbon, which is now under tension. The shear stresses observed in the matrix change direction at a temperature T_c and an outward movement of the fringes is observed. However, for the sample geometry and the loading conditions considered, the ribbon acts as a heat source and the entire sample is not heated uniformly. Therefore, stress buildup takes place in some regions of the matrix before stresses are relieved in other areas. The resulting stress field is difficult to analyze. For the annealed SMA sample in Figure 4.6, a slight outward movement of the fringes occurs near point A, indicating stress buildup, while there is hardly any movement near the center of the sample. The slight outward movement is attributed to the residual shape memory effect in the annealed sample.

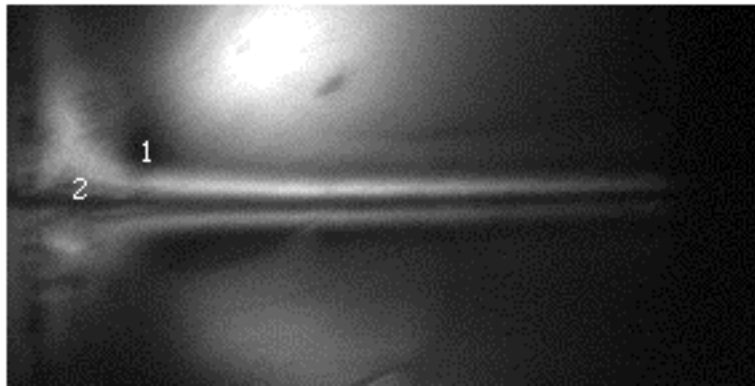
The stress buildup is much more obvious in the two-way trained sample shown in Figure 4.8. The single residual fringe in Figure 4.8 (a) moves outward towards the top edge of the sample and a second fringe starts to appear in Figure 4.8 (b) and is clearly visible in Figure 4.8 (c). However, a complete stress relief followed by a stress buildup was not observed. It was difficult to differentiate between the residual fringes and the fringes due to stress buildup. Therefore, while the shape memory effect is clearly observed in the two-way trained ribbons, the stress contour values are difficult to tabulate and compare with theoretical models.

4.4 Load Transfer—Room Temperature Cure Matrix

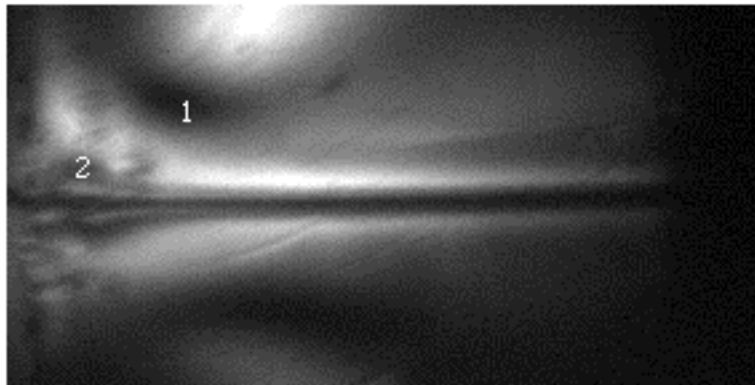
The behavior of SMA ribbons in high temperature cure matrices is complicated by the presence of a residual stress field. An alternative is to embed the SMA ribbons in a room temperature cure matrix. Room temperature cure composites have negligible residual stresses. Therefore identification of fringes due to SMA actuation becomes more straightforward. The disadvantage of room temperature cure materials is that most have a glass transition temperature T_g of about 55°C. The matrix will undergo viscoelastic stress



(a)



(b)



(c)

Figure 4.8. Photoelastic images of two-way trained sample at different temperatures: (a) $T = 25^{\circ}\text{C}$, (b) $T = 50^{\circ}\text{C}$ and (c) $T = 80^{\circ}\text{C}$.

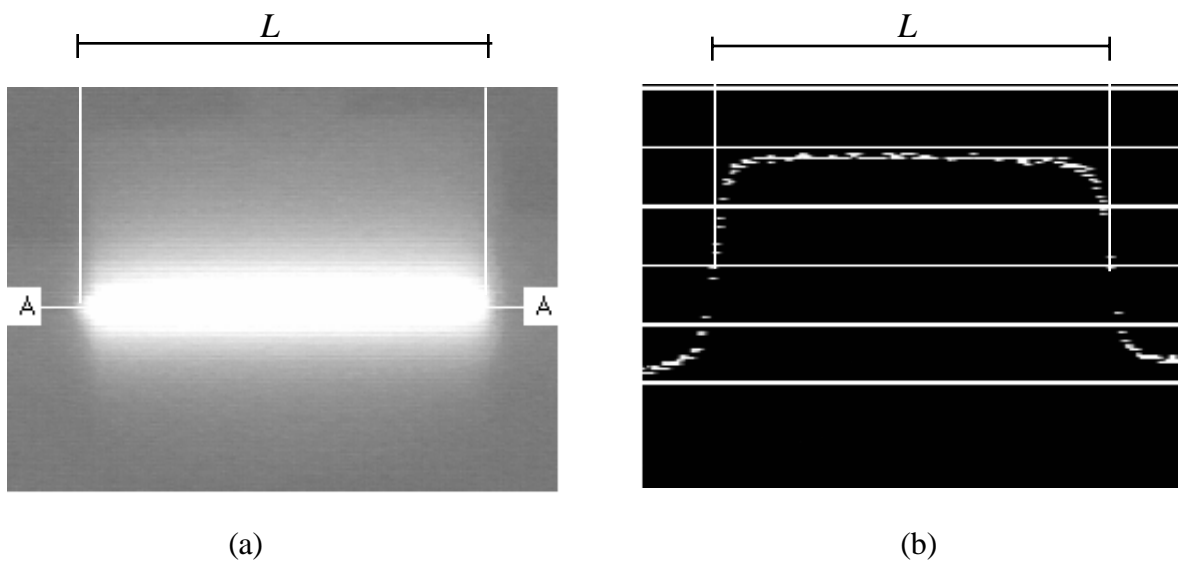
relaxation at around 48°C. Table 4.2 shows that the austenite finish temperature A_f for the SMA ribbons is 57°C. Therefore, it is not possible to induce complete transformation in the ribbon without relaxing the matrix. For the experiments described in this section, the ribbons were heated to a maximum of about 48°C.

4.4.1 *Sample Preparation*

The sample geometry and the preparation procedures for room temperature cure composites were similar to those described in Section 4.3.1 except for the matrix curing agent and the cure cycle. Diethylenetriamine (DETA) from Air Products was used as a curing agent. The samples were cured at room temperature for 10 days before polishing and testing. One set of annealed SMA ribbons was subjected to a uniform one-way strain of 1% prior to embedding. Since the SMA ribbons do not actuate during the room temperature cure, they were not two-way trained. Although each sample could be used for only one test run, greater control was obtained over the exact amount of induced strain. Control samples were made with annealed SMA ribbons with no prestrain. Aluminum and processed SMA samples were not fabricated since it was determined from Section 4.3 that their behavior is significantly different from that of annealed samples.

4.4.2 *Heating and Actuation*

For this set of experiments, a temperature profile was measured using a control sample. Variations of temperature along the length of the sample might occur if the ribbon cross-section is nonuniform or if the sample thickness varies significantly. An infrared camera (Inframetrics 525) was used to ascertain if the sample heated uniformly across its length. Figure 4.9 (a) shows an infrared image of the heated control sample. The relative temperature rise across A-A in isotherm units is shown in Figure 4.9 (b). Each horizontal line represents a constant temperature, which depends upon the spectral emissivity of the polymer. The length of the sample, L , is indicated by the vertical lines. The temperature



(a) (b)

Figure 4.9. Heating of SMA ribbons: (a) Infrared image of SMA ribbon sample;
(b) Temperature profile along sample in isotherm units.

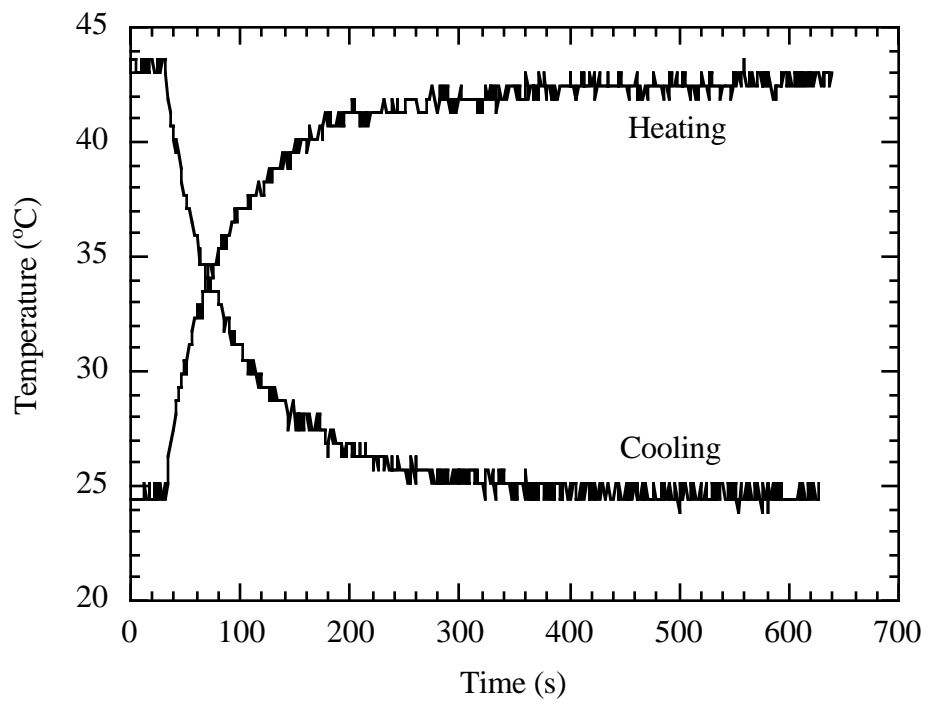


Figure 4.10. Temperature profile on the SMA sample surface adjacent to the ribbon during heating and cooling.

Table 4.2. Material properties of high temperature and room temperature cure epoxy matrices.

Material Property	PACM/Epoxy	DETA/Epoxy
E (GPa)	2.5	2.5
ν	0.33	0.33
α (x $10^{-6}/^{\circ}\text{C}$)	68.0	57.0
K (W/m $^{\circ}\text{C}$)	0.18	0.18
f_{σ} (kN/m)	10.49	15.10
ρ (Kg/m 3)	1350	1350
T_g ($^{\circ}\text{C}$)	130	56

remained uniform across the sample length throughout heating. Due to difficulty in obtaining an accurate value for the emissivity of the polymer matrix, the infrared camera was not used for absolute temperature measurement. To obtain the absolute temperature, a thermocouple was placed on the sample surface above the ribbon and the temperature change with time was recorded using a LabView driven data acquisition board. Figure 4.10 shows that a steady state temperature of 44°C was achieved in approximately 200 seconds.

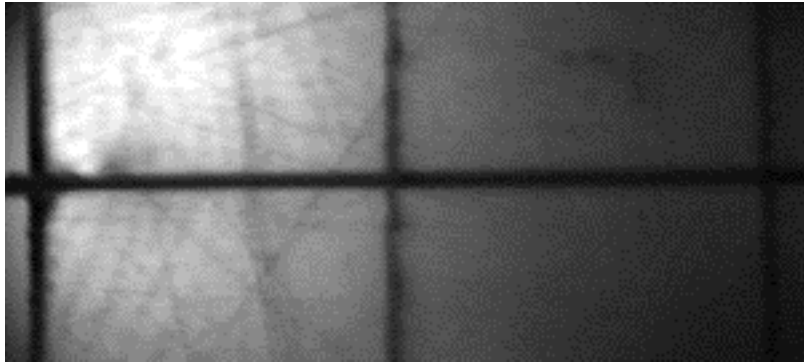
4.4.3 *Experimental Stress Analysis*

In order to separate the purely thermal effects, the control sample with annealed SMA ribbon was heated resistively with a current of 1.55 A. The resulting stress profiles are shown in Figure 4.11 for different time intervals. There are no fringes due to residual stress at time $t = 0$. The vertical line near the center of the image represents the point one-fourth of the length from the edge of the sample. In Figures 4.11 (b) and 4.11 (c), there is negligible fringe development with time. Hence, the stress buildup due to thermal effects are not significant for the given loading conditions.

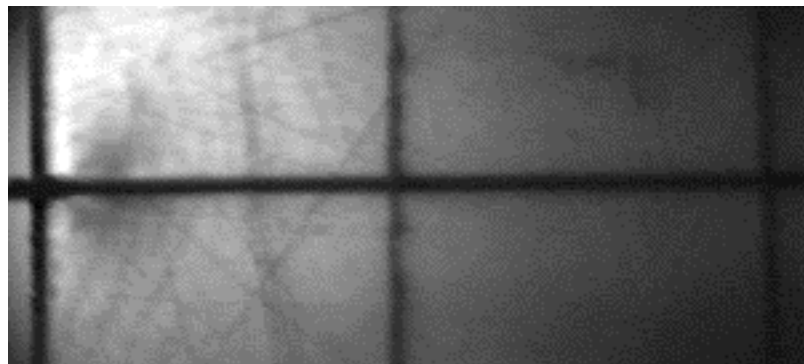
Next, samples with 1% prestrain were actuated. The experimental stress contours are shown in Figures 4.12 (a) to 4.16 (a) for various time intervals. Since experiments with annealed ribbons indicated that the thermal contribution to stress was negligible, it is assumed that stress contours observed are all due to the SMA effect. The numerical values of the stresses are calculated using the stress optic law

$$\sigma_1 - \sigma_2 = \frac{Nf_\sigma}{h} \quad (4.1)$$

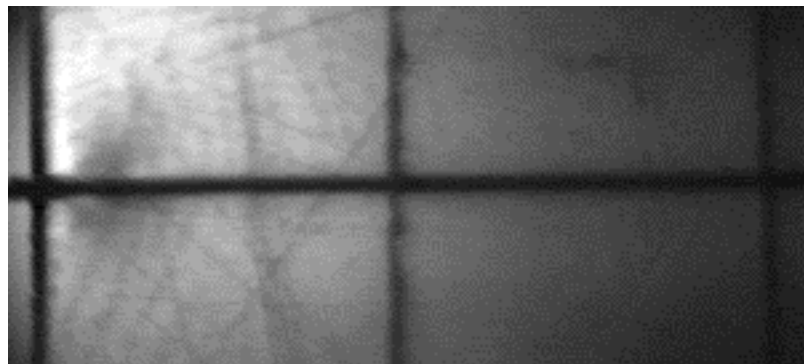
where N is the fringe order, f_σ is the material fringe value given in Table 4.1 and h is the thickness of the sample. The $\sigma_1 - \sigma_2$ contours for the top half of the symmetric



(a)

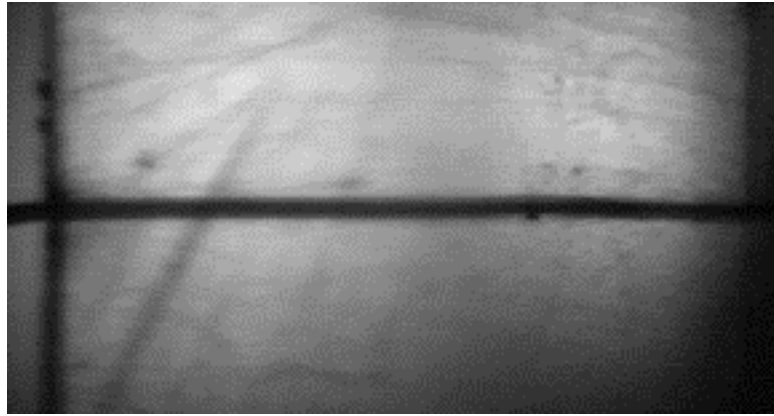


(b)

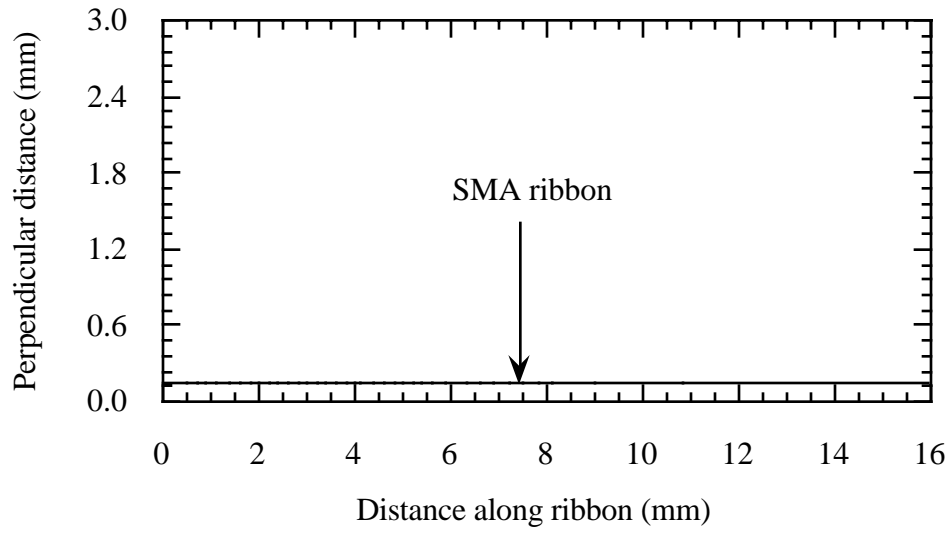


(c)

Figure 4.11. Photoelastic images of room temperature cured SMA ribbon composites at various times: (a) $t = 0$; (b) $t = 120$ s; (c) $t = 240$ s.

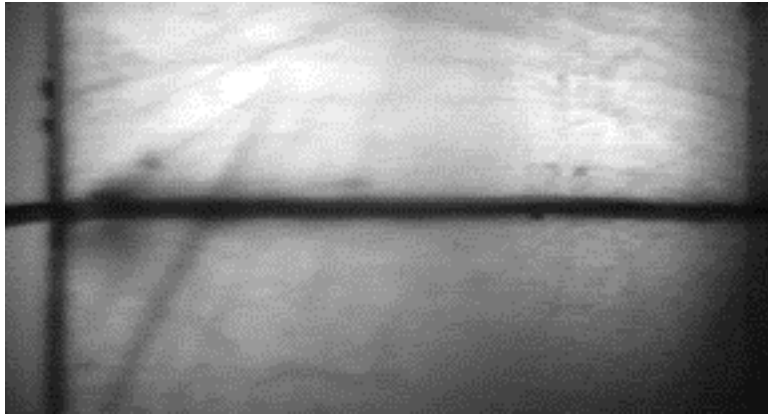


(a)

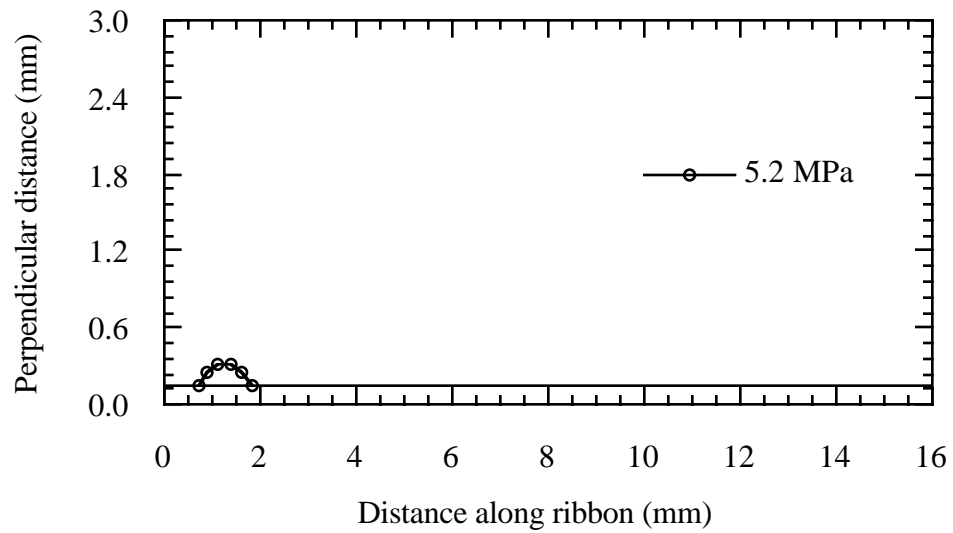


(b)

Figure 4.12. (a) Photoelastic stress contours for 1% prestrained sample at time $t = 0$; (b) Locations of stress contours for the symmetric top half of the photoelastic image.

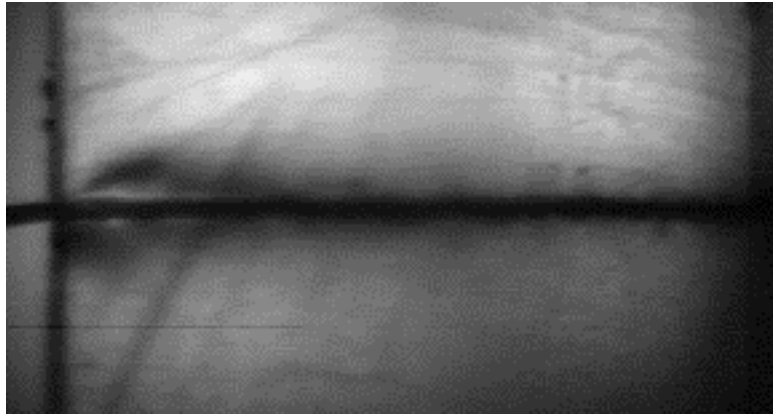


(a)

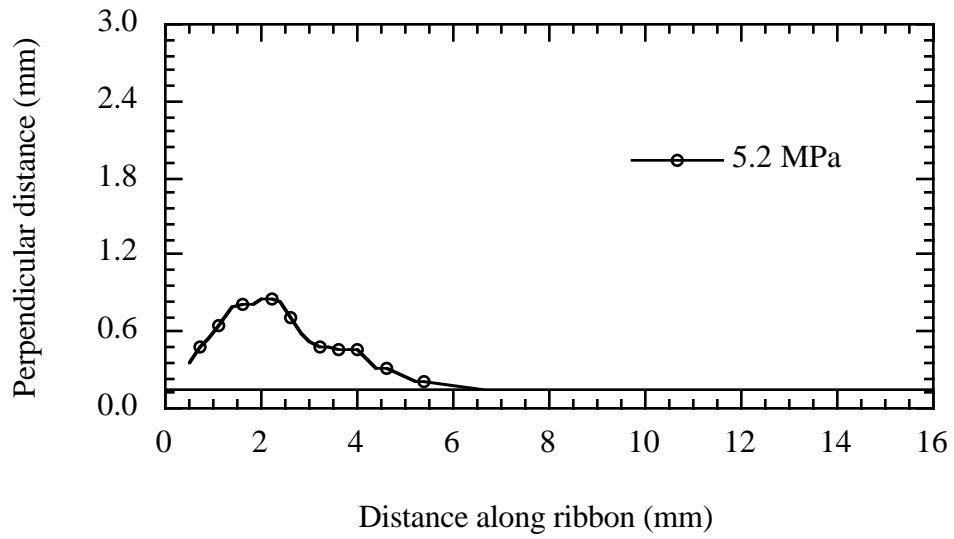


(b)

Figure 4.13. (a) Photoelastic stress contours for 1% prestrained sample at time $t = 60$ s;
 (b) Locations of stress contours for the symmetric top half of the photoelastic image.

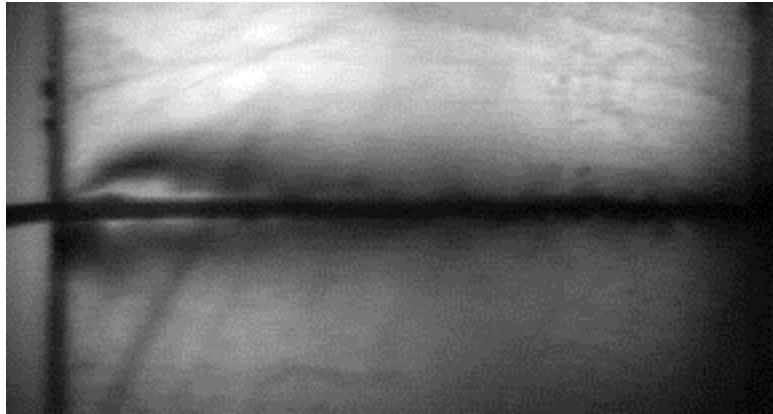


(a)

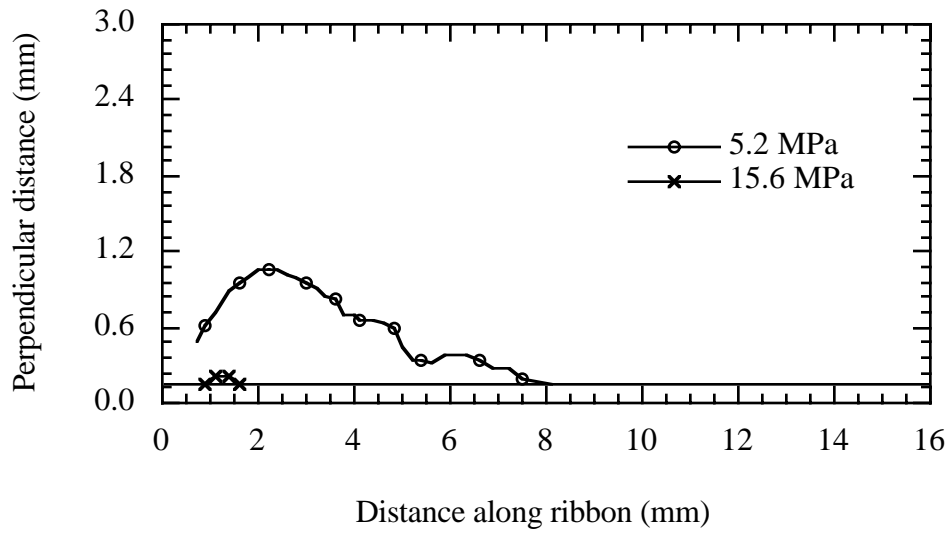


(b)

Figure 4.14. (a) Photoelastic stress contours for 1% prestrained sample at time $t = 120$ s;
(b) Locations of stress contours for the symmetric top half of the photoelastic image.

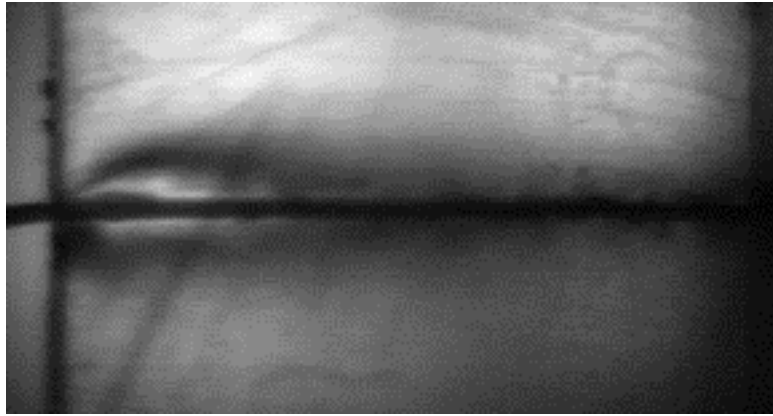


(a)

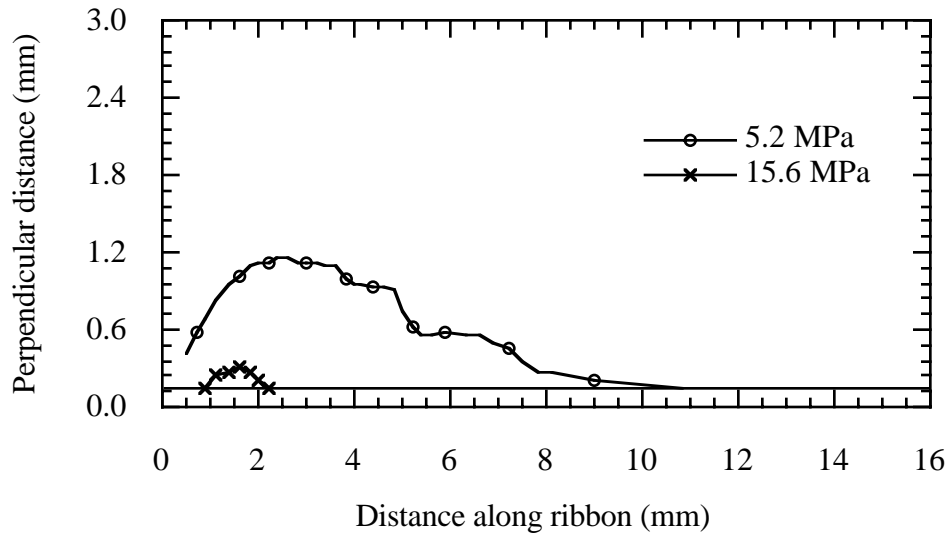


(b)

Figure 4.15. (a) Photoelastic stress contours for 1% prestrained sample at time $t = 180$ s;
 (b) Locations of stress contours for the symmetric top half of the photoelastic image.



(a)



(b)

Figure 4.16. (a) Photoelastic stress contours for 1% prestrained sample at time $t = 240$ s; (b) Locations of stress contours for the symmetric top half of the photoelastic image.

photoelastic images are plotted in Figures 4.12 (b) to 4.16 (b) for different time intervals. Accurate determination of the locations of the fringes was made using an image analysis program (Image V1.49 from NIH). A stress contour of 5.20 MPa starts out at the edge of the sample and moves towards the center of the sample from the edges and outward from the ribbon. A second stress contour of 15.62 MPa is first observed in Figure 4.15 at $t = 180$ s. With increasing time, this contour moves slightly outward from the ribbon as seen from Figure 4.16 at $t = 240$ s. The data provide transient stress profiles for a simple geometry and are therefore ideal for comparison with theoretical models.

4.5 Conclusions

Photoelasticity was used to study the transient stress profiles of SMA ribbons in high temperature cure and low temperature cure matrices. The response of annealed and embedded SMAs showed significant differences when compared with the behavior of embedded aluminum and processed SMAs in high temperature cure matrices. The residual stresses were lower for annealed SMAs due to the self-accommodation of martensite. The nonuniform reversal in shear stress direction in the host material made analysis of the experimental data from high temperature composites difficult.

Transient stress profiles were obtained for annealed SMA ribbons and 1% prestrained SMA ribbons in a room temperature cure matrix. The stress contours were quantified and plotted for different time intervals. Actuation of annealed SMA ribbons indicated that the thermal contribution to stress was not significant compared with the stresses induced due to the shape memory effect. The simple sample geometry along with the transient stress and temperature data provide an ideal benchmark for evaluating theoretical models.

5. IN-PLANE DISPLACEMENT

Quantitative measurements of load transfer from an SMA ribbon to a polymer matrix were obtained by photoelasticity as discussed in Chapter 4. The objective of the experiments outlined in the current chapter is to obtain whole-field displacement data for samples similar to those used for photoelasticity. Displacements provide an independent set of data for evaluation of theoretical models and also complement the stress values obtained using photoelasticity. Further, since the thermal and SMA displacements are opposite in direction, whole-field displacements can be used to obtain the location of the phase transformation front at a particular temperature.

Moiré interferometry has been widely used to obtain in-plane displacement measurements in diverse applications (Post, Han and Ifju, 1994). To the knowledge of the author, it has not been applied to the study of SMAs and SMA composites. In this chapter, the moiré technique is adapted to obtain whole-field displacement measurements of SMA ribbons embedded in an epoxy matrix.

5.1 Principle of Moiré Interferometry

When a beam of light is directed onto a reflective diffraction grating, the reflected beams emerge along certain preferred directions as shown in Figure 5.1. The preferential angles of the emerging wavefronts are given by

$$\sin \beta_m = \sin \alpha + m\lambda f \quad (5.1)$$

where m denotes the order of a particular diffracted wavefront, β_m is the angle normal to diffracted wavefront m , α describes the angle of the light incident to the grating surface, λ is the wavelength of both incident and diffracted light, and f denotes the frequency of

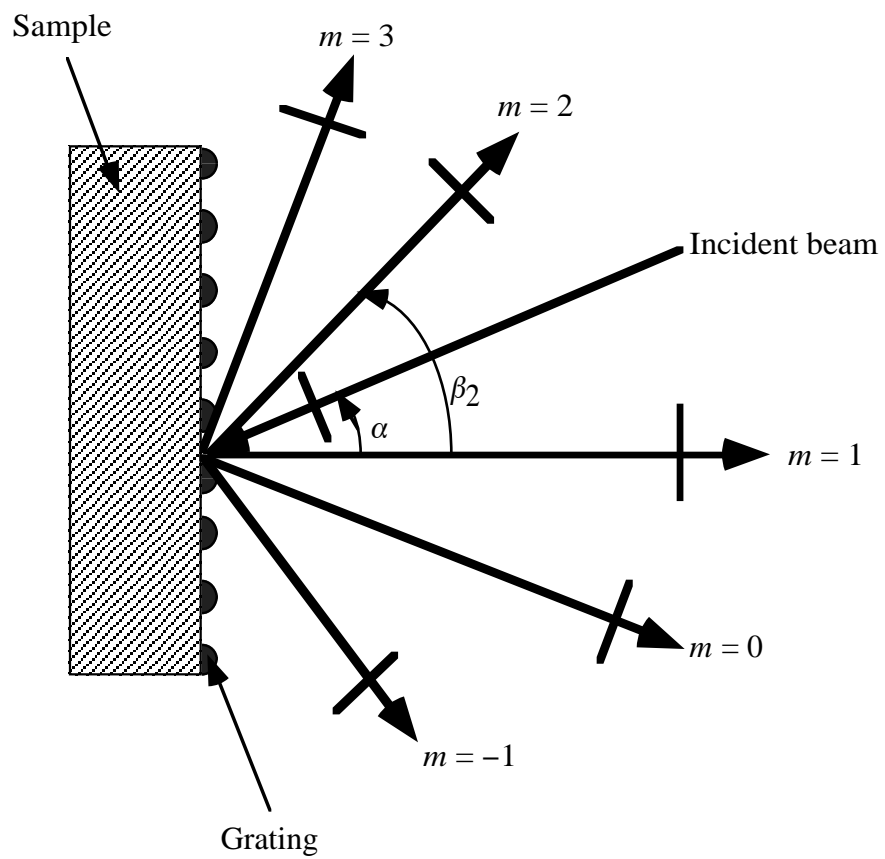


Figure 5.1. Diffraction from a reflective grating.

the grating. The α and β_m angles are measured from the normal to the grating surface with counterclockwise being positive. Diffraction orders whose angles are counterclockwise with respect to the zero order are considered positive as seen in Figure 5.1. Frequency of the grating is indicated by the number of grating lines per unit length.

The basic principle of moiré interferometry is schematically illustrated in Figure 5.2. A reflective grating is placed on the sample to be tested. When two mutually coherent beams of light with angle of incidence α reflect off the grating surface as shown in Figure 5.2, they interfere to form moiré fringes. The angle α is chosen as

$$\alpha = \sin^{-1}\left(-\frac{\lambda f}{2}\right). \quad (5.2)$$

Substitution of this value of α into Equation (5.1) shows that the +1 diffraction order from beam 1 and -1 diffraction order from beam 2 travel perpendicular to the grating surface ($\beta_1 = \beta_2 = 0$). The lens in Figure 5.2 is used to focus the image of the interference at the grating surface onto a photographic film or a CCD camera. For an undeformed grating, the phase difference between the +1 and -1 diffracted wavefronts remains constant, producing a uniformly bright or dark image on the film plane. This image is referred to as the null field. In practice, the size and focal length of the lens are chosen to cause diffraction orders other than +1 or -1 to miss the lens and not create additional interference.

The relationship between grating surface deformation and interference can be described by the displacement of a point on the grating surface as shown by Post, Han, and Ifju (1994). Figure 5.3 depicts the motion of point P on the grating surface in relation to

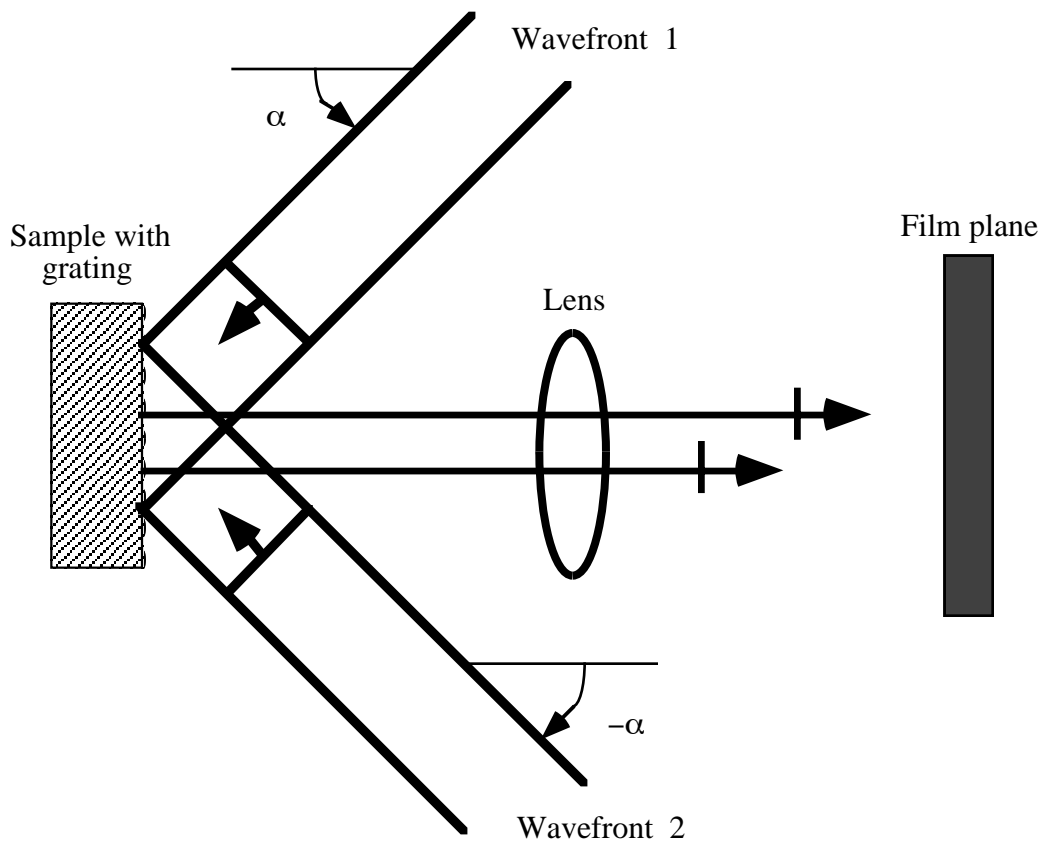
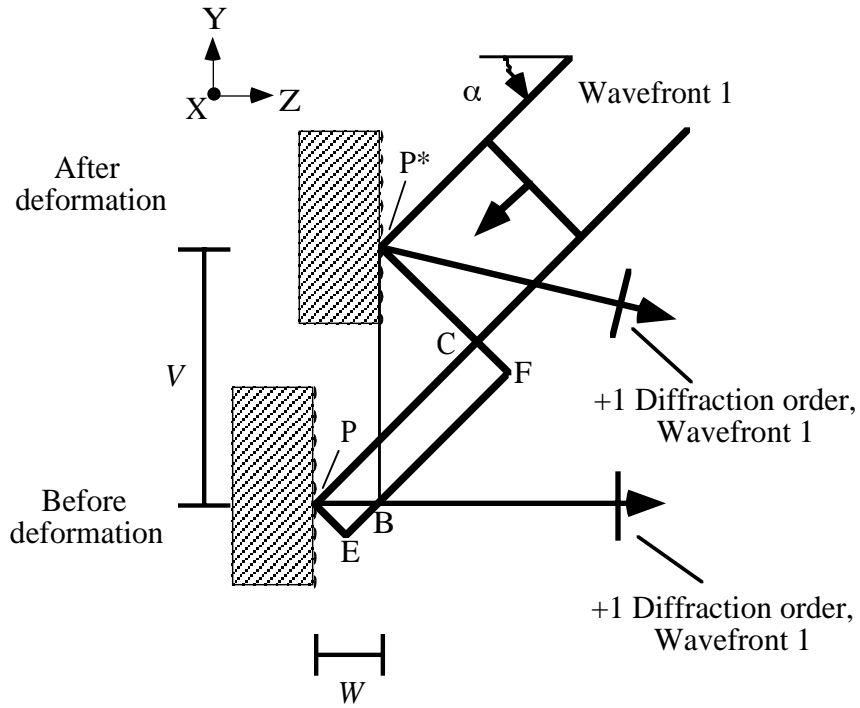
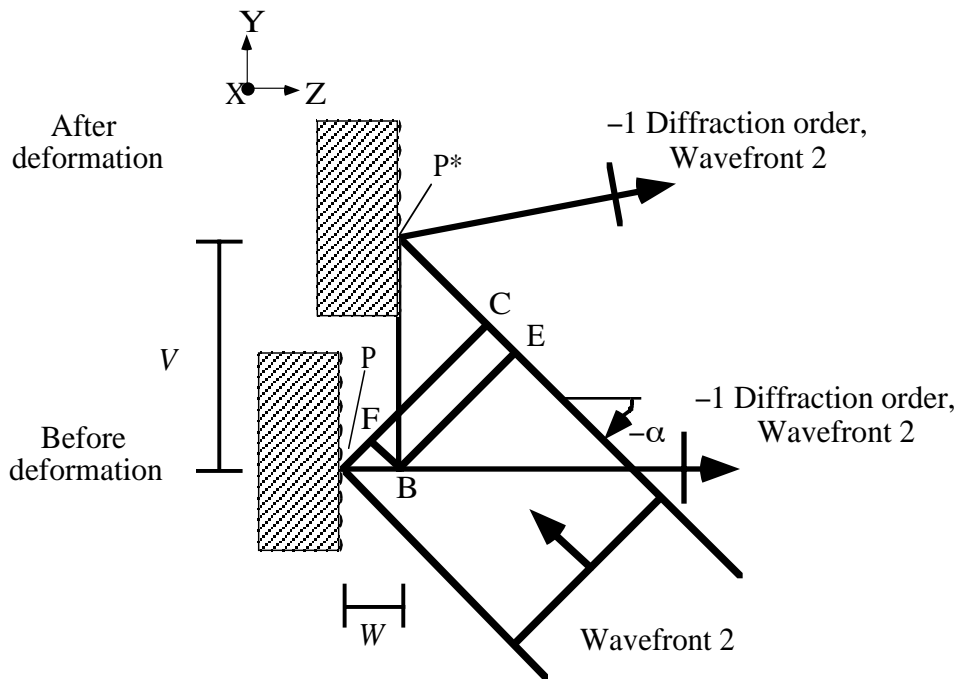


Figure 5.2. Principle of moiré interferometry.



(a)



(b)

Figure 5.3. Change in optical path length with deformation:

(a) Wavefront 1; (b) Wavefront 2.

the changes of optical path length from beam 1 and beam 2. The optical elements between the grating surface and the film plane do not influence optical path length (OPL). Therefore, the intensity depends on the changes in OPL up to and not after the point P on the grating surface. From Figure 5.3 (a), the change in OPL for beam 1 is given by

$$\Delta\text{OPL}_1 = \text{CP} + \text{PB}. \quad (5.3)$$

Equation (5.3) can be simplified to express the change in OPL in terms of the displacements V and W and the incident angle α as

$$\Delta\text{OPL}_1 = W(1 + \cos \alpha) + V\sin \alpha. \quad (5.4)$$

Similarly, the change in optical path for beam 2 in Figure 5.3b is given by

$$\Delta\text{OPL}_2 = W(1 + \cos \alpha) - V\sin \alpha. \quad (5.5)$$

Therefore, the difference between the path lengths of the two beams is

$$\Delta\text{OPL}_1 - \Delta\text{OPL}_2 = 2V\sin \alpha. \quad (5.6)$$

The change in the OPL between the two beams is independent of the out-of-plane displacement W . The phase difference between the two beams depends on the difference between ΔOPL_1 and ΔOPL_2 plus a constant of separation from the null field. Consequently, the phase difference depends on the deformation of the grating. The relation between fringe order and displacement can be expressed as (Post, Han and Ifju, 1994):

$$V = \frac{1}{f_v} \left(N_y + \frac{k}{\lambda} \right) \quad (5.6)$$

where f_v is the virtual grating frequency, which is chosen equal to $2f$, k is a constant and N_y is the fringe order in the V -field. The term $k\lambda/f_v$ is equivalent to a uniform displacement throughout the field, or a rigid body translation. While studying deformations, rigid body motion is neglected to yield

$$V = \frac{1}{f_v} N_y. \quad (5.7)$$

To characterize more complex sample deformation, crossed line diffraction gratings are used to provide information about displacements U and V in the x and y directions, respectively. In practice, the crossed line grating allows pairs of incoming laser beams to produce fringe patterns of U and V deformation in succession either by using a four beam interferometer or by rotating the sample by 90° when using a two beam interferometer. The separate U and V field fringe patterns provide information about the displacement of every point in the images relative to every other point. The expression for the x direction displacement is given by

$$U = \frac{1}{f_v} N_x \quad (5.8)$$

where N_x denotes the fringe order in the U -field.

5.2. Sample Preparation

Room temperature cured samples of SMA ribbons in epoxy were prepared by the procedure described in Section 4.4.1. Diethylenetriamine (DETA) was used as a curing agent for the epoxy matrix (EPON 828). Two sets of samples with annealed SMA ribbons and 1% prestrained SMA ribbons were fabricated. The sample geometry was similar to that of the photoelastic samples. A schematic of the sample is shown in Figure 5.4. The

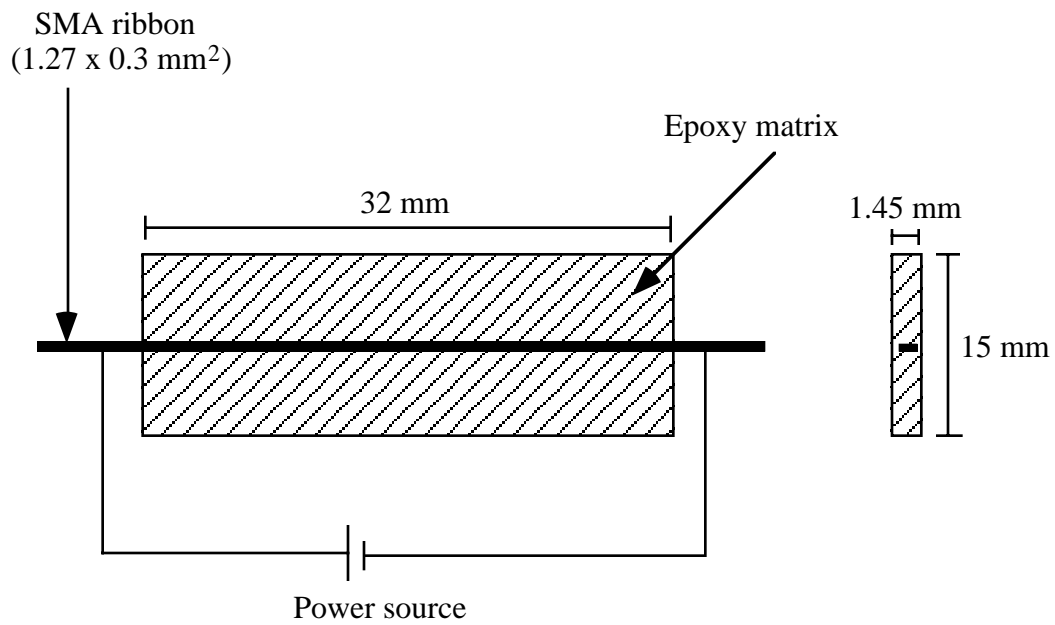


Figure 5.4. Schematic of sample for moiré interferometry.

height of the sample was reduced from 32 mm to 15 mm so that the surface area of the sample, and therefore, the size of the grating to be put on the sample was reduced. The embedded ribbon length and the thickness of the sample remained at 32 mm and 1.45 mm respectively.

Diffraction gratings were applied, using the technique described by Post, Han, and Ifju (1994), to the samples. First, a submaster of a 1200 lines/mm cross lined master grating was replicated using GE RTV 615 silicone rubber. The silicone rubber was degassed in a vacuum jar for approximately ten minutes until all visible air bubbles had collapsed. A 3 cm diameter pool of the degassed silicone rubber was then poured on a clean and primed glass plate. The master grating was pressed onto the silicone rubber for replication. After allowing the RTV 615 to cure for 24 hours, the master and submaster were separated by the fixture shown in Figure 5.5. The fixture permitted the controlled separation of the gratings while minimizing the bending loads on the glass plates. The fixture was designed by Stout (1997) based on an original design by Post, Han, and Ifju (1994). The silicone rubber submaster was then replicated in the same fashion by using Envirotex-Lite brand epoxy.

The epoxy grating was coated with aluminum through vacuum evaporation deposition. After evaporating one coat of aluminum onto the epoxy grating, a solution of Kodak Photo-flo 200, diluted 1:200 in distilled water, was applied. The Photo-flo solution acted as a separating agent between the first layer of aluminum and a second layer, which was evaporated onto the grating after the solution had dried fully. This second grating layer was then transferred to the samples by spreading a thin degassed layer of Envirotex-Lite epoxy onto the samples with the wooden end of a swab and placing the sample onto the grating. The orientation of the grating lines required that the perimeter of the specimens

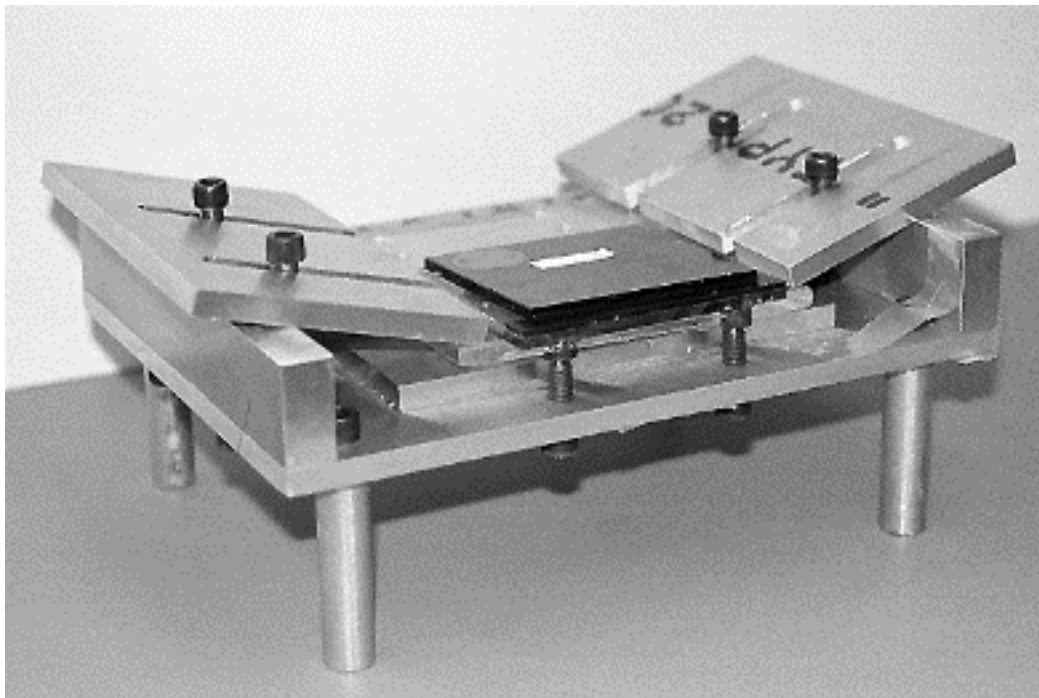


Figure. 5.5. Photograph of grating separation fixture.

be square with respect to the edges of the grating. In this way, moiré fringes corresponded to displacements along the major and minor axes of the specimen.

5.3 Experimental Setup and Procedure

A compact four beam interferometer (PEMI 2001-X, IBM Corp.) was used for the experiments. A schematic of the optical arrangement in the interferometer is given in Figure 5.6. A cross line grating is used to split a beam from a 632 nm He-Ne laser source into four separate coherent beams of light. Beams from mirrors A and C are used to obtain the U field and beams from mirrors B and D are employed to obtain the V field. The angle of incidence of the beams onto the sample, α , is 49.4 degrees. The resulting frequency of the virtual grating in the interferometer f_v is 2400 lines/mm, twice the sample grating frequency. Post, Han and Ifju (1994) provide a detailed description of the instrument. Samples were positioned within the 45 mm diameter viewing field of the compact four beam interferometer using an x-y table, rotation stage, and screw adjustments on the interferometer. A pneumatic optical table isolated the entire assembly from ambient vibration. Moiré images were recorded by a CCD camera (Panasonic BL200) connected to a VCR (Mitsubishi U82). Recorded images were copied for analysis using a 640 pixel by 480 pixel frame grabber.

The fixtures to hold the sample during actuation were designed to minimize any effect on the movement of the SMA ribbon. After experimenting with a number of possible designs, the fixtures shown schematically in Figure 5.7 were adopted. The sample was fastened in the center on the bottom side and mounted on a rotation stage. Additional stages were incorporated for aligning the sample in the interferometer. The fixtures were thermally insulated. Actuation was accomplished by resistively heating the ribbons to different temperatures. The motion of the ribbon was monitored only in the axial direction using the U -field setting.

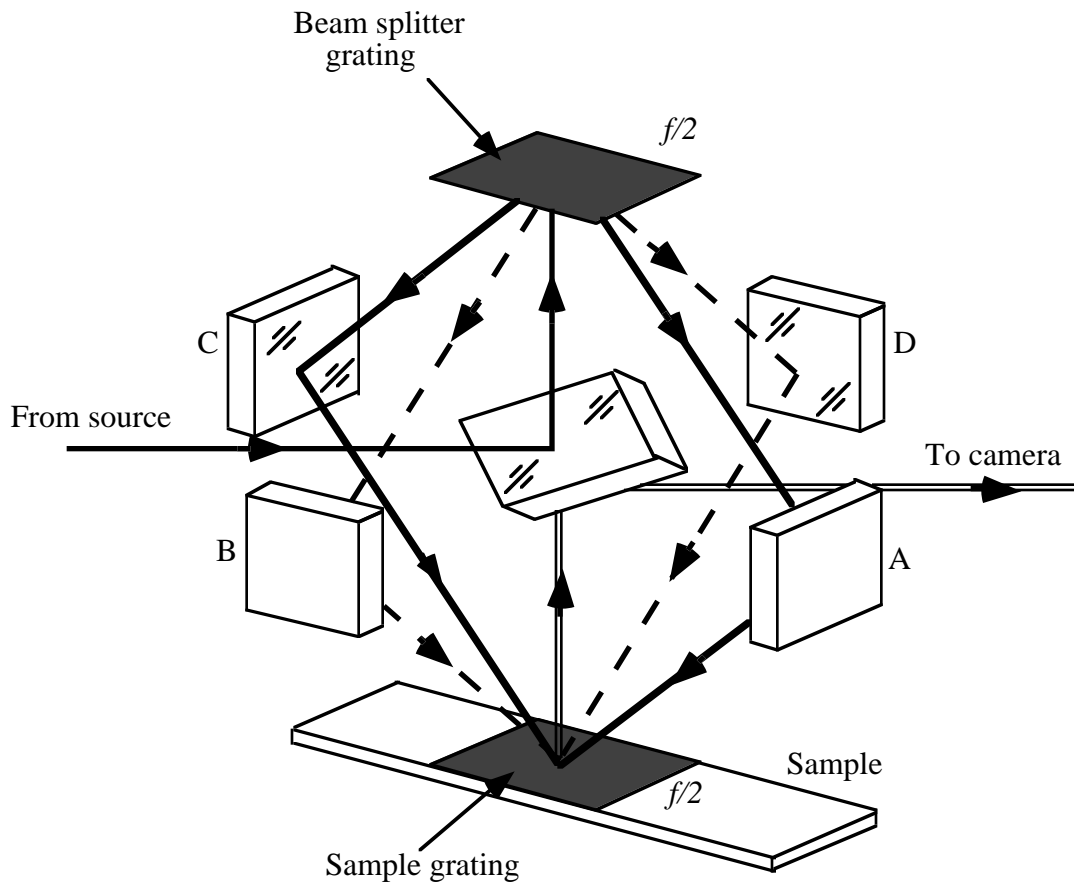


Figure 5.6. Schematic illustration of the moiré interferometer.

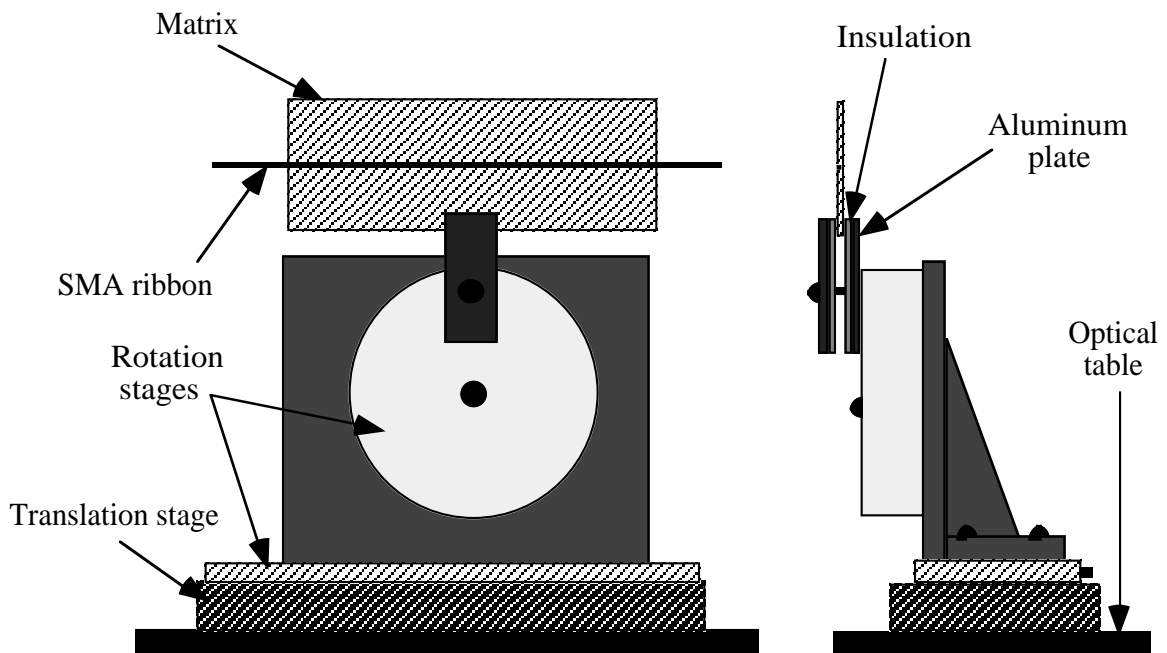


Figure 5.7. Schematic illustration of sample fixtures.

5.4 Displacement Measurements Using Moiré Interferometry

5.4.1 Temperature Measurements

The samples were prepared using a room temperature cure matrix as discussed in Section 5.2. The advantage of the room temperature cure system is that only minimal residual stresses are generated in the sample prior to loading. Residual stresses increase the transformation temperatures in the ribbon, complicating the sample response upon heating. The disadvantage of room temperature cured polymers is that they have a low glass transition temperature—about 55°C for the DETA/epoxy system. Viscoelastic relaxation of the matrix starts to occur at approximately 48°C. The austenite finish temperature of the ribbon is 57°C (Table 4.1). Therefore, the ribbon cannot be actuated completely without relaxing the matrix. As the ribbon is heated to above the austenite start temperature, the amount of phase transformation induced in an SMA is proportional to the temperature to which it is raised. As the steady state temperature is increased by increasing the power input, a greater portion of the SMA is transformed to austenite.

Accurate measurements of temperatures for different power inputs are necessary for correlating the amount of transformation with temperature. It was demonstrated in Section 4.4.2 that a current input of 1.55 A raises the temperature of the sample surface to 44°C. Temperature profiles were acquired for current inputs of 1.50 A and 1.65 A in addition to 1.55 A. Thermocouples were placed on the sample surface above the ribbon and the temperature change with time was recorded using a LabView driven data acquisition board. Figure 5.8 shows that steady state temperatures of 42.5°C, 44°C and 47°C are attained for current inputs of 1.50 A, 1.55 A and 1.65 A, respectively.

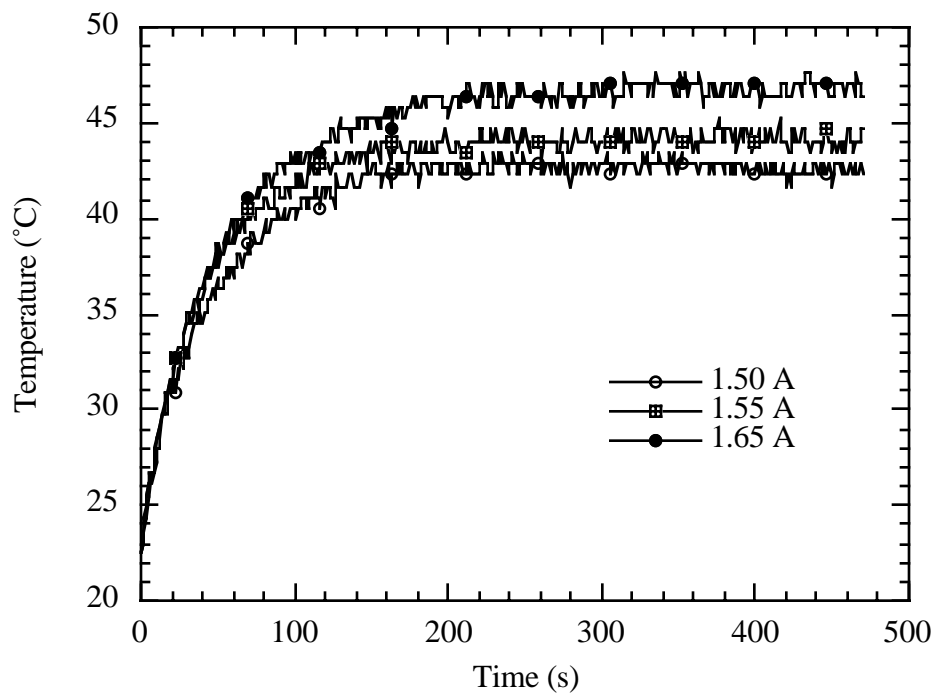
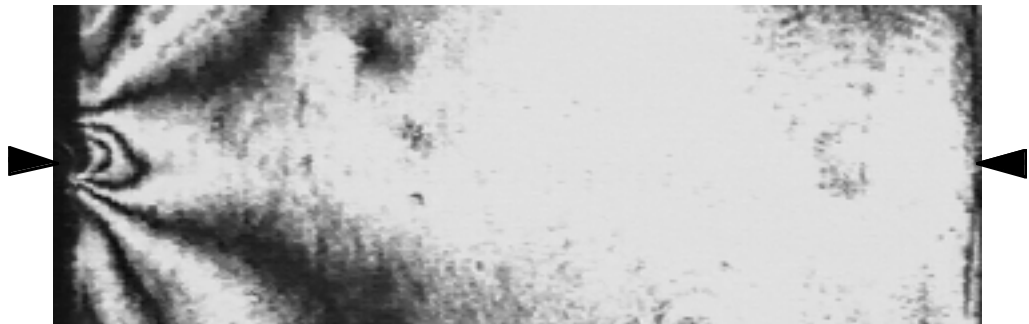


Figure 5.8. Temperature profiles of the sample surface at different power inputs.

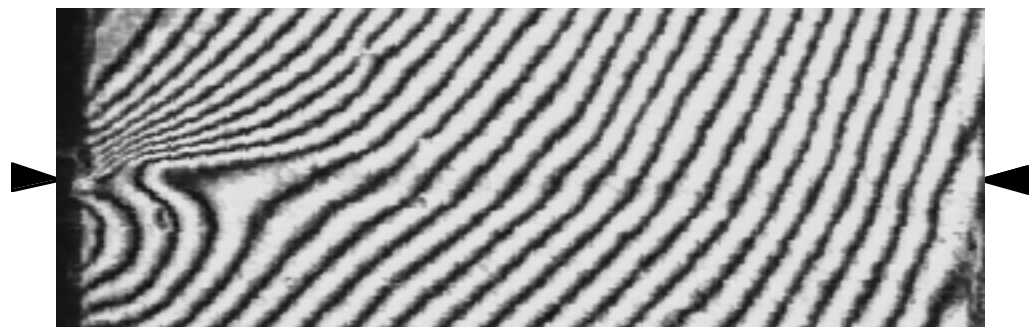
5.4.2 *Steady State Displacements*

Annealed SMA ribbon samples were tested first using a current input of 1.50 A. Annealing mitigates the stresses induced during processing and very little shape memory effect is observed in the ribbons unless they are prestrained or two-way trained. Figure 5.9 shows the moiré fringe patterns of an annealed ribbon sample, prior to heating, at steady state temperature, and after cooldown. The knife edges at the side of each figure mark the location of the ribbon in the sample. Due to symmetry, only half of the sample is shown in all the images. Figure 5.9 (a) shows that there are very few fringes in the sample prior to heating. This initial fringe pattern is referred to as the null field. The power was switched on and the sample slowly heated to a steady state temperature of 42.5°C. The fringe pattern corresponding to the steady state temperature is shown in Figure 5.9 (b). The power was then switched off and the sample was allowed to cool to room temperature. Figure 5.9 (c) shows the moiré fringes on the sample after complete cooldown to room temperature. Most the fringes observed at steady state dissipate on cooldown, and the final fringe pattern is very similar to the null field. No residual fringe pattern is observed in the annealed ribbon samples. At steady state, there is a lack of symmetry in the fringes about the ribbon axis. A higher density of fringes is observed near the top of the sample image than at the bottom. This lack of symmetry occurs because the bottom fixture absorbs some heat by conduction and lowers the sample temperature around it. The top of the sample loses heat by convection only. Even though a thin layer of insulation was used between the sample and the fixture, the fixture acts as a heat sink.

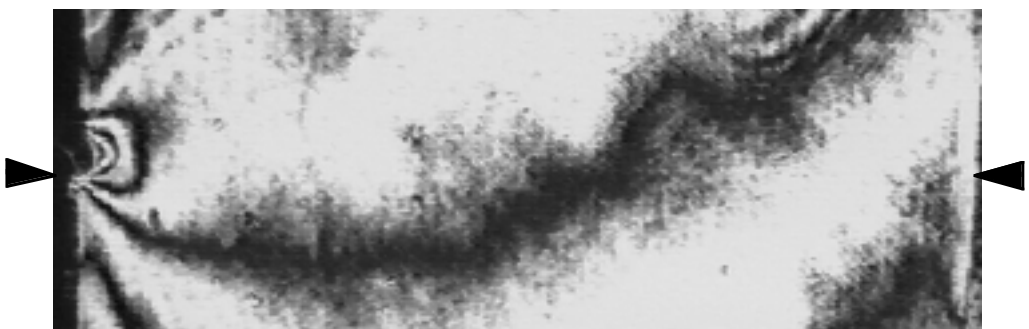
The images from Figure 5.9 were analyzed and the displacements at steady state were determined. The fringes at null field were accounted for in the displacement calculations. Displacement values along the ribbon, from the edge to the center of the sample, are plotted in Figure 5.10. The edge of the sample was treated as the origin for the plots. A steady state finite element model was developed for the sample geometry. The



(a)



(b)



(c)

Figure 5.9. Moiré images of annealed ribbon sample with a current input of 1.50 A:
(a) Prior to heating; (b) At steady state temperature; and (c) After cooldown.

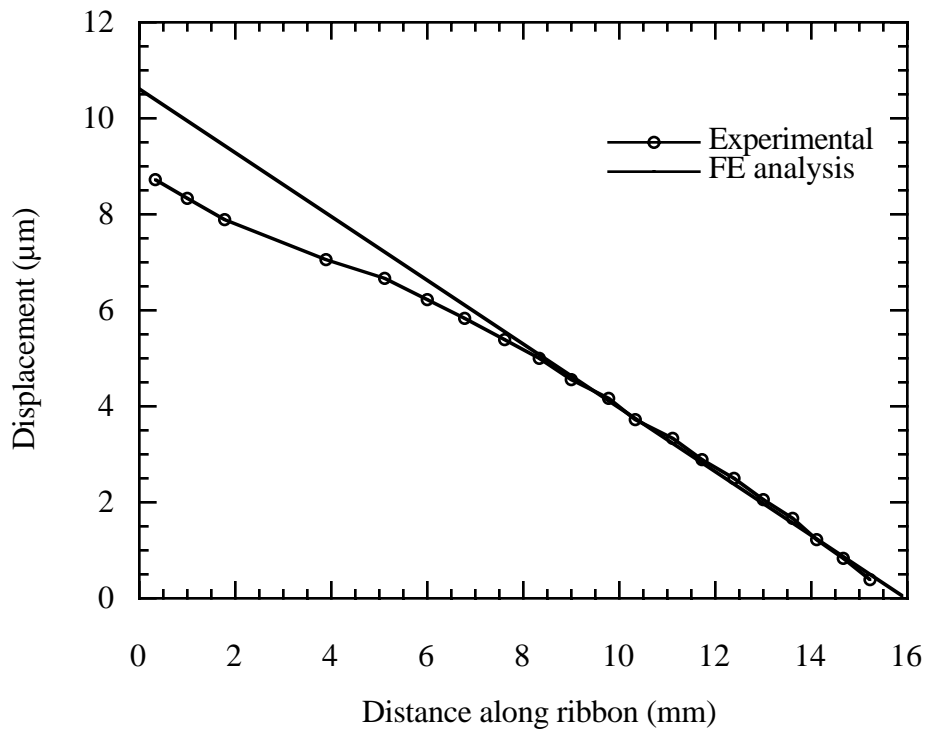
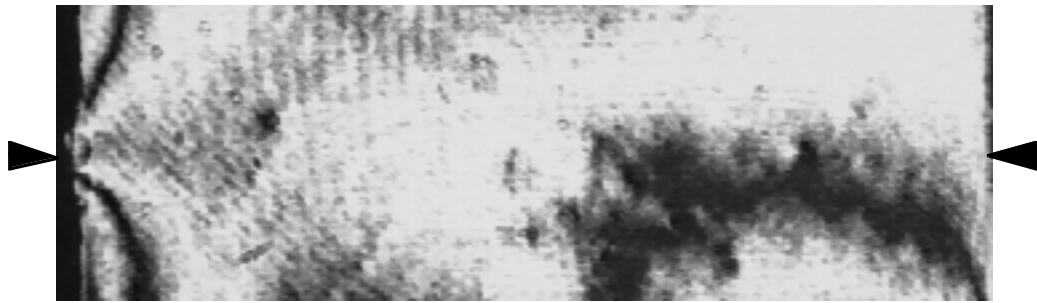


Figure 5.10. Displacement profile of annealed SMA ribbon with a power input of 1.50 A at steady state temperature.

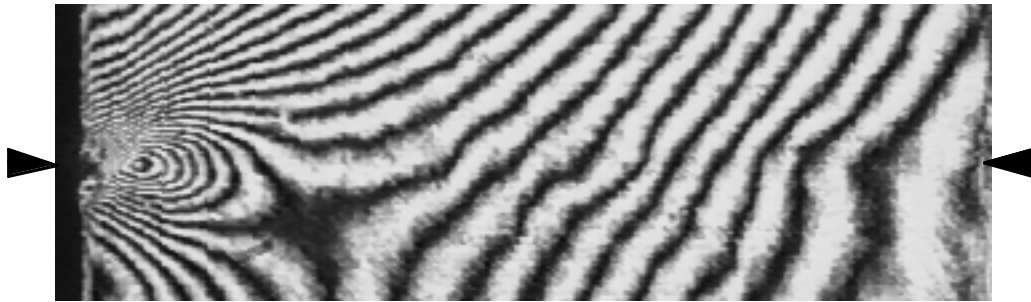
plane stress approximation was used and displacements were calculated using the material properties given in Tables 4.1 and 4.2. Figure 5.10 shows that the finite element solution is in good agreement with the experimental displacement contour except towards the edge of the sample. The deviation is due in part to a debond of approximately 1 mm at the edge of the sample that was not accounted for in the theoretical solution. Small amounts of residual shape memory effect in the annealed ribbons could also contribute to the lower displacements.

Next, 1% prestrained ribbon samples were actuated with a current input 1.50 A. The fringes in the null field, at a steady state temperature, and after complete cooldown of the sample, are shown in Figure 5.11. A clear distinction is observed between the fringe patterns of prestrained ribbons and those of annealed ribbons. Unlike the patterns for annealed ribbons, a saddle point is observed in Figure 5.11 (b), indicating a local maximum or minimum. Lack of thermal symmetry due to the sample fixture causes the saddle point to be located below the ribbon axis. Distinct residual fringes appear in the prestrained samples after cooldown, as seen from Figure 5.11 (c). The resulting fringe pattern in Figure 5.11 (c) is quite different from the null field in Figure 5.11 (a) and indicates a one-way transformation of the SMA ribbon. The fringes were analyzed and the displacement profiles are plotted in Figure 5.12. The displacement contour at steady state temperature shows a maximum displacement of $3.95 \mu\text{m}$ at a distance of 4.7 mm from the edge of the sample. A maximum residual displacement of $-1.67 \mu\text{m}$ is observed near the edge of the sample after cooldown.

The fringe patterns in Figures 5.11 (b) and 5.11 (c) when compared with those for the annealed sample in Figure 5.9 clearly demonstrate that phase transformation takes place in the prestrained ribbons. Most of the transformation is restricted to the edge of the sample for the given power input. From a study of dynamic response of an SMA



(a)



(b)



(c)

Figure 5.11. Moiré images of 1% prestrained ribbon sample with a current input of 1.50 A:

(a) Prior to heating; (b) At steady state temperature; and (c) After cooldown.

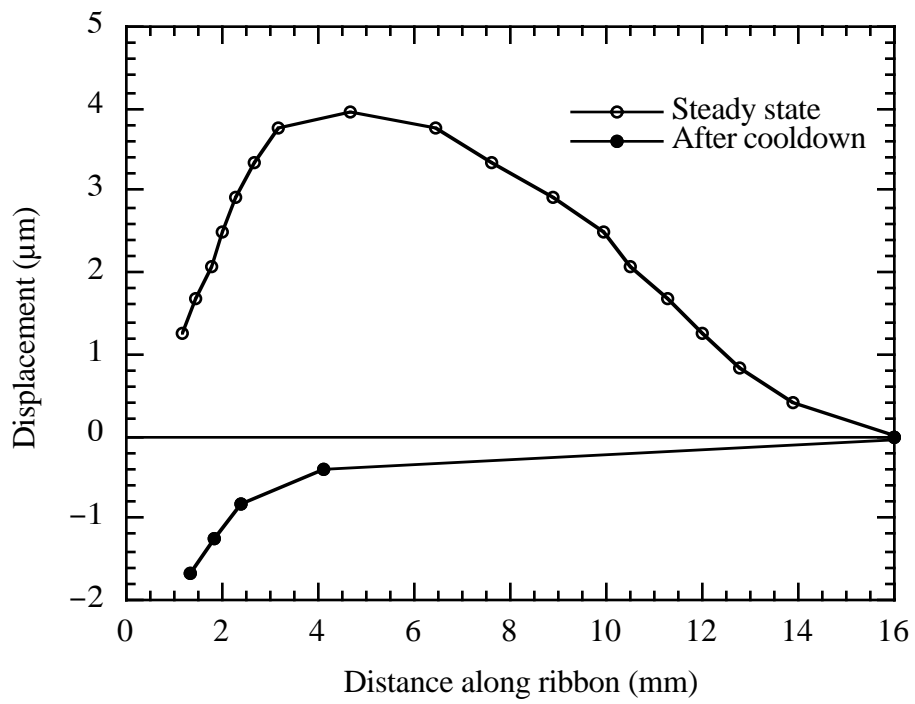
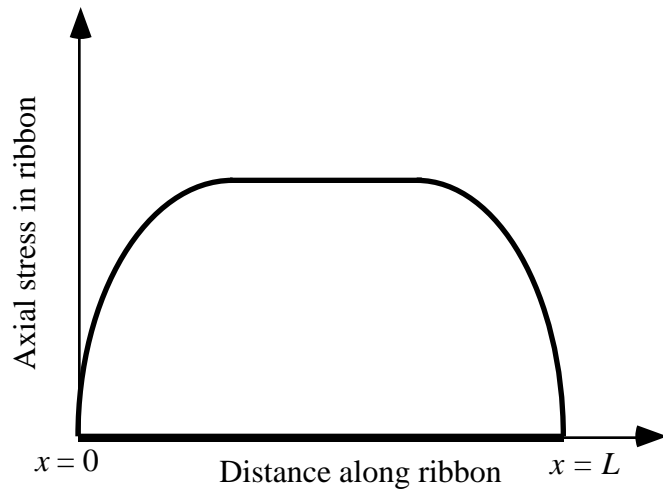


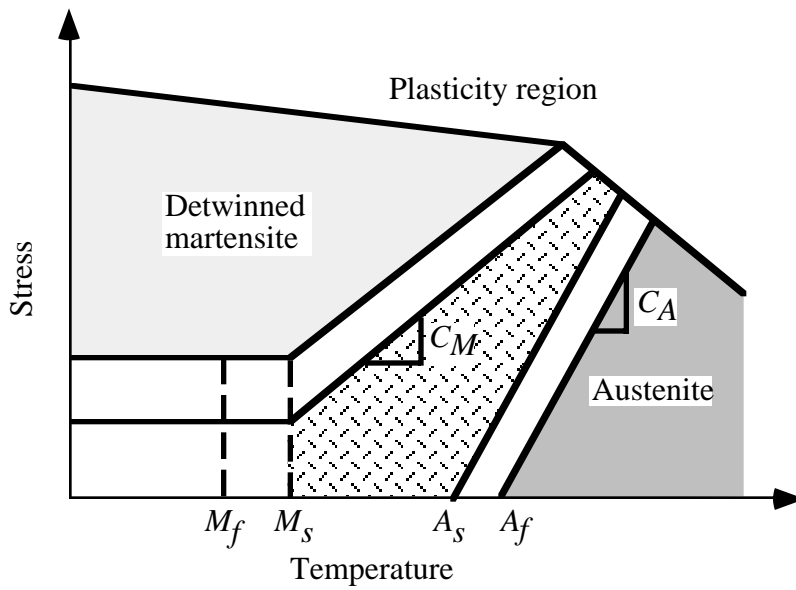
Figure 5.12. Displacement profiles of 1% prestrained SMA ribbon with a current input of 1.50 A at steady state temperature and after cooldown.

composite, Bidaux et al. (1993) speculated that only the ends of an embedded SMA wire might be actuating. The present work confirms that the transformation zone is near the ends of the embedded ribbons. The residual deformation in Figure 5.11 (c) is restricted to the portion of the ribbon between the edge of the sample and the outermost fringe, at a distance of 4.1 mm from the edge. The transformation is restricted to the ends of the ribbon due to stress induced in the ribbon by the constraint of the matrix. The dominant stress in the SMA ribbon upon actuation is the axial stress. Figure 5.13 (a) shows a schematic of the axial stress profile in the ribbon, and the effect of applied stress on transformation temperatures is shown in Figure 5.13 (b). At a given temperature, the axial stress increases from zero at the edge of the sample to a steady value near the center. Near the edge of the sample, the stress in the ribbon is lower, and so the upward shift in transformation temperatures is smaller. Therefore, most of the transformation occurs near the edge of the sample.

Since the region of permanent deformation is bounded by the outermost fringe in Figure 5.11 (c), it is reasonable to assume that this fringe represents the location of a transformation front. On one side of the front, the ribbon is at least partially transformed, while transformation is yet to be initiated on the other side. Image analysis showed that the distance of the saddle point from the edge of the sample in Figures 5.11 (b) is 4.1 mm, which is exactly equal to the distance of the outermost fringe in Figure 5.11 (c). The saddle point, therefore, could represent the location of the transformation front at elevated temperature. In order to establish further that the saddle point and the outermost fringe represent the location of transformed SMA, the sample was heated to different temperatures by varying the power input. Increasing the temperature should induce greater transformation of the SMA, causing the actuation front to advance towards the center of the sample and/or further transformation of the partially transformed region near the edge. The sample was heated with additional current inputs of 1.55 A and 1.65 A.



(a)

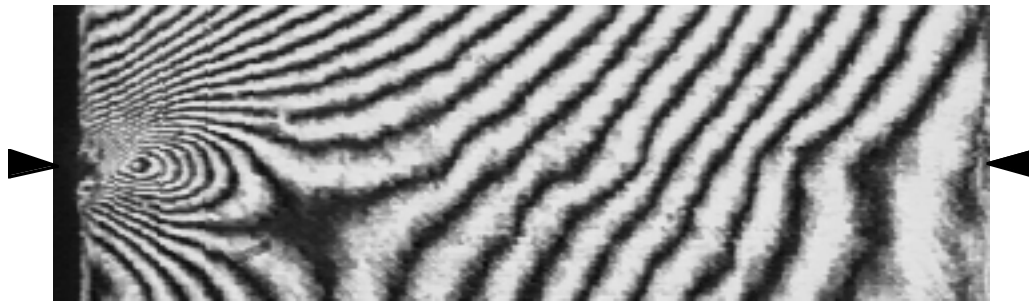


(b)

Figure 5.13. (a) Axial stress in embedded SMA ribbon on heating; (b) Effect of applied stress on transformation temperatures of SMA ribbons.

The moiré fringe patterns at steady state temperature for three different power inputs are shown in Figure 5.14. The corresponding displacement profiles are plotted in Figure 5.15. For a current input of 1.55 A, the saddle point is at a distance of 4.5 mm from the edge of the sample, as compared with 4.1 mm for a 1.50 A input. At 1.65 A, the saddle point is at 4.8 mm from the edge of the sample. An increasing number of fringes also develop between the saddle point and the edge of the sample with increasing power input. This rise in fringe density corresponds to larger inward displacement of the ribbon in this region, implying increased actuation. Therefore, for the power input levels considered, increasing the power resulted mostly in a greater transformation of the partially transformed region near the edge of the sample, with only a small movement in the transformation front. A rise in input current from 1.50 A to 1.65 A caused the actuation front to move from 4.1 mm to 4.8 mm. Higher power levels could not be applied since the resulting temperatures were above the glass transition temperature of the matrix and the grating, which start to relax. In fact, some loss of resolution due to matrix relaxation can be observed near the edge of the sample in Figure 5.14 (c) for a current input of 1.65 A.

The moiré fringe patterns after cooldown for different power inputs are shown in Figure 5.16 and the displacement profiles are plotted in Figure 5.17. The outermost fringe is located at a distance of 4.5 mm from the edge for a current input of 1.55 A, and at 4.8 mm for an input of 1.65 A. Even at higher inputs, the location of the outermost fringe after cooldown matches the location of the saddle point at steady state temperature. It is therefore reasonable to assume that the saddle point represents the location of the actuation front while the ribbon is being heated. The density of the fringes near the edge of the sample in Figure 5.17 also increases with increasing power, confirming that the partially transformed region undergoes further transformation.



(a)



(b)



(c)

Figure 5.14. Moiré images of 1% prestrained ribbon sample at steady state temperature for different current inputs: (a) $I = 1.50$ A; (b) $I = 1.55$ A; and (c) $I = 1.65$ A.

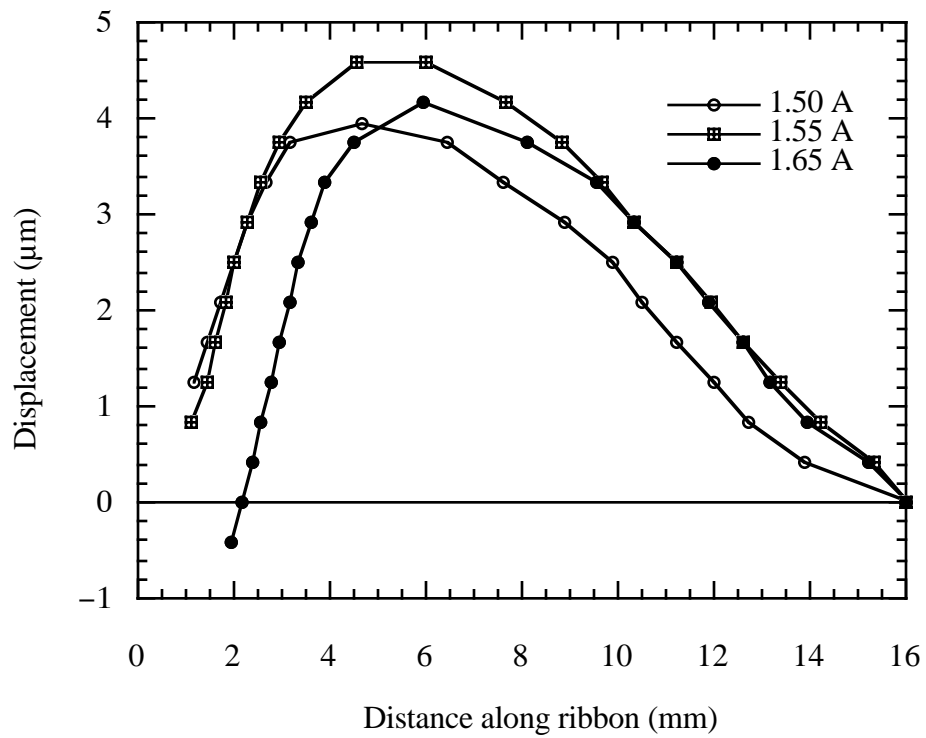
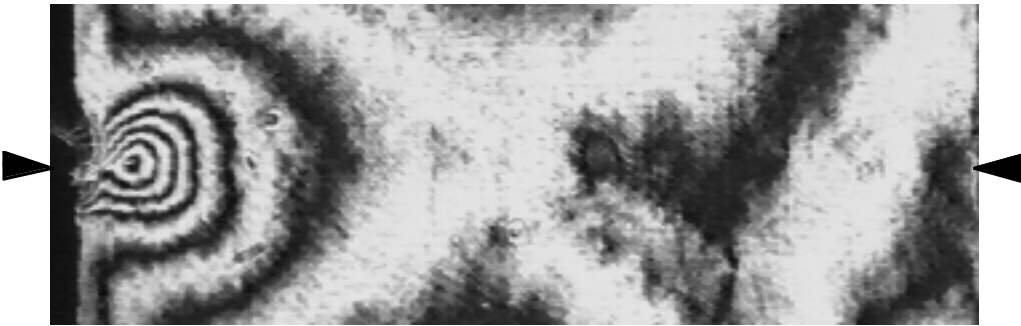


Figure 5.15. Displacement profiles of 1% prestrained SMA ribbons at steady state temperature for different current inputs.



(a)



(b)



(c)

Figure 5.16. Moiré images of 1% prestrained ribbon sample after cooldown for different current inputs: (a) $I = 1.50$ A; (b) $I = 1.55$ A; and (c) $I = 1.65$ A.

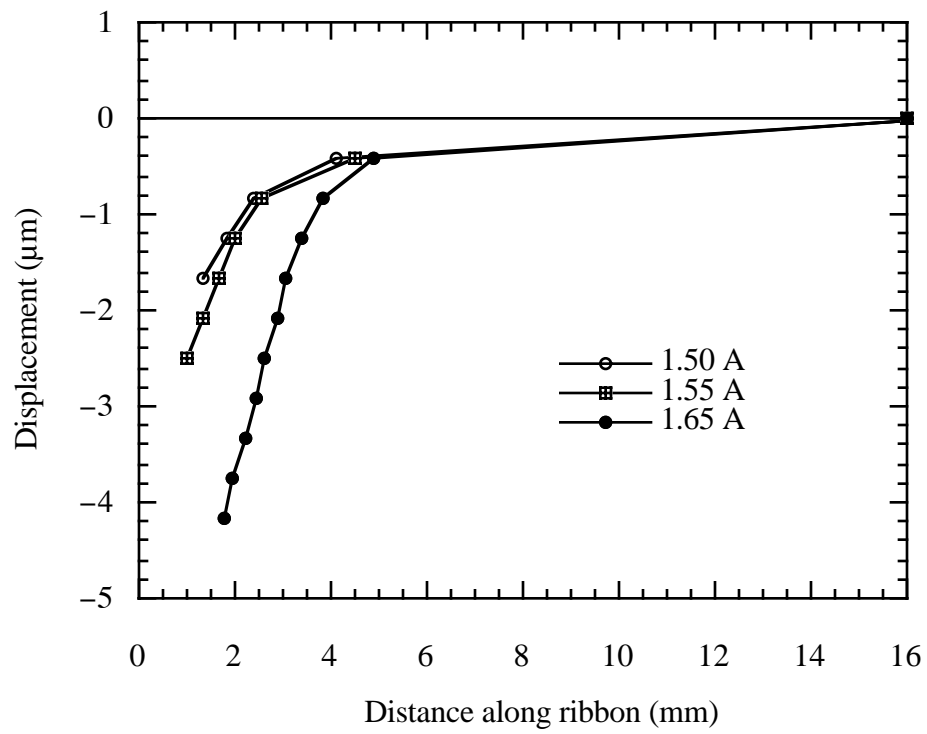


Figure 5.17. Displacement profiles of 1% prestrained SMA ribbons after cooldown for different current inputs.

Since the saddle point represents the location of a transformation front, the fringes to the left of the saddle point in Figure 5.11 (b) are due to the thermal expansion plus the shape memory effect, while those on the right are due to thermal expansion alone. Displacements in the annealed ribbon samples in Figure 5.9 (b) are due solely to thermal expansion. Therefore, at a given material point, the displacement due to shape memory effect alone can be obtained by subtracting the displacement of annealed ribbons from the displacement of prestrained ribbons, if the experimental conditions and samples are identical. On subtraction, the steady state SMA displacement at a point 2 mm from the edge was found to be $-5.3 \mu\text{m}$. Since the SMA ribbons used were one-way, the amount of transformation at steady state temperature should be retained upon cooldown. No displacement due to thermal expansion should exist after the sample has cooled to room temperature. After cooldown, all the observed fringes in Figure 5.11 (c) are due to shape memory effect alone. The measured displacement after cooldown at a distance of 2 mm from the edge was only $-1.15 \mu\text{m}$.

Lower values of SMA displacement after cooldown from steady state suggest that some of the martensite that had been transformed to austenite was transforming back to martensite upon cooling. A schematic of the behavior of the SMA ribbon composites upon heating and cooling is given in Figure 5.18. The sample is stress-free at room temperature. As it heats up, the ribbon expands, but the matrix expands more, causing the tension in the ribbon and compression in the matrix. As the shape memory effect occurs, the ribbon contracts and increases the tensile stress in the ribbon and the compressive stress in the matrix. After cooldown, the thermal effects dissipate but the length of the transformed ribbon is shorter than its original length, while the matrix is unaffected. Therefore, after cooldown from steady state temperature the ribbon is still in tension and the matrix in compression. At room temperature T , the ribbon is between the austenite start and the austenite finish temperatures. A schematic of a typical SMA stress-strain curve at a

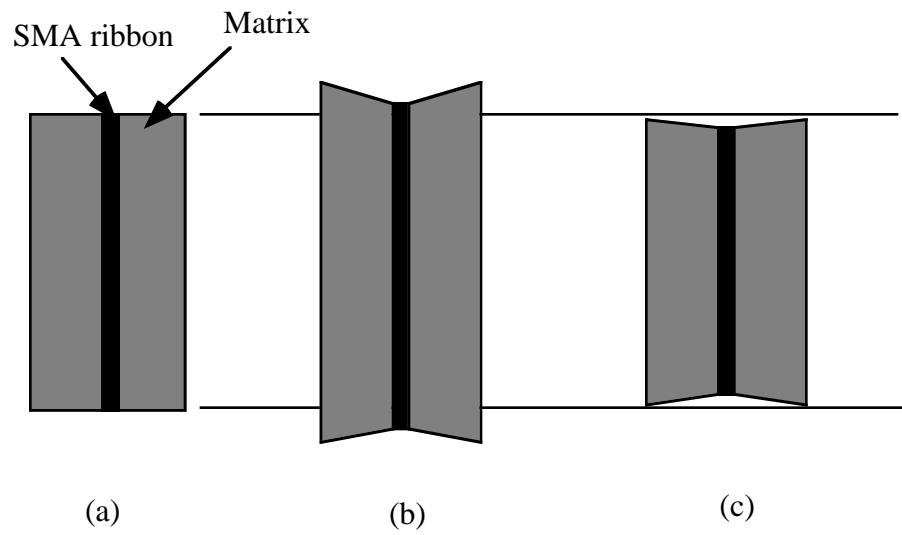


Figure 5.18. Schematic of displacements in prestrained SMA ribbon sample:
(a) Prior to heating; (b) At steady state temperature; and (c) After cooldown

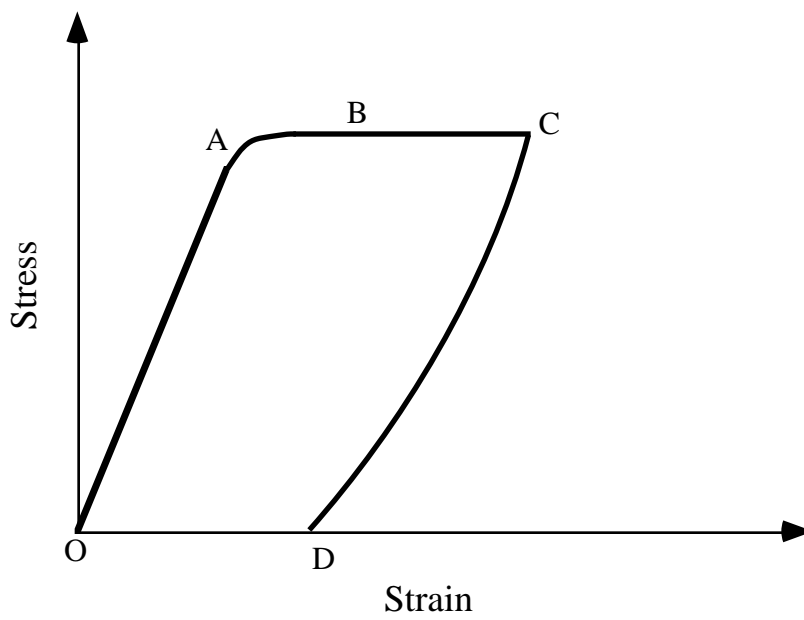


Figure 5.19. The stress–strain curve of a typical shape memory alloy at $M_s < T < A_s$.

temperature T such $M_s < T < A_s$ is shown in Figure 5.19. Point A on the curve represents the elastic limit. Stress-induced martensite is formed between point A and point C. On unloading, a permanent strain D–O remains and can be recovered by raising the temperature of the SMA above A_f . For the ribbon composite, the residual tensile stress upon cooldown (Figure 5.18) induces a strain that approximately follows the stress–strain curve in Figure 5.19. If the residual stress is sufficiently large, stress-induced martensite is formed (Point B). This transformation back to martensite due to residual stresses could account for lower SMA displacements in the ribbon upon cooldown when compared with steady state SMA displacements.

5.4.3. *Transient Displacements*

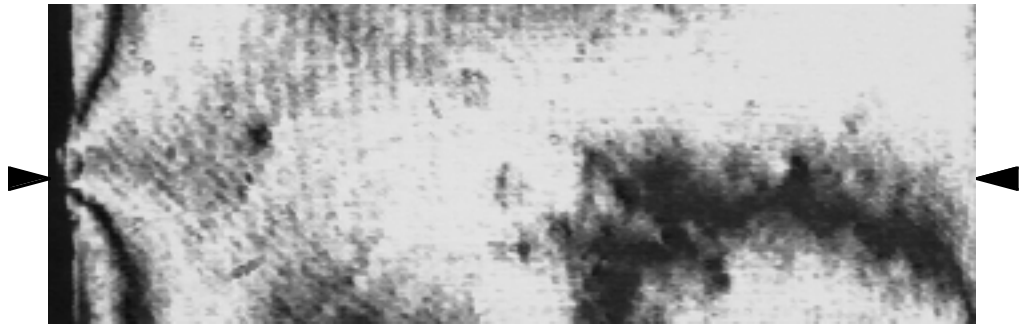
It was established from the steady state displacement data that the saddle point in the moiré fringe patterns represents the location of a phase transformation front. In this section, the location of the saddle point during heatup is monitored to obtain some insight into the evolution of the phase transformation front. In the first heating cycle, the ribbon was heated resistively with a constant current of 1.50 A for 240 s, at which time the power was turned off. After cooling an additional 240 s, the sample was reheated with a current input of 1.55 A without moving it from the original fixture. After another heating and cooling cycle of 480 s, the experiment was repeated with 1.65 A. The fringe patterns were continuously recorded using a VCR.

Moiré images of the 1% prestrained sample for the initial current input of 1.50 A are shown in Figure 5.20 at 15 s intervals. Four uniformly spaced fringes, indicating thermal expansion, are observed at $t = 15$ s. The formation of a saddle point begins at $t = 30$ s near the edge of the sample and is clearly visible at $t = 45$ s. The saddle point moves slowly towards the center of the sample. The fringes to the right of the saddle point are formed due to thermal expansion alone, and remain largely unchanged after $t = 120$ s. The

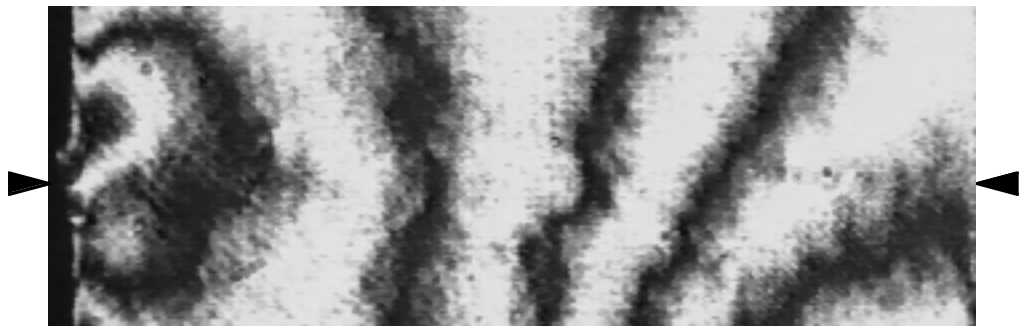
fringes to the left of the saddle point, which are formed due to shape memory actuation, continue to evolve. At $t = 240$ s, seven fringes are induced by actuation, including the fringe forming the saddle point.

Movement in the saddle point indicates a movement of the actuation front, while increasing fringe density shows that further transformation is taking place in the partially transformed region to the left of the saddle point. For the power inputs used, it is seen from Figure 5.8 that a steady state temperature is attained in about 200 s. For these power levels, significant thermal expansion is observed before the shape memory effect occurs. The delayed SMA actuation is partly because the power inputs were kept low and actuation does not start until the austenite start temperature of 35°C . Another reason for slow actuation is the build up of stress in the ribbon, which raises the phase transformation temperatures.

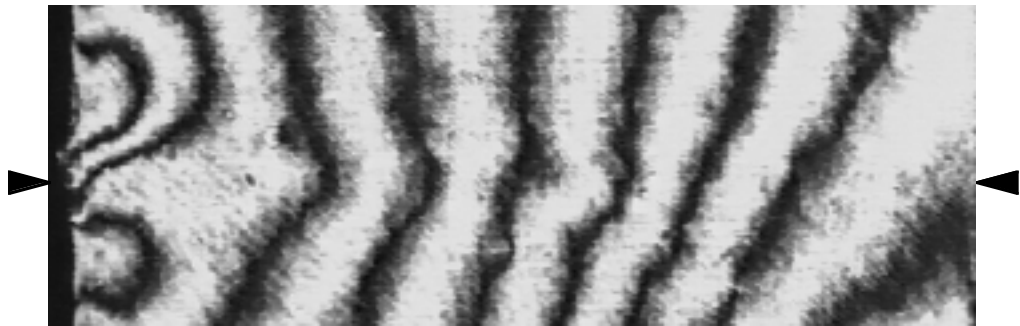
The distance of the saddle point from the edge of the sample with time is plotted in Figure 5.21 and the velocity of the transformation front is estimated from the slope of the displacement curve. The velocity V_1 in the initial part of the curve was $25\ \mu\text{m/s}$ and velocity V_2 at steady state temperature was $2.4\ \mu\text{m/s}$. For larger levels of power input, higher temperatures are attained more quickly, inducing faster SMA transformation. A rise in the rate of transformation increases the velocity of the actuation front and therefore, higher power inputs result in higher front velocities. However, as the SMA actuates, larger stresses are induced in the ribbon by the surrounding matrix, which raises the transformation temperatures. The upward shift in transformation temperatures makes the martensite-to-austenite transformation more difficult, causing a decrease in the velocity of the actuation front. The stress induced by the matrix in the ribbon is governed by the properties of both the SMA and the epoxy matrix. Therefore, the actuation front



(a)

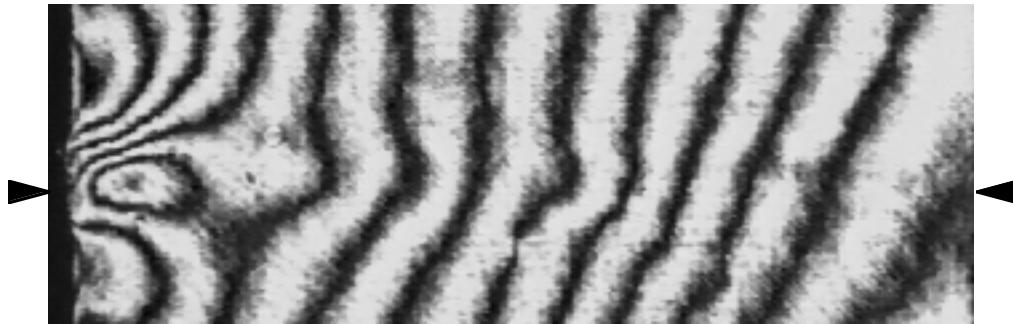


(b)

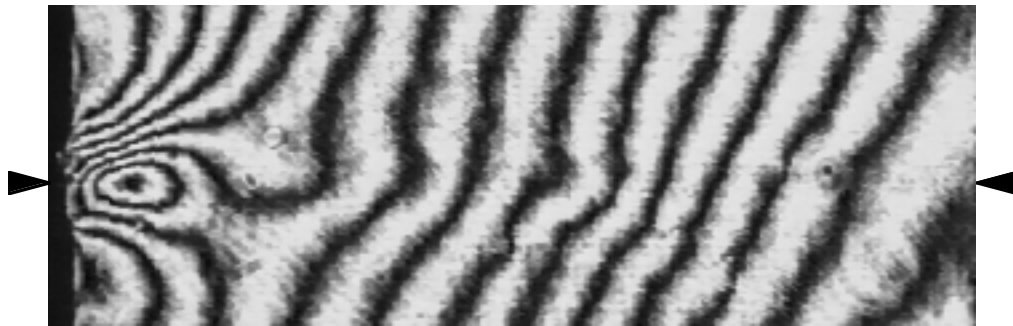


(c)

Figure 5.20. Transient moiré images of 1% prestrained ribbon sample with a current input of 1.50 A: (a) $t = 0$; (b) $t = 15$ s; (c) $t = 30$ s.



(d)

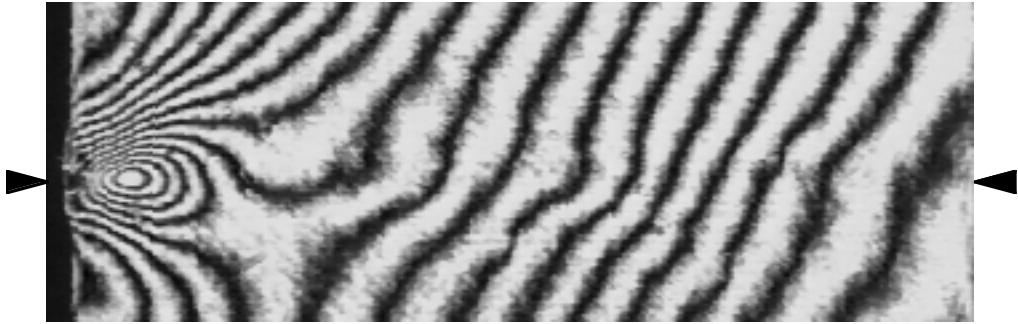


(e)

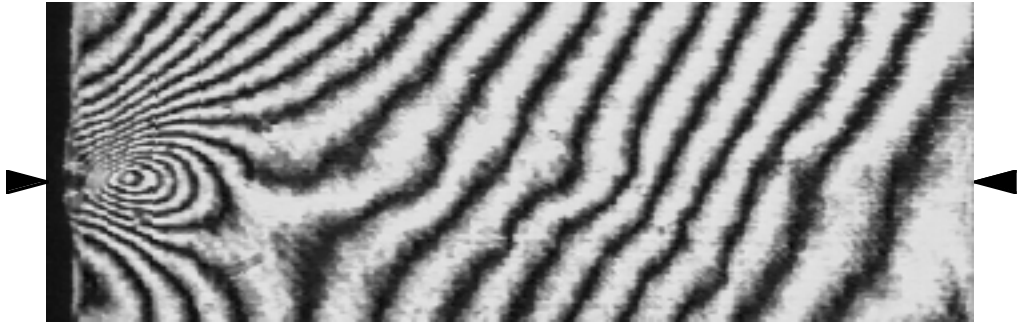


(f)

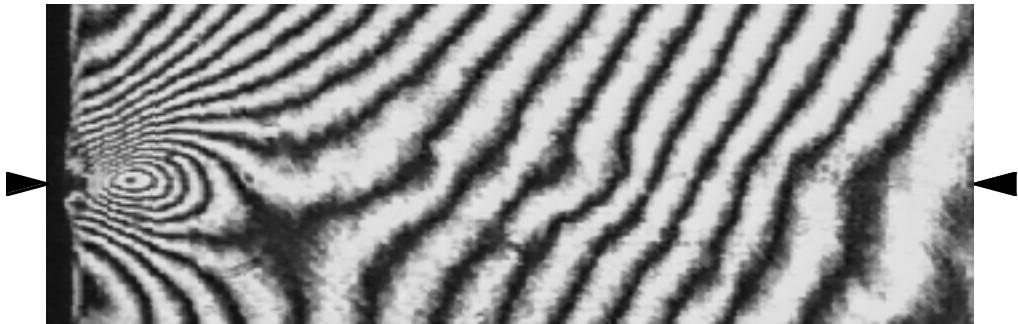
Figure 5.20. Transient moiré images of 1% prestrained ribbon sample with a current input of 1.50 A: (d) $t = 45$ s; (e) $t = 60$ s; (f) $t = 75$ s.



(g)

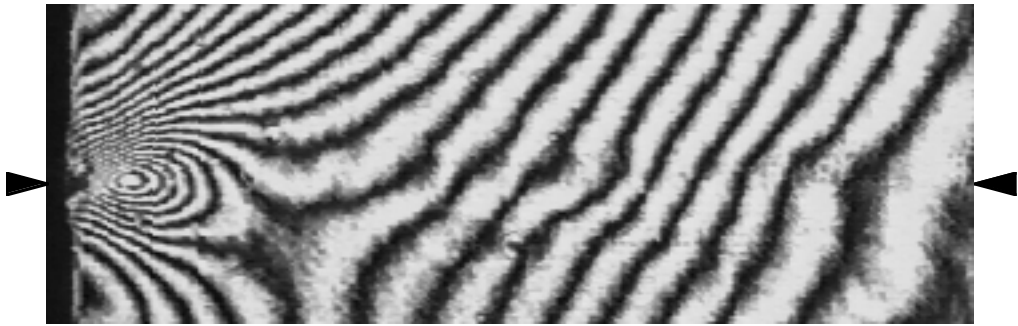


(h)

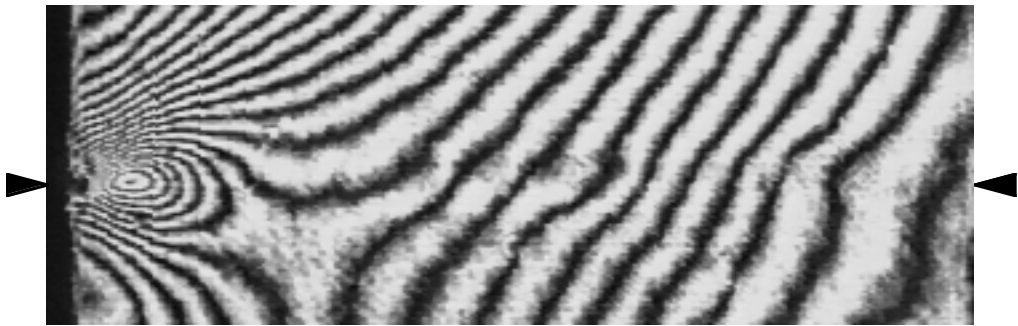


(i)

Figure 5.20. Transient moiré images of 1% prestrained ribbon sample with a current input of 1.50 A: (g) $t = 90$ s; (h) $t = 105$ s; (i) $t = 120$ s.



(j)

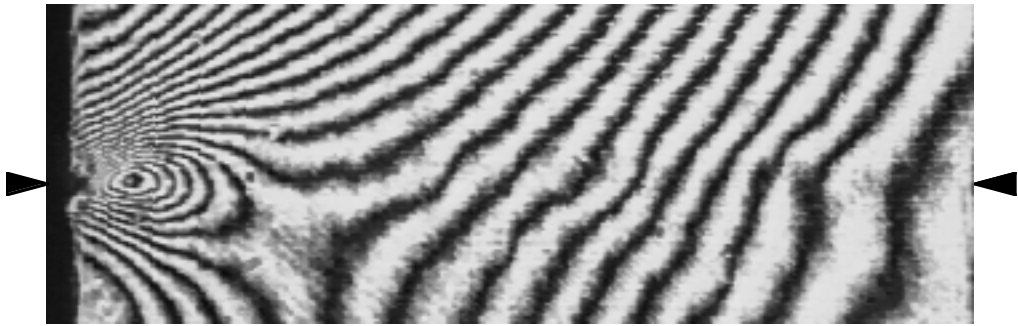


(k)

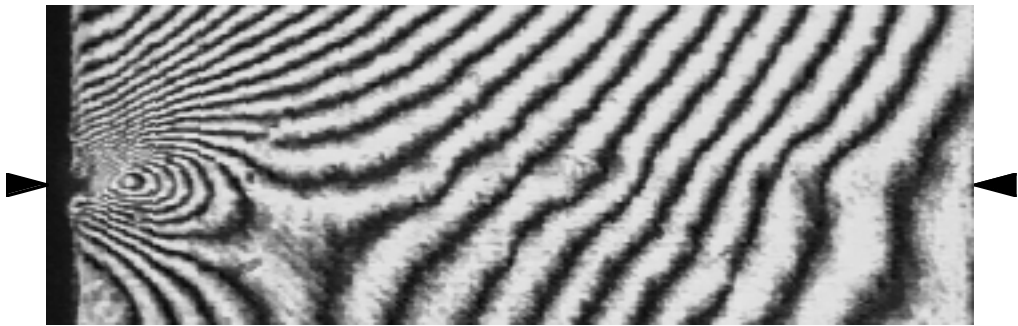


(l)

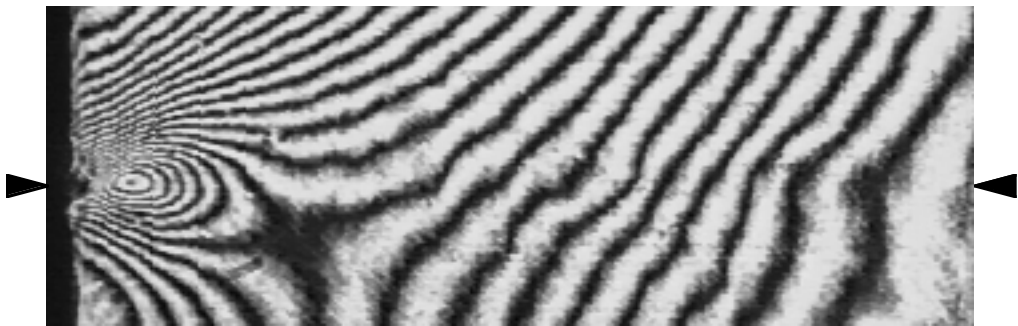
Figure 5.20. Transient moiré images of 1% prestrained ribbon sample with a current input of 1.50 A: (j) $t = 135$ s; (k) $t = 150$ s; (l) $t = 165$ s.



(m)

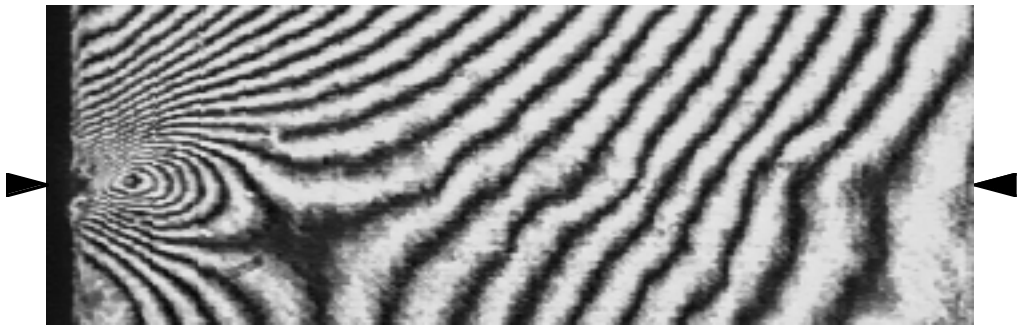


(n)

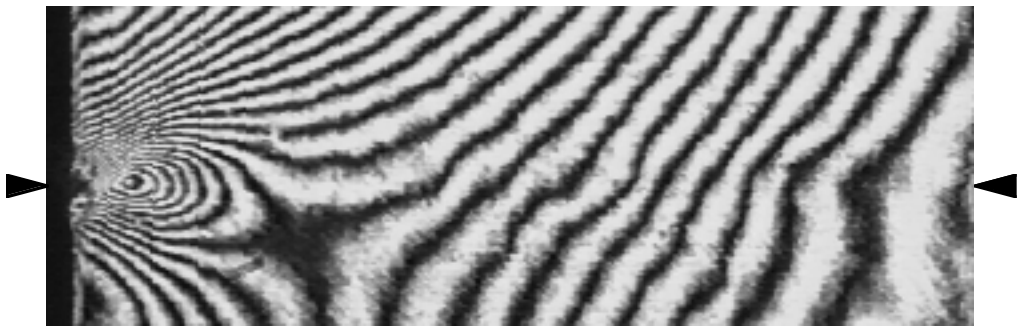


(o)

Figure 5.20. Transient moiré images of 1% prestrained ribbon sample with a current input of 1.50 A: (m) $t = 180$ s; (n) $t = 195$ s; (o) $t = 210$ s.



(p)



(q)

Figure 5.20. Transient moiré images of 1% prestrained ribbon sample with a current input of 1.50 A: (p) $t = 225$ s; (q) $t = 240$ s.

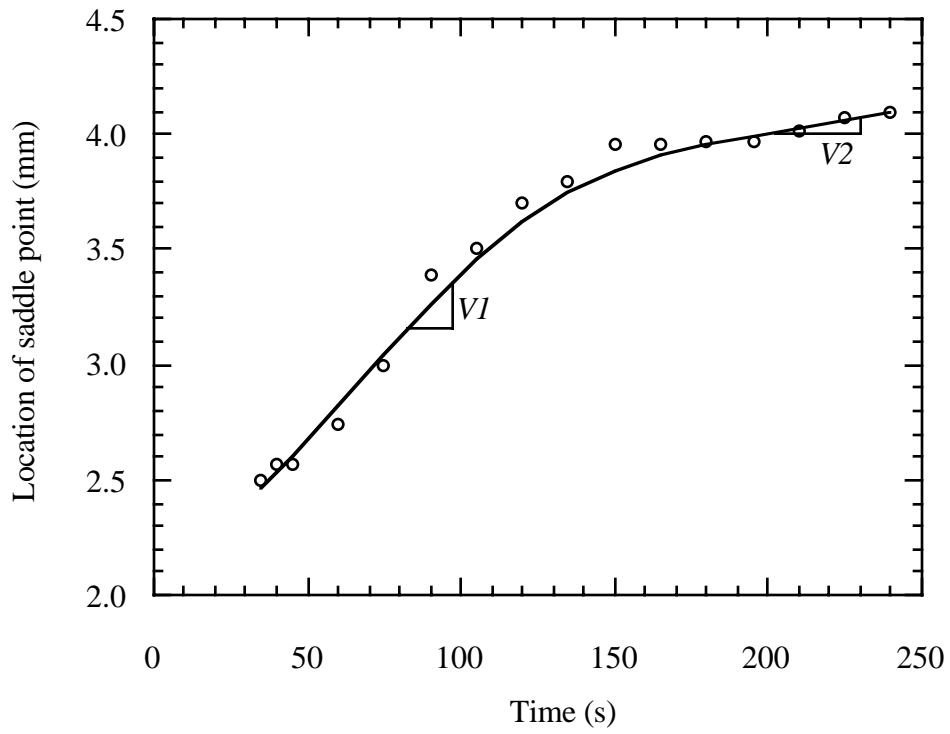
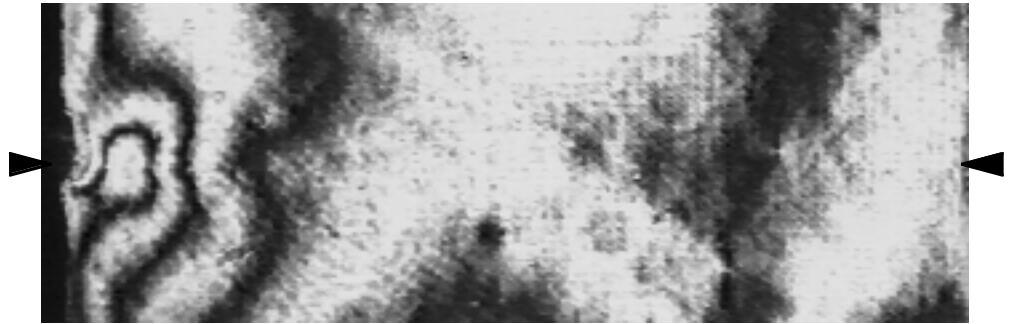


Figure 5.21. Change in location of the saddle point with time for SMA ribbon sample with a current input 1.50 A.

velocity is highly dependent on the loading conditions, sample geometry, and the material properties of the SMA and the matrix.

When the SMA ribbon sample was reheated with a current input of 1.55 A, an interesting transient behavior was observed. Figure 5.22 shows the moiré fringe patterns of the reheated sample at time $t = 0$, $t = 10$ s and $t = 60$ s. Since the same sample was used for obtaining the 1.50 A input data, residual fringes are observed at time $t = 0$. Soon after the power is turned on, the number of fringes increases rapidly from 3 to 8. By $t = 60$ s, a clear saddle point is observed. The fringe development after $t = 60$ s is very similar to the transient behavior in Figure 5.20. The saddle point moves about 0.4 mm towards the center of the sample at $t = 240$ s. Similar behavior was observed when the sample was reheated with a current input of 1.65 A. The initial rapid development of fringes for the reheated sample cannot be easily explained and needs to be investigated further.

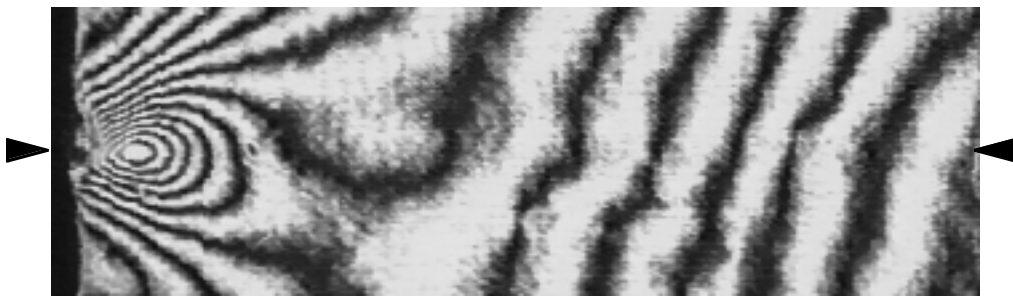
At the start of the heat-cool cycle with a power input of 1.55 A, the ribbon is in tension and the matrix in compression due to permanent strain induced by the first cycle with 1.50 A. The SMA ribbon is either in the region O–A or the region A–C on the stress-strain curve shown in Figure 5.19. When the power is switched on, the ribbon temperature rises first, providing stress relief due to thermal expansion. If, for example, the SMA is at point B on the stress-strain curve, this stress relief causes a recovery of the elastic part of the curve denoted by O–A. If the elastic part is large enough, a rapid buildup of fringes would be observed. As the matrix is heated by conduction, tensile stresses again build up in the ribbon, causing some of the fringes to dissipate. The elastic strain recovery is one possible explanation for the fringe buildup. However, other factors such as the change in the matrix properties because of heating to a temperature close to the T_g need to be considered.



(a)



(b)



(c)

Figure 5.22. Transient moiré images of 1% prestrained ribbon sample reheated with a current input of 1.55 A: (a) $t = 0$; (b) $t = 10$ s; and (c) $t = 60$ s.

5.5 Conclusions

Moiré interferometry was utilized to obtain the in-plane displacements of SMA ribbons embedded in a polymer matrix. Displacements of annealed ribbon samples compared well to a steady state finite element solution. Heating of 1% prestrained SMA ribbons showed that most of the phase transformation was restricted to a region close to the edge of the sample. Residual fringes were observed in the sample after cooldown, indicating one-way transformation. The outermost residual fringe indicated the location of the a phase transformation front upon cooldown. The location of the saddle point at steady state temperature matched the location of the outermost fringe in the sample after cooldown, indicating that the saddle point might represent the location of a phase transformation front during heatup.

Increasing the power input to the sample resulted in only a small movement of the transformation front but induced further transformation in the partially transformed region between the edge of the sample and the actuation front. Comparison of SMA displacements at steady state with residual SMA displacements after cooldown indicated that some of the martensite transformed to austenite during heatup might be transforming back to martensite upon cooling due to the tensile stress applied by the matrix on the ribbon.

Transient measurements showed that displacements due to thermal expansion occur at a faster rate than SMA displacements, for the configuration and power input levels considered. The saddle point was used to track the evolution of the phase transformation front with time. For a current input of 1.50 A, the transformation front had an initial velocity of 25 $\mu\text{m/s}$ which tapered off to 2.4 $\mu\text{m/s}$ as equilibrium was reached.

6. COMPARISON WITH THEORY

Since the discovery of shape memory alloys, most applications have been restricted to the use of SMAs directly, without embedding them in a host material. Only in recent years has attention been directed towards the study of the SMA composite. There is a paucity of both experimental data and theoretical models to provide guidelines for the design of an SMA composite. Chapters 2 through 5 discussed various experimental investigations of the behavior of an embedded SMA. In particular, photoelasticity and moiré interferometry were utilized to obtain quantitative data for evaluation of theoretical models.

Significant effort has been devoted to the development of constitutive models to describe the response of shape memory alloy materials. Most of these models provide only a one-dimensional description of the material behavior. More recently, several three-dimensional models have emerged. To the knowledge of the author, only Lagoudas and Qidwai (1997) have attempted to predict the behavior of SMAs in composites. In this chapter, the different types of models available in the literature are first discussed briefly. Then, the 1-D constitutive model of Liang and Rogers (1990) is modified and applied to the analysis of SMA ribbon composites. The constitutive model was incorporated into an iterative finite element solution to predict displacements and stresses which are compared with experimental data.

6.1 Overview of Constitutive Models

The different types of constitutive models for shape memory alloys can be classified into three broad groups. The first group of models is based on tracking the motion of the austenite–martensite interface in a 1-D SMA body. The interface is treated as a strain discontinuity and the internal structure of the interface is not examined. Abeyaratne and

Knowles (1991) assumed a kinetic relation to determine the speed of the interface as a function of stress and a uniform temperature. Falk (1980) constructed a smooth polynomial function to describe the movement of the interface. Pego (1987) used a one-dimensional nonlinear viscoelasticity model to predict phase transitions. Leo, Shield and Bruno (1993) determined the position of the interface by assuming the overall behavior of the wire to be quasi-static, precluding the need for an additional kinetic relation to determine the motion of the interface.

The second group consists mainly of 1-D macromodels that are based on uniaxial constitutive laws. The fraction of martensite phase in the SMA is used as an internal variable and a semi-empirical quasi-static kinetic law is employed to describe the phase transition curves. Many of the more recent models in this group were based on pioneering work by Tanaka (1986) who derived the stress–strain relations from continuum mechanics and thermodynamics. An exponential function was used to describe the kinetic law governing the phase transformation. The martensite fraction in the material was treated as an internal variable that was a function of stress and temperature. Liang and Rogers (1990) adopted Tanaka’s formulation but used a cosine function instead of an exponential to describe the phase transformation. Brinson (1993) modified Liang and Rogers’ (1990) model by separating the martensite volume fraction into two parts—one obtained by applied stress and the other induced by change in temperature. Ivshin and Pence (1994) used the austenite fraction as an internal variable and used hyperbolic relations to express the evolution of the phase transformation front. In this class of models, only Liang and Rogers (1993) have modified their formulation to address the 3-D response.

The third group of models are self-consistent type models based on some type of phase-mixture theory formulated in terms of free energy. Three-dimensional models have been derived using energy dissipation concepts analogous to plasticity theory. Berveiller,

Patoor and Buisson (1991) and Patoor, Eberhardt and Berveiller (1993) modeled the single crystal free energy and transformation rate by treating the volume fraction of martensite variants as an internal variable. Polycrystalline transformation response was then predicted from the single crystal equations using self-consistent micromechanics. Sun and Hwang (1993a, 1993b) derived a thermodynamical model for both pseudoelasticity and shape memory effect due to transformation and reorientation. Boyd and Lagoudas (1995a) extended the work of Sun and Hwang (1993) to include adiabatic deformation and isotropic and kinematic hardening. In a later work, Boyd and Lagoudas (1995b) also incorporated the effects of two-way shape memory effect. Müller (1989) proposed a model combining free energy concepts with statistical mechanics. In recent work, Qidwai and Lagoudas (1997) adapted the model of Boyd and Lagoudas (1995b) to predict the behavior of SMA ribbons in polymer composites.

6.2 One-Dimensional Constitutive Model

Many of the constitutive models discussed in the previous section adequately predict the response of unembedded SMA materials. The 1-D model of Liang and Rogers (1990) is derived from fundamental thermodynamics but is also relatively straightforward to implement. Epps and Chopra (1997) demonstrated that the model makes excellent predictions of the 1-D pseudoelastic and shape memory behavior. In this section, the general formulation of the model by Liang and Rogers (1990) is described briefly. The model is then modified by making further assumptions that are applicable to the room temperature cured ribbon composite problem in Chapters 4 and 5.

6.2.1 General Formulation

The one-dimensional formulation described in this section is based on original work by Tanaka (1986) which was later modified by Liang and Rogers (1990). For a one-dimensional SMA material undergoing transformation, Tanaka (1986) derived from the

principles of thermodynamics the following relationship between the second Piola-Kirchhoff stress σ and the Helmholtz free energy Φ :

$$\sigma = \rho_o \frac{\partial \Phi(\varepsilon, \xi, T)}{\partial \varepsilon} = \sigma(\varepsilon, \xi, T) \quad (6.1)$$

where ρ_o is the density in the Lagrangian configuration, ε is the Green strain, ξ is the martensite volume fraction, and T is the temperature. Equation (6.1) is based on the assumption that the thermomechanical behavior of an SMA material can be fully described in terms of the three variables ε , ξ and T . The martensite volume fraction ξ varies from 0 to 1 with $\xi = 1$ representing 100% martensite. By using differential calculus, Equation (6.1) is written in the rate form

$$d\sigma = E(\varepsilon, \xi, T)d\varepsilon + \Omega(\varepsilon, \xi, T)d\xi + \Theta(\varepsilon, \xi, T)dT \quad (6.2)$$

where the material coefficients E , Ω and Θ denote the Young's modulus, transformation tensor and thermal expansion, respectively. Tanaka (1986) assumed all three of the material coefficients to be constants, leading to the constitutive relation

$$\sigma - \sigma_o = E(\varepsilon - \varepsilon_o) + \Omega(\xi - \xi_o) + \Theta(T - T_o). \quad (6.3)$$

The maximum possible recoverable strain in an SMA is a material constant and is denoted by ε_L . By substituting the initial conditions $\sigma_o = \varepsilon_o = \xi_o = 0$ and final conditions $\sigma = 0$, $\varepsilon = \varepsilon_L$, $\xi = 1$ with $T = T_o$ into Equation (6.3), the transformation tensor Ω is expressed in terms of the modulus E as

$$\Omega = -\varepsilon_L E. \quad (6.4)$$

Experimental studies (Melton, 1989) have shown that the modulus E of the SMA is strongly dependent on the martensite volume fraction. To describe the change in modulus, Liang (1990) adopted a linear relation between E and ξ , given by

$$E(\varepsilon, \xi, T) = E(\xi) = E_a + \xi(E_m - E_a) \quad (6.5)$$

where E_m is the SMA modulus at 100% martensite and E_a is the SMA modulus at 100% austenite. Since E is assumed to be a function of ξ alone, Ω is also assumed to be a function of the martensite fraction only. Expanding $\Omega(\xi)$ in a Taylor series about ξ_o and neglecting higher order terms gives

$$\Omega(\xi) = \Omega(\xi_o) + (\xi - \xi_o)\Omega'(\xi_o). \quad (6.6)$$

For $\xi = \xi_o$, the transformation tensor and the modulus are constants. Hence, Equation (6.4) can be utilized to obtain

$$\Omega(\xi_o) = -\varepsilon_L E(\xi_o). \quad (6.7)$$

Substituting Equations (6.7) and (6.5) into Equation (6.6) and simplifying leads to the general relation

$$\Omega(\xi) = -\varepsilon_L E(\xi). \quad (6.8)$$

Liang and Rogers (1990) and Brinson (1993) addressed only the unembedded SMA problem, where the SMA recovery strain were considerably larger than the strain due to thermal expansion. Therefore they assumed the thermal expansion tensor Θ to be a constant. For embedded SMAs, experiments discussed in Chapter 5 demonstrated that the

thermal expansion and SMA induced displacements are comparable in magnitude. In the current analysis Θ is not assumed to be a constant, $\Theta = \Theta(\xi)$. By analogy to the thermal expansion tensor in 1-D thermoelasticity, the tensor Θ is assumed to have the form

$$\Theta(\xi) = E(\xi)\alpha \quad (6.9)$$

where α is the coefficient of thermal expansion, which is assumed to be constant ($\alpha_A = \alpha_M = \alpha$). Equations (6.5), (6.8) and (6.9) are substituted into the rate equation (6.2), which is then integrated. After integration and simplification, the constitutive relations for non-constant material constants are obtained as

$$\sigma - \sigma_o = E(\xi)\varepsilon - E(\xi_o)\varepsilon_o + \Omega(\xi)\xi - \Omega(\xi)\xi_o + \Theta(\xi)T - \Theta(\xi_o)T_o. \quad (6.10)$$

Tanaka (1986) assumed an exponential kinetic law to express the dependence of the martensite volume fraction on stress and temperature. Liang and Rogers (1990) assumed a cosine relationship to model the stress–temperature–martensite interaction. The Liang and Rogers (1990) relations are adopted in the current model since it compares well with experimental data (Epps and Chopra, 1997) for unembedded shape memory alloys. The transformation from austenite to martensite is given by

$$\xi(\sigma, T) = \frac{1 - \xi_o}{2} \left\{ \cos \left[a_M \left(T - M_f - \frac{\sigma}{C_M} \right) \right] \right\} + \frac{1 + \xi_o}{2} \quad (6.11)$$

$$\text{for } C_M(T - M_s) < \sigma < C_M(T - M_f)$$

and the transformation from martensite to austenite is governed by

$$\xi(\sigma, T) = \frac{\xi_o}{2} \left\{ \cos \left[a_A \left(T - A_s - \frac{\sigma}{C_A} \right) \right] + 1 \right\} \quad (6.12)$$

for $C_A(T - A_f) < \sigma < C_A(T - A_s)$.

Here, C_A and C_M denote the stress–temperature coefficients for austenite and martensite, respectively, and the constants a_M and a_A are given by

$$a_M = \frac{\pi}{M_s - M_f}, \quad a_A = \frac{\pi}{A_f - A_s}. \quad (6.13)$$

6.2.2 Adaptation for Embedded SMA

By using Equations (6.8) and (6.9), Equation (6.10) can be rewritten as

$$\sigma - \sigma_o = E(\xi)(\varepsilon - \varepsilon_L \xi + \alpha T) + E(\xi_o)(\varepsilon_o - \varepsilon_L \xi_o + \alpha T_o). \quad (6.14)$$

For the room temperature cured ribbon composites described in Chapters 4 and 5, the martensite in the ribbon was induced by applying a stress to a fully austenitic ribbon at room temperature. The initial strain ε_o induced in the ribbon prior to embedding is directly related to the initial martensite fraction ξ_o . At 100% martensite, $\xi = 1$ and $\varepsilon = \varepsilon_L$. Prior to application of initial strain, $\xi = \varepsilon = 0$. Therefore, it is assumed that the initial martensite fraction can be expressed in terms of initial strain as

$$\xi_o = \frac{\varepsilon_o}{\varepsilon_L}. \quad (6.15)$$

Since the experiments were started at room temperature, the initial temperature T_o is taken to be zero. There is no initial stress field in the matrix for room temperature cured samples and therefore σ_o is also zero. Substituting Equation (6.15) and the initial conditions $\sigma_o = T_o = 0$ into Equation (6.14) gives

$$\sigma = E(\xi)(\varepsilon - \varepsilon_L \xi + \alpha T). \quad (6.16)$$

Stress and displacement data in Chapters 4 and 5 were obtained by heating the ribbon, which transforms from martensite to austenite. Since one-way ribbons were used, only the forward transformations need to be considered. By combining Equation (6.12), which governs the forward transformation, with the relation between initial strain and martensite fraction given in Equation (6.15), the martensite fraction ξ is expressed as,

$$\xi(\sigma, T) = \frac{\varepsilon_o}{2\varepsilon_L} \left\{ \cos \left[a_A \left(T - A_s - \frac{\sigma}{C_A} \right) \right] + 1 \right\} \quad (6.17)$$

and therefore

$$\varepsilon_L \xi = \frac{\varepsilon_o}{2} \left\{ \cos \left[a_A \left(T - A_s - \frac{\sigma}{C_A} \right) \right] + 1 \right\} \quad (6.18)$$

The term denoting the thermal expansion effect on the right hand side of Equation (6.16) is $E\alpha T$. Similarly, the term denoting the shape memory effect is given by $-E\varepsilon_L \xi$. If the shape memory term can be expressed as a product of temperature and a coefficient accounting for the transformation, the thermal expansion and shape memory terms can be combined with a single coefficient that depends upon the martensite fraction. For the present analysis, it is assumed that the shape memory term can be expressed as

$$\varepsilon_L \xi = \gamma T \quad (6.19)$$

where

$$\gamma(\sigma, T) = \frac{\varepsilon_0}{2T} \left\{ \cos \left[a_A \left(T - A_s - \frac{\sigma}{C_A} \right) \right] + 1 \right\}. \quad (6.20)$$

By substituting Equation (6.20) into the Equation (6.16), the constitutive equation can be rewritten as

$$\sigma = E\varepsilon + E(\alpha - \gamma)T = E\varepsilon + E\alpha'T \quad (6.21)$$

where E is given by Equation (6.5) and $\alpha' = \alpha - \gamma$, so that,

$$E = E(\sigma, T) \quad \text{and} \quad \alpha' = \alpha'(\sigma, T). \quad (6.22)$$

6.3 Finite Element Analysis

6.3.1 Solution Procedure

A finite element model incorporating the constitutive relation described in Section 6.2 was constructed. The commercial finite element package ABAQUS (Hibbitt, Karlsson and Sorenson) was used to perform the analysis. The constitutive behavior of the SMA was determined by using equation (6.21). The matrix was assumed to be linear elastic. Both the SMA ribbon and the matrix were considered to be isotropic. The material properties shown in Tables 4.1 and 4.2 were used for the analysis. A perfect interface was assumed between the ribbon and the matrix.

The thermal problem was solved first in order to obtain a steady state temperature profile in the sample, which was then used as the input to calculate the stresses and displacements induced by heating. To simplify the numerical simulation, a one-quarter sample was constructed utilizing the geometric symmetries. A schematic of the sample

along with the assumed boundary conditions is shown schematically in Figure 6.1. The finite element mesh shown in Figure 6.2 was generated. Eight-node plane stress elements (DC2D8) having temperature as the only degree of freedom were used for the analysis. A heat generation capability was assigned to the ribbon. A range of values for resistivity for the SMA has been reported in the literature (Jackson, Wagner and Wasilewski, 1972). The resistivity was selected such that the computational steady state temperature in the sample was in agreement with the measured experimental values in Chapter 5. Room temperature was assumed to be 25°C. A typical temperature profile at a steady state temperature of 42.5°C ($\Delta T = 17.5^\circ\text{C}$) is shown in Figure 6.3.

The finite element mesh of the thermal problem was retained for solving the mechanical problem so that the temperatures at node points from the thermal problem could be assigned as nodal loads for the mechanical problem. Eight-node plane stress elements (CPS8) with two displacement degrees of freedom for each node were employed. Figure 6.4 schematically shows the boundary conditions used for the symmetric quarter-plate. Displacements are determined at nodal points, while stresses were calculated at the integration points to obtain stress contour plots.

The coefficient α' in the axial direction for the mechanical problem depended on the temperature and a field variable. The field variable was chosen to be the axial stress σ_{xx} in the ribbon. Therefore,

$$\alpha'_x = \alpha - \gamma \quad (6.23)$$

where α is constant and,

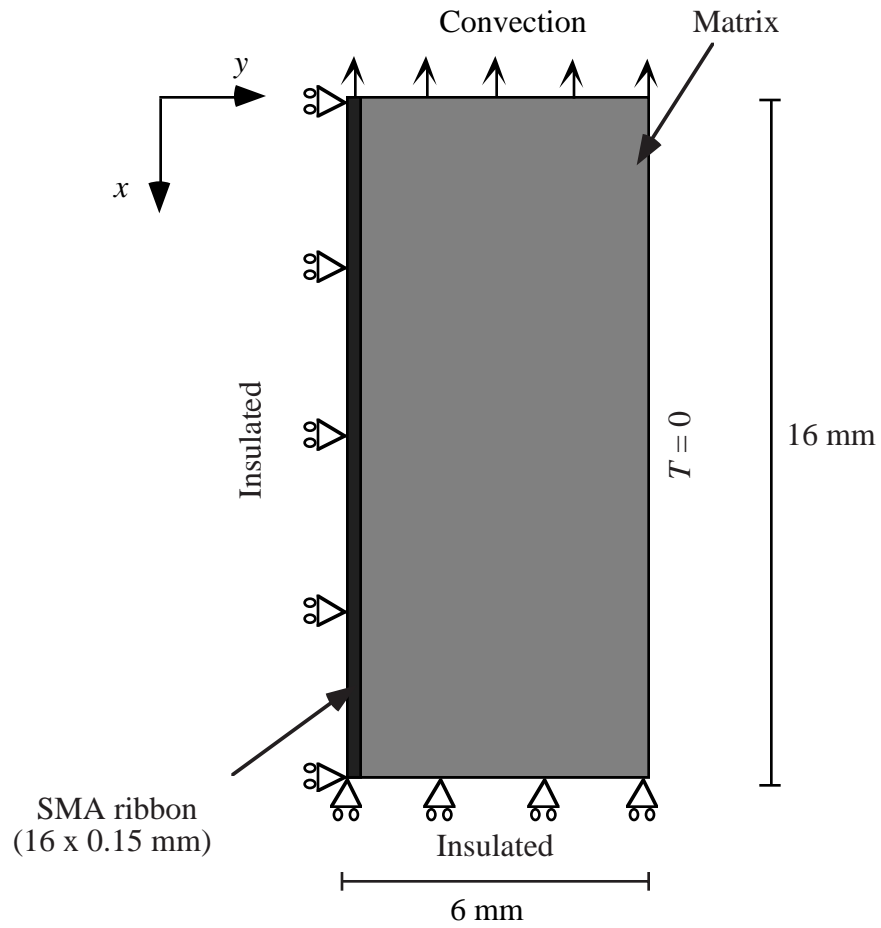


Figure 6.1. Schematic of sample geometry and boundary conditions for the thermal problem.

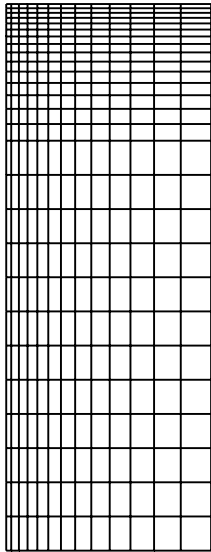


Figure 6.2. Finite element mesh for quarter-symmetric ribbon composite sample.

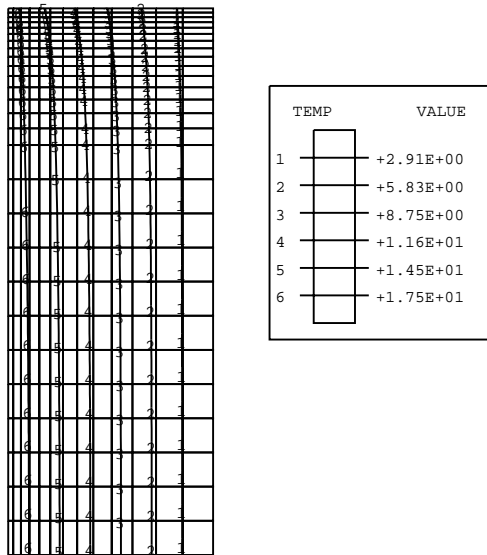


Figure 6.3. Contours of constant temperature difference at steady state.

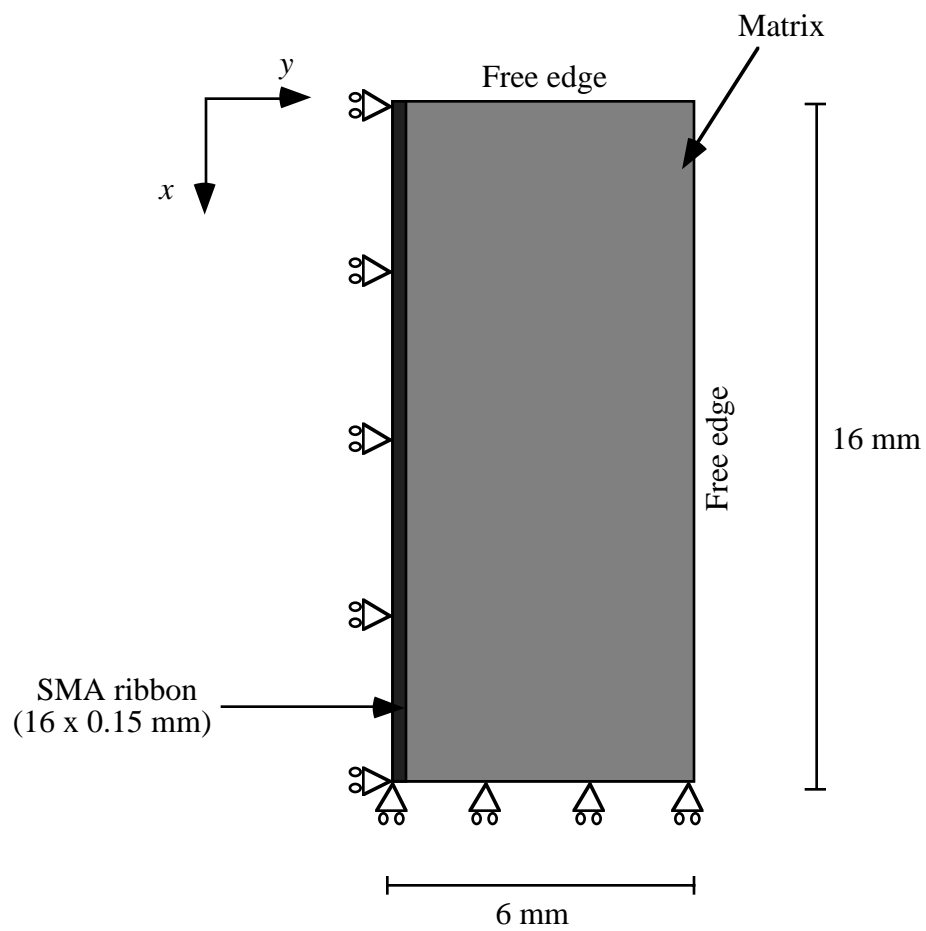


Figure 6.4. Schematic of sample geometry and boundary conditions for the mechanical problem.

$$\gamma = \gamma(\sigma_{xx}, T) \quad (6.24)$$

from Equation (6.20). In the direction perpendicular to the ribbon axis,

$$\alpha'_y = \alpha. \quad (6.25)$$

The steady state temperature solution was divided into linear increments with the actual temperature being reached at the final increment. After each increment, the ABAQUS user subroutine USDFLD was utilized to obtain the value of σ_{xx} at each integration point. Then, a new value of α' was calculated at each integration point, based on the axial stress and temperature of the previous increment. The modified α' was used to obtain the stresses and displacements for the present increment. Equation (6.20) was used to calculate γ , and then the effective CTE α' . After about 20 increments, the change in maximum stress was less than 1%. The reported results were calculated with 25 increments. Figure 6.5 shows a flowchart of the solution procedure.

6.3.2 Analysis and Discussion

The analysis was first carried out for a steady state temperature of 44°C in the ribbon. This temperature corresponds to a current input of 1.50 A in the displacement experiments discussed in Chapter 5. Displacements along the ribbon were obtained and compared with experimental data. Figure 6.6 shows the displacement profile obtained from the finite element (FE) solution along with the steady state displacement curve obtained using moiré interferometry. The two displacement profiles are found to exhibit some common features although the magnitudes of the displacements are quite different. Both curves show a local maximum with a positive slope near the edge of the sample and a negative slope near the center. The predicted local maxima are closer to the edge of the sample than the center, although the respective distances from the edge of the sample are not equal to the experimental values. A local debond approximately 1 mm in length

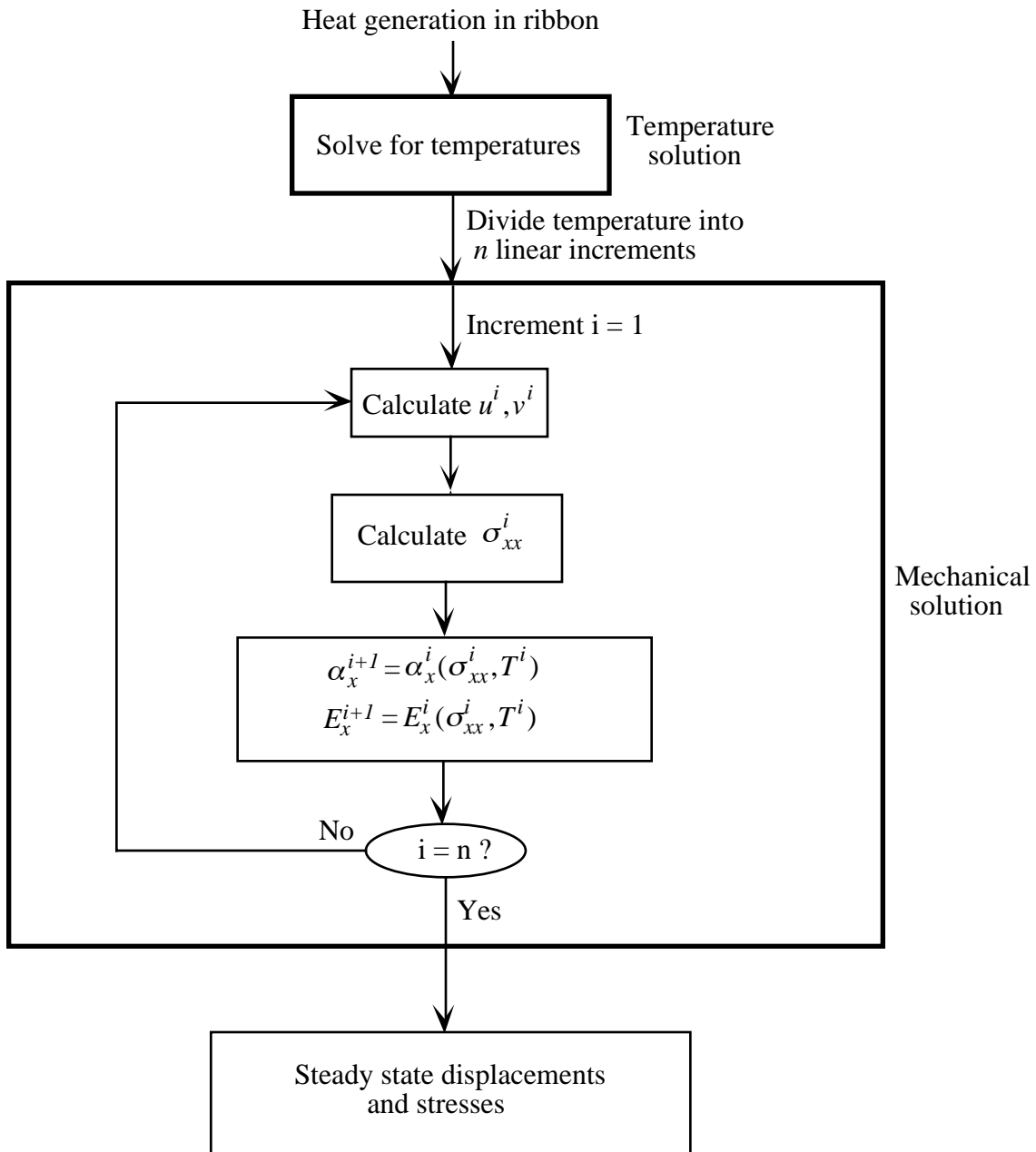


Figure 6.5. Schematic of finite element solution procedure for SMA ribbon composites.

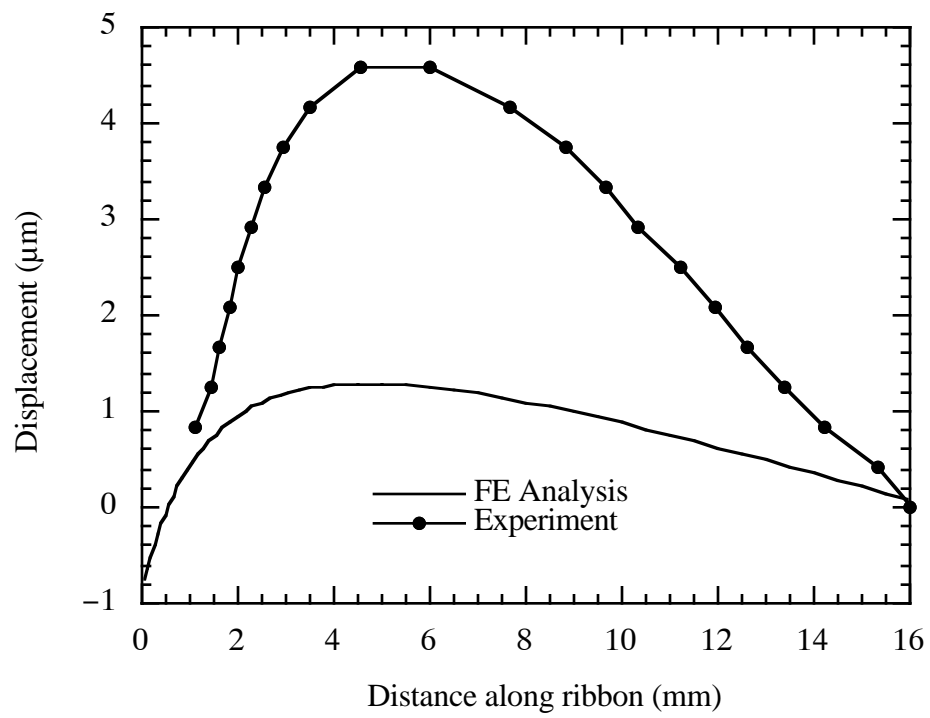


Figure 6.6. Comparison of experimental and finite element displacement profiles at a steady state temperature of 44°C.

occurred during the processing of the sample for the moiré experiments but was not accounted for in the FE model. Incorporating the debond in the model would move the location of the local maximum in the predicted displacement curve closer to that of the experiment.

The local maximum and the positive slope in displacement near the edge indicate that significant SMA actuation occurs in this region. Most of the actuation is restricted to the edge, and very little SMA effect is observed near the center of the sample. As discussed in Chapter 5, lower axial stress near the ends of the ribbon causes a smaller shift in the transformation temperatures, facilitating greater actuation. Therefore, the FE displacement profile captures most of the features of the SMA actuation in the ribbon composite although there is a large discrepancy in the magnitudes of displacements.

Several possible reasons exist for the differences in the magnitudes of the FE solution and the experimental displacement profiles. First, a 1-D model SMA constitutive model was adapted to a 2-D plane stress problem. Some loss of accuracy would be expected with this approximation. The experimental data and the 1-D model will eventually be compared with a fully 3-D model for SMA composites being developed by Qidwai and Lagoudas (1997). Preliminary results, however, indicate similarity with the 1-D solution developed. Further, the temperature to which the matrix is heated is around 10°C below the T_g of the epoxy and hence there is a possibility of viscoelastic relaxation that was not included in the model. Finally, the stress–temperature coefficient C_A of the SMA ribbon was obtained from the literature (Dye, 1990) and may not be accurate for the ribbon. In the experiments, the temperature measurements were made at the sample surface. Actual ribbon temperatures are probably higher than the measured values. Thermocouples could not be placed on the ribbon itself since it was resistively heated and the current drawn by the thermocouple would alter the measured temperatures.

A parametric study was carried out to investigate the influence of the ribbon temperature and the stress–temperature coefficient C_A . First, the temperature of the wire was varied while C_A was held constant at a literature value of 13.5 MPa/°C (Dye, 1990). The displacement and stress profiles were calculated for different temperatures. Figure 6.7 shows the displacement profiles with variation in temperature. The displacements are highly sensitive to change in temperature. The displacement along the entire ribbon is positive at $T = 42^\circ\text{C}$ indicating that at this temperature, thermal expansion dominates the sample response. By $T = 48^\circ\text{C}$, the entire displacement is negative indicating a predominance of the shape memory effect. The moiré displacement at $T = 44^\circ\text{C}$ again differs considerably in magnitude from the theoretical prediction. Although a uniform prestrain was applied to the ribbon prior to embedding, greater transformation is observed near the edge of the sample with rise in temperature.

The effect of change in steady state temperature on the stresses was also examined. In Chapter 4, a 5.2 MPa Tresca stress ($|\sigma_1 - \sigma_2|$) contour was obtained using photoelasticity. The variation with temperature of the predicted 5.2 MPa stress contour is shown in Figure 6.8 along with the contour from experiment at steady state ($t = 240\text{s}$). The stress contours were also very sensitive to increase in temperature. The contours move further away from the ribbon and also towards the center of the sample with increasing temperature. The point on the contours that is furthest from the ribbon (for example, point A on the at $T = 48^\circ\text{C}$ contour) is closer to the edge of the sample in the theoretical predictions. Adding a 1 mm debond at the edge of the sample would shift the location of this point closer to the experimental curve. The stress contour at $T = 48^\circ\text{C}$ is the closest to the experimental stress contour with a surface temperature of 44°C .

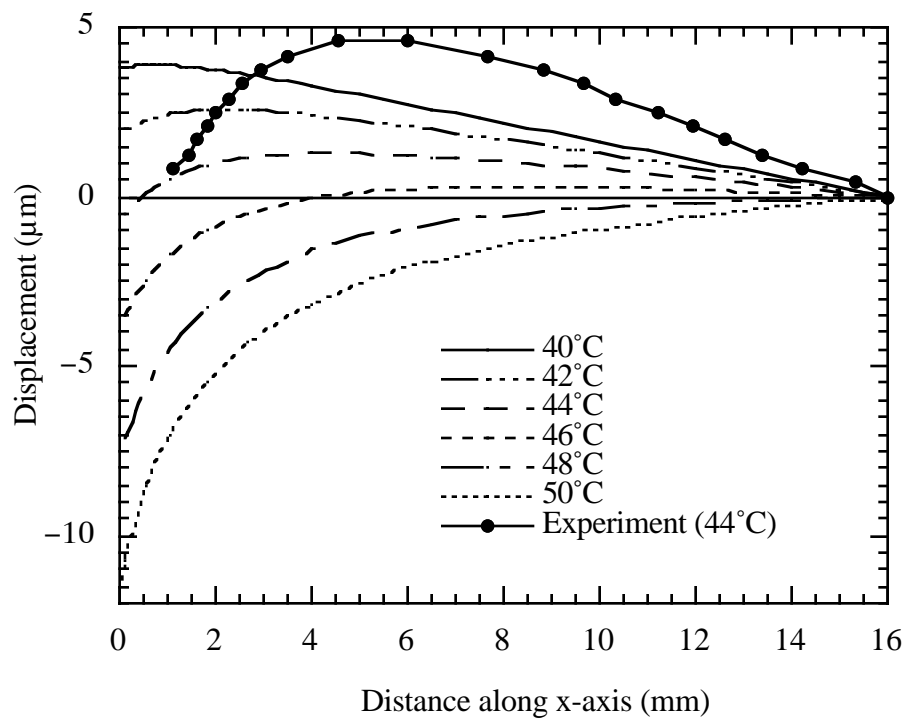


Figure 6.7. Displacement profiles along SMA ribbon for different steady state temperatures.

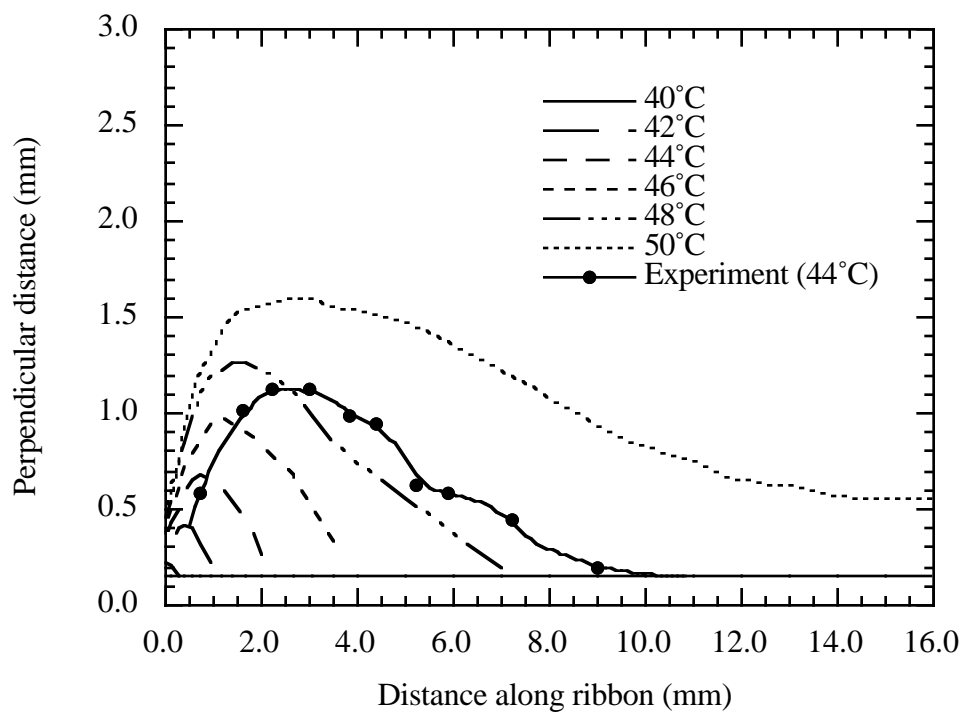


Figure 6.8. Stress contours along SMA ribbon for different steady state temperatures.

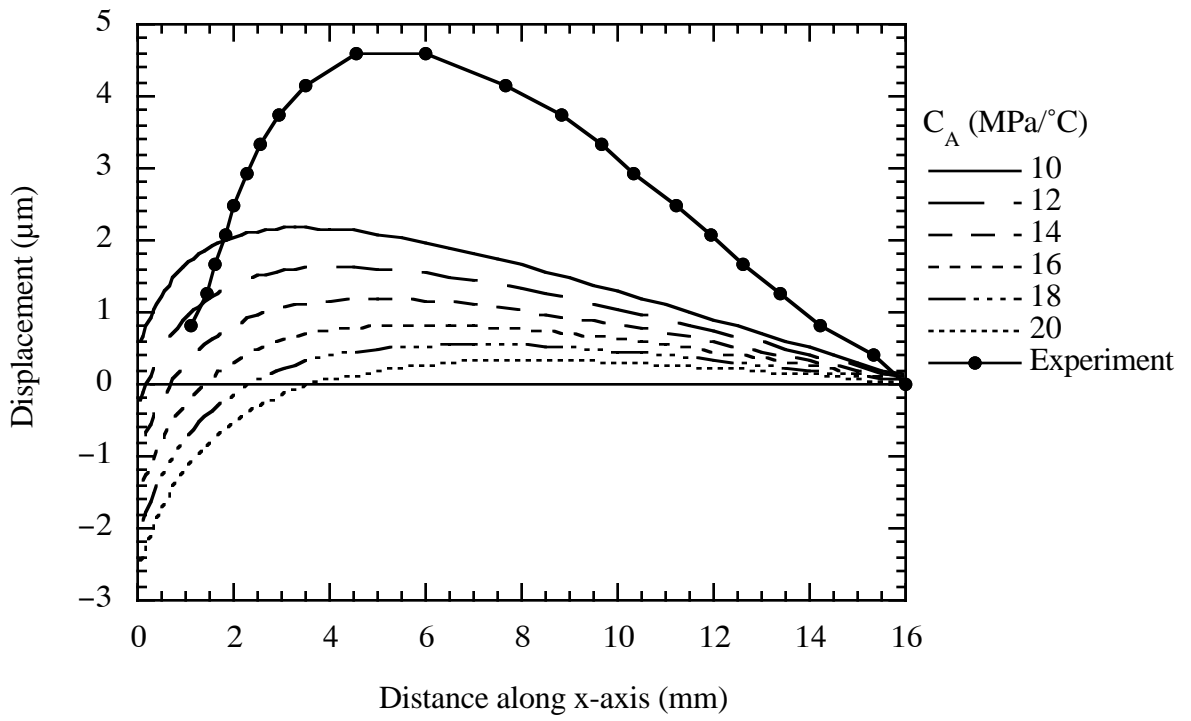


Figure 6.9. Displacement profiles along SMA ribbon for different stress–temperature coefficients.

Next, the value of C_A was varied, holding the steady state temperature at 44°C. The corresponding displacement profiles are shown in Figure 6.9. The response to changes in C_A is similar to that due to changes in temperature. Increasing C_A resulted in larger SMA transformation, indicated by increasing negative displacements. An examination of the cosine term in Equation (6.20) explains this behavior. The argument of the cosine term, given by

$$T - A_s - \frac{\sigma}{C_A} \quad (6.23)$$

denotes the effective difference in temperature above A_s . If the stress is zero, (6.23) would simply indicate the change in temperature above A_s , which governs the amount of transformation. An increase in stress is equivalent to a decrease in effective temperature. The stress and temperature are related through the stress–temperature coefficient C_A . For a given stress value, a larger C_A results in a smaller value of σ/C_A , thereby increasing the effective temperature. An increase in C_A is thus equivalent to an increase in the effective temperature, which causes greater actuation. As expected, the effect of C_A on stresses was again similar to the effect of temperature. Since no further insight was gained by the examination of these stress contours, they are not reported here.

The effect of change in the coefficient of thermal expansion α on the ribbon displacements was also examined. Displacement profiles along the ribbon for different values of α are shown in Figure 6.10. As α increases, a greater portion of the ribbon exhibits positive displacement, indicating that the thermal expansion becomes more significant. However, the effect of change in α on the displacement magnitudes is relatively small when compared to the effect of change in temperature. For example, when the value of α is doubled from $5 \mu\epsilon/^\circ\text{C}$ to $10 \mu\epsilon/^\circ\text{C}$, the displacement at the edge of the sample changes from $-1.91 \mu\text{m}$ to $-1.58 \mu\text{m}$. For comparison, Figure 6.8 shows

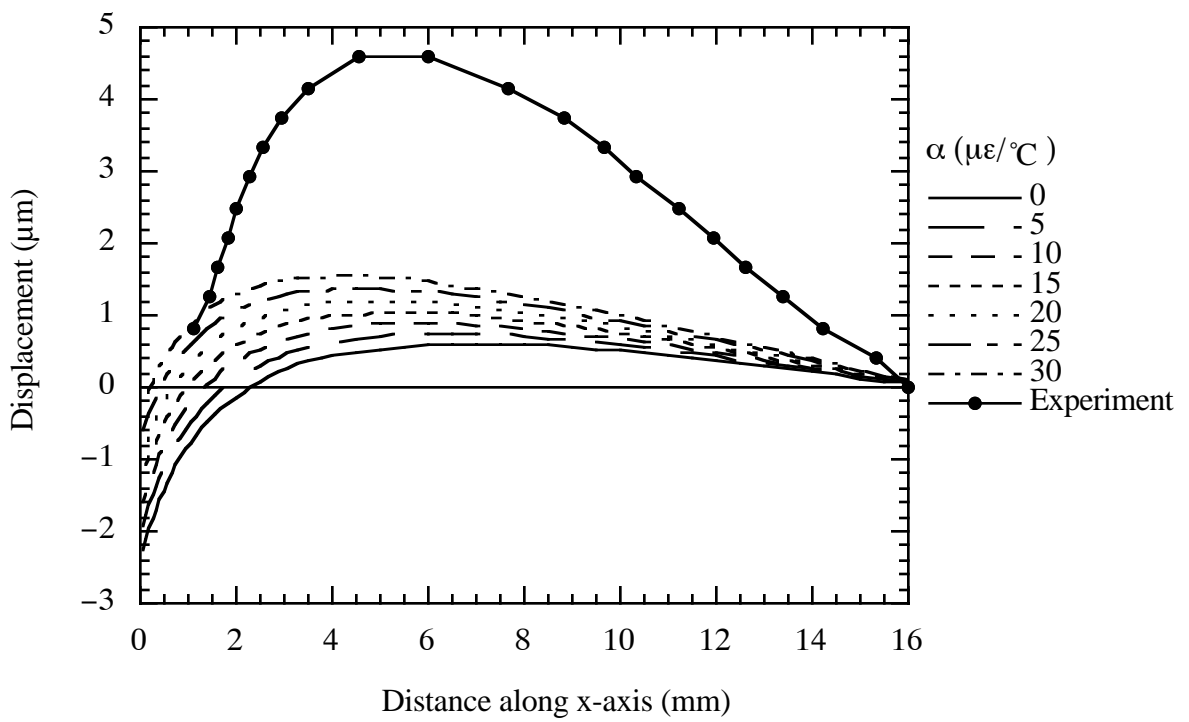


Figure 6.10. Displacement profiles along SMA ribbon for different values of the coefficient of thermal expansion.

that a 2°C change in temperature from 42°C to 44°C causes the edge displacement value to change from +1.87 μm to -0.75 μm.

The parametric studies described above indicate that the temperature of the ribbon has the most effect on the transformation, among the parameters considered. Material properties have a smaller, but still significant effect on sample response. It is therefore important to have accurate measurements of the ribbon temperature and material properties. The temperature profiles shown in Figure 5.8 were measured on the surface of the sample at a distance of approximately 0.1 mm from the embedded ribbon. Actual ribbon temperatures are probably higher. It was not possible to place a thermocouple directly on the ribbon since the current supplied for resistive heating affected the measured temperatures.

Among the material properties of the SMA listed in Table 4.1, the four transformation temperatures were obtained using a differential scanning calorimeter and the CTE for austenite was measured with a thermomechanical analyzer (TMA). The modulus E , the Poisson's ratio ν , the thermal conductivity K and the density ρ were obtained from literature (Dye, 1990) for an SMA with composition similar to that of the ribbons used in the experiments. Measurement of material properties such as the moduli and thermal conductivity for thin ribbons or wires is not straightforward. Further experiments are needed to accurately measure these properties. Accurate material property measurements are essential for the development and evaluation of SMA composite models.

6.5 Conclusions

A modified 1-D constitutive equation based on the model developed by Liang and Rogers (1990) was constructed. A finite element solution was developed to model the response of an SMA ribbon in a room temperature cured polymer composite and compared

with experimental values of displacements and stresses. The model captured most of the features of shape memory actuation, although large differences were observed in the actual magnitudes of the displacement and stress at a given temperature.

A parametric study was conducted to determine the sensitivity of the sample response to change in the ribbon temperature, the stress–temperature coefficient C_A , and the coefficient of thermal expansion α . The response was found to be highly sensitive to change in steady state temperature both for displacements and stresses. Increasing the temperature resulted in greater actuation of the SMA ribbon. Larger values of stress–temperature coefficient also resulted in greater actuation, although the sample response was less sensitive. Lower values of α also resulted in increased SMA displacements.

7. CONCLUSIONS AND FUTURE WORK

The behavior of Ni–Ti shape memory alloys embedded in a polymer matrix was investigated. Several different experimental techniques were utilized to measure the transient displacements and stress profiles of SMA wires or ribbons in epoxy matrices. A finite element model based on a one-dimensional constitutive equation was developed. Model predictions were compared to experimental data. This chapter outlines the major conclusions from the thesis and recommends possible areas of future work.

7.1 Conclusions

Interfacial debond strength of SMA wires embedded in an epoxy matrix were measured using pullout tests. Experimental data indicated that the interfacial bond between the SMA wire and the polymer matrix was largely due to mechanical rather than chemical bonding. Increasing the surface roughness of the wire was the only method that effectively raised the bond strength. Sandblasting the wires induced a significant increase in the bond strength while handsanding and acid etching actually decreased it. Silane coatings did not have a significant effect on the bond strength, and a plasma coating reduced the adhesion slightly.

In-situ out-of-plane displacements of two-way trained SMA wires in epoxy were measured using heterodyne microinterferometry. Experiments with 150 μm SMA wires in polymers indicated that thermal expansion occurs much faster than SMA actuation for the geometry and loading conditions considered. The interfacial bond strengths from pullout tests were correlated with maximum wire displacements. The smallest displacements were measured for sandblasted wires, which exhibited the highest interfacial bond strength. The largest displacement was observed for the acid etched wires, which had the lowest bond

strength. The host matrix imposed a greater restraint on the wire with increasing bond strength, causing a decrease in the wire displacement.

The transient load transfer behavior of a one-way SMA ribbon in a room temperature cured polymer matrix was quantified using two-dimensional photoelasticity. For high temperature cure matrices, annealed SMAs had lower residual stresses when compared with as received SMA, and aluminum samples. The stress applied by the matrix on the annealed ribbon during cooling converts some of the austenite to martensite, changing the length of the ribbon slightly. This results in lower residual stresses in the matrix for annealed SMA composites. Only qualitative data could be obtained for SMAs in high temperature cure matrices due to difficulty in separating the residual stress fringes from the fringes due to actuation.

Transient stress profiles were obtained for annealed SMA ribbons and 1% prestrained SMA ribbons embedded in a room temperature cure matrix. The stress contours were quantified and plotted for different time intervals. Actuation of annealed SMA ribbons indicated that the stresses due to thermal expansion were much lower than the stresses induced due to the shape memory effect. Photoelastic fringes due to actuation originated near the edge of the sample and moved inward toward the center as the sample was heated. The simple sample geometry along with the transient stress and temperature data provide an ideal benchmark for evaluating theoretical models.

Moiré interferometry was utilized to obtain the whole-field in-plane displacements of SMA ribbons embedded in a polymer matrix. Displacements of annealed ribbon samples compared well to a steady state finite element solution. Actuation of 1% prestrained SMA ribbons showed that most of the phase transformation was restricted to a region close to the edge of the sample. Residual fringes were observed in the sample after

cooldown, indicating one-way transformation. The outermost residual fringe indicated the location of a phase transformation front upon cooldown. The location of the saddle point at steady state temperature matched the location of the outermost fringe in the sample after cooldown, indicating that the saddle point might represent the location of a phase transformation front during actuation.

Increasing the power input to the sample resulted in only a small movement of the transformation front but induced further transformation in the partially transformed region between the edge of the sample and the actuation front. Comparison of SMA displacements at steady state with residual SMA displacements after cooldown indicated that some of the martensite transformed to austenite during heatup might be transforming back to martensite upon cooling due to the tensile stress induced by the constraint of the matrix on the ribbon.

Transient moiré measurements showed that displacements due to thermal expansion occurred before SMA displacements due to SMA actuation, for the configuration and power input levels considered. The motion of the fringes indicated that the SMA actuation front originates near the edge of the samples and moves inward towards the center as the sample is heated. The edge-to-center movement of the moiré fringes was similar to the movement of the stress contours in the photoelastic experiments. An experimental value for the velocity of the phase transformation front was calculated by tracking the location of the saddle point. For a current input of 1.50 A, the transformation front had an initial velocity of 25 $\mu\text{m/s}$ which tapered off to 2.4 $\mu\text{m/s}$ as equilibrium was reached.

A one-dimensional constitutive equation based on work by Liang and Rogers (1990) was adapted to model the SMA behavior. Finite element analysis was employed to model the response of an SMA ribbon in a room temperature cured polymer composite and

compared with experimental values of displacements and stresses. The model captured the main features of shape memory actuation observed in the experiments, such as actuation being restricted to the edge of the sample for low power inputs and increasing actuation near the center for higher power inputs. However, large differences were observed in the actual magnitudes of the displacement and stress at a given temperature. For example, for a current input of 1.50 A, the maximum displacement from the moiré experiments was 4 μm while the FE solution predicted a maximum displacement of only 2.2 μm .

A parametric study was conducted to determine the sensitivity of the sample response to change in ribbon temperature, the stress–temperature coefficient C_A , and the coefficient of thermal expansion α . The response was found to be highly sensitive to change in steady state temperature both for displacements and for stresses. Increasing the temperature resulted in greater actuation of the SMA ribbon. Larger values of stress–temperature coefficient also resulted in greater actuation, although the sample response was less sensitive. Higher values of α caused a decrease SMA displacements. Accurate measurements of SMA properties, such as the stress–temperature coefficient and the coefficient of thermal expansion are needed to improve predictions of SMA composite response.

7.2 Future Work

Aspects of shape memory alloy research that were addressed in this thesis include interfacial adhesion, load transfer, local displacements, and rate of actuation. Quantitative load transfer and displacement data were obtained for room temperature cure composites. There are many more unresolved issues regarding the behavior of embedded shape memory alloys. Some possible extensions of the current work are described briefly in this section.

Many applications involve SMAs embedded in high temperature cure matrices. Quantitative experimental data regarding the behavior of embedded SMAs in high temperature cure matrices are lacking in the literature. Moiré interferometry was utilized to obtain whole-field displacement measurements of room temperature cured SMA ribbon composites. It might be possible to apply the moiré technique to obtain quantitative displacement measurements of high temperature cure composites also. The same sample geometry could be retained but high temperature gratings are required. An additional advantage with high temperature cured samples is that they can be heated well above the austenite finish temperature without relaxing the matrix.

One of the long term objectives of the U.S. Navy, which partly funded this research work, is to embed SMA wires in the wing of fighter aircraft to provide active shape control of the wing surface. Most advanced aircraft wing panels are made of advanced composites, such as graphite/epoxy. A logical extension to the study of SMAs in pure polymers would be the study of SMAs in a composites such as graphite/epoxy. The graphite/epoxy matrix is cured at elevated temperatures. Therefore, quantitative data for behavior of SMAs in high temperature cured materials are essential for designing a SMA/graphite/epoxy smart composite system.

Another area of active research in SMA composites is the development of constitutive models to predict material behavior. Apart from the simple one-dimensional formulation adopted in the present work, only the model of Qidwai and Lagoudas (1997) is available for prediction of SMA composite response. Accurate predictions of material response are necessary for designing a smart composite.

In all the experiments discussed in this thesis, the SMA wires or ribbons were thermally actuated. As discussed previously, there is an equivalence between stress and

temperature for shape memory alloys. A higher stress equals a lower temperature, both stabilizing martensite. Therefore, SMA materials can also be actuated mechanically, and phenomena such as the pseudoelastic effect can be employed to actuate SMA composites. Further, the current work examines only the micromechanical response of SMA composites. This micromechanical behavior needs to be correlated with the macromechanical response of the composite in order to facilitate the design of complex SMA composite structures such as aircraft wing panels.

BIBLIOGRAPHY

ASM Metals Handbook, 1990, *Selection and Material Properties: Non-Ferrous Alloys and Special-Purpose Materials*, **2**, pp. 153-154.

Abeyaratne, R., and Knowles, J. K., 1991, Kinetic Relations and the Propagation of Phase Boundaries in Solids, *Archive of Rational Mechanics*, **114**, pp. 119-154.

Baz, A., and Ro, J., 1992, Thermo-Dynamic Characteristics of Nitinol Reinforced Composite Beams, *Composites Engineering*, **2**(5-7), pp. 527-542.

Bellesis, G. H., Harlice P. S., Renema, A., and Lambeth, D. N., 1993, Magnetostriction Measurement by Interferometry, *IEEE Transactions on Magnetics*, **29**(6), pp. 2989-2991.

Berveiller, M., Patoor, E., and Buisson, M., 1991, Thermomechanical Constitutive Equations for Shape Memory Alloys, *Journal de Physique IV*, Colloque C.4,387, European Symposium on Martensitic Transformation and Shape Memory Properties.

Buehler, W. J., Gilfritch, J. V., and Riley, R. C., 1963, Effect of Low-Temperature Phase Changes on the Mechanical Properties of Alloys Near Composition of TiNi, *Journal of Applied Physics*, **34**, pp. 1475-1477.

Bidaux, J. E., Bataillard, L., Manson, J. A., and Gotthardt, R., 1993, Phase Transformation Behavior of Thin Shape Memory Alloy Wires Embedded in a Polymer

Matrix Composite, Proceedings of 3rd European Conf. on Advanced Materials and Processes, pp. 1-5.

Boyd, J. G., and Lagoudas, D. C., 1995a, A Thermodynamical Constitutive Model for Shape Memory Materials. 1. The Monolithic Shape Memory Alloy, *International Journal of Plasticity*, **12**(6), pp. 805-842.

Boyd, J. G., and Lagoudas, D. C., 1995b, A Thermodynamical Constitutive Model for Shape Memory Materials. 2. The SMA Composite Material, *International Journal of Plasticity*, **12**(7), pp. 843-873.

Brinson, L. C., 1993, One-Dimensional Constitutive Behavior of Shape Memory Alloys: Thermomechanical Derivation with Non-Constant Material Functions, *Journal of Intelligent Material Systems and Structures*, **4**(2), pp. 229-242.

Chaudry, Z., and Rogers, C., 1991, Response of Composite Beams to an Internal Actuator Force, Proceedings of the 32nd Smart Structures and Materials Conference, AIAA-91-1166-CP, pp. 186-193.

Chua, P. S., and Piggott, M. R., 1985, The Glass Fibre-Polymer Interface: II—Work of Fracture and Shear Stresses, *Composites Science and Technology*, **22**, pp. 107-119.

Dally J. W., and Riley F. W., 1991, *Experimental Stress Analysis*, 3rd ed., McGraw-Hill, New York.

Drzal, L. T., Rich, M. J., Camping, J. D., and Park, W. J., 1980, Interfacial Shear Strength and Failure Mechanisms in Graphite Fiber Composites, 35th Annual Technical Conference, Reinforced Plastics/Composites Institute.

Drzal, L. T., Rich, M. J., and Lloyd, P. F., 1982, Adhesion of Graphite Fibers to Epoxy Matrices, *Journal of Adhesion*, **16**, pp. 133-145.

Dye, T. E., 1990, An Experimental Investigation of the Behavior of Nitinol, M.S. Thesis, Department of Engineering Science and Mechanics, Virginia Polytechnic Institute and State University.

Falk, F., 1980, Model Free Energy, Mechanics, and Thermodynamics of Shape Memory Alloys, *Z. Physik B*, **54**, pp. 1773-1780.

Goldstein, D., Kabacoff, L., and Tydings, J., 1981, Stress Effects on Nitinol Phase Transformations, *Journal of Metals*, pp. 19-26.

Hebda, D. A., Whitlock M. E., Ditman J. B., and White, S. R., 1995, Manufacturing of Adaptive Graphite/Epoxy Structures with Embedded Nitinol Wires, *Journal of Intelligent Materials and Smart Systems*, **6**(2), pp. 220-228.

Ivshin, Y., and Pence, T. J., 1994, A Constitutive Model for Hysteretic Phase Transition Behavior, *International Journal of Engineering Science*, **32**(4), 681-704.

Jackson C. M., Wagner, H. J., and Wasilewski, R.J., 1963, 55-Nitinol—The Alloy with a Memory: Its Physical Metallurgy, Properties, and Applications, NASA SP-5110.

Laughner, J. W., Shaw, N. J., Bhatt, R. T., and Dicarolo, J. A., 1988, Simple Indentation Method for Measurement of Interfacial Shear Strength in SiC/Si₃N₃ Composites, *Ceramics Engineering and Science Proceedings*, **7**, pp. 932-945.

Leo, P. H., Shield, T. W., and Bruno, P., 1993, Transient Heat Transfer Effects on Pseudoelastic Behavior of Shape Memory Alloy Wires, *Acta Metallurgica*, **41**, pp. 2477-2485.

Li, L., Durkin, K., and Sottos, N. R., 1994, The Influence of Interface/Interphase Regions on the Performance of Piezocomposites, The American Society for Composites, Ninth Technical Conference, Newark, Delaware, Technomic Publishing Company Inc., pp. 5-12.

Liang C., Jia, J., and Rogers, C., 1989, Behavior of Shape memory Alloy Reinforced Composite Plates Part II: Results, Proceedings of the 30th Structures, Structural Dynamics and Materials Conference, AIAA-89-1331-CP, pp. 1504-1513.

Liang C., and Rogers, C., 1990, One-Dimensional Thermomechanical Constitutive Relations for Shape Memory Materials, *Journal of Intelligent Material Systems and Structures*, **1**(2), pp. 207-234.

Ling, H. C., and Kaplow, R., 1981, Variation in the Shape Recovery Temperature in NiTi Alloys, *Material Science and Engineering*, **48**(2), pp. 241-247.

MacLaughlin, T. F., 1968, A Photoelastic Analysis of Fiber Discontinuities in Composite Materials, *Journal of Composite Materials*, **2**(1), 44-55.

Melton, K. N., 1989, Ni-Ti Based Shape Memory Alloys, in *Engineering Aspects of Shape Memory Alloys*, ed. Deurig, T. W., Melton, K. N., Stockel, D., and Wayman, C.M., Butterworth-Heinemann, Boston, pp. 21-35.

Miller, B., Muri, P., and Rebenfield, L., 1987, A Microbond Method for Determination of Shear Strength of a Fiber/Resin Interface, *Composites Science and Technology*, **28**, pp. 17-32.

Miyazaki, S., 1989, Thermal and Stress Cycling Effects and Fatigue Properties of Ni-Ti Alloys, in *Engineering Aspects of Shape Memory Alloys*, ed. Deurig, T. W., Melton, K. N., Stockel, D., and Wayman, C.M., Butterworth-Heinemann, Boston, pp. 394-413.

Müller, I., 1989, On the size of hysteresis in Pseudoelasticity, *Continuum Mechanics and Thermodynamics*, **1**, pp. 125-142.

Ortin, J., 1992, Preisach Modeling of Hysteresis for a Pseudoelastic Cu-Zn-Al Single Crystal, *Journal of Applied Physics*, **71**(3), pp. 1454-1461.

Otsuka, K., Introduction to the R-Phase Transition, in *Engineering Aspects of Shape Memory Alloys*, ed. Deurig, T. W., Melton, K. N., Stockel, D., and Wayman, C.M., Butterworth-Heinemann, Boston, pp. 36-45.

Paine, J. S. N., and Rogers, C. A., 1991, The Effect of Thermoplastic Composite Processing on the Performance of Embedded Nitinol Actuators, *Journal of Thermoplastic Composite Materials*, **2**(4), pp. 102-122.

Paine, J. S. N., Jones, W. M., and Rogers, C. A., 1992, Nitinol Actuator to Host Composite Interfacial Adhesion in Adaptive Hybrid Composites, Proceedings of the 33rd Structures, Structural Dynamics and Materials Conference, AIAA-92-2405-CP, pp. 556-565.

Paine, J. S. N., and Rogers, C. A., 1993, Characterization of Interfacial Shear Strength Between SMA Actuators and Host Composite Material in Adaptive Composite Material Systems, *Adaptive Structures and Material Systems*, ASME AD-35, pp. 63-70.

Patoor, E., Eberhardt, A., and Berveiller, M., On Micromechanics of Thermoelastic Phase Transition, Fourth International Symposium on Plasticity and its Applications, Baltimore, Md., July 19-23.

Pego, R., 1987, Phase Transitions in One-Dimensional Nonlinear Viscoelasticity: Admissibility and Stability, *Archive of Rational Mechanics*, **97**, pp. 353-394.

Penn, L. S., Bystry, F., and Marchionni, H. J., 1983, Relation of Interfacial Adhesion in Kevlar/Epoxy Systems to Surface Characterization and Composite Performance, *Polymer Composites*, **4**, pp. 26-31.

Penn, L. S., and Lee, S. M., 1989, Interpretation of Experimental Results in the Single Pull-out Filament Test, *Journal of Composites Science and Technology*, **11**(1), pp. 23-30.

Perkins J., and Hodgson, G., 1989, The Two-Way Shape Memory Effect, in *Engineering Aspects of Shape Memory Alloys*, ed. Deurig, T. W., Melton, K. N., Stockel, D., and Wayman, C.M., Butterworth-Heinemann, Boston, pp. 195-206.

Piggot, M. R., Chua, P. S., and Andison, D., 1985, The Interface between Glass and Fibers and Thermosetting Polymers, *Polymer Composites*, **6**(4), pp. 242-248.

Piggot, M. R., 1991, Failure Processes in Fiber-Polymer Interphase, *Composite Science and Technology*, **46**(1), pp. 56-76.

Post, D., Han, B., and Ifju, P., 1994, *High Sensitivity Moiré*, Springer-Verlag, New York

Ryan, M. J., Scott, W. R., and Sottos, N. R., 1990, *Review of Progress in Quantitative Nondestructive Evaluation*, Plenum Press, New York.

Schuerch, H. U., 1968, Certain Physical Properties and Applications of Nitinol, NASA Cr-1232, NTIS N 69-11420, pp. 1-23.

Shaw, J. A., and Kyriakides, S., 1995, Thermomechanical Aspects of NiTi, *Journal of Mechanics and Physics of Solids*, **43**(8), pp. 1243-1281.

Sottos, N. R., Scott, W. R., and McCollough, R. L., 1991, Micro-Interferometry for Measurement of Thermal Displacements at Fiber/Matrix Interfaces, *Journal of Experimental Mechanics*, **31**(2), pp. 98-103.

Sottos, N. R., Kline, G. E., Qidwai, M. A., and Lagoudas, D. C., 1996, Analysis of Phase Transformation Fronts in Embedded Shape Memory Alloy Composites, Proceedings of SPIE Mathematics and Control in Smart Structures, pp. 25-29.

Sun, Q. P., and Hwang, K. C., 1993a, Micromechanics Modelling for the Constitutive Behavior of Polycrystalline Shape Memory Alloys—I. Study of the Individual Phenomena, *Journal of Mechanics and Physics of Solids*, **41**(1), pp. 1-18.

Sun, Q. P., and Hwang, K. C., 1993b, Micromechanics Modelling for the Constitutive Behavior of Polycrystalline Shape Memory Alloys—II. Derivation of General Relations, *Journal of Mechanics and Physics of Solids*, **41**(1), pp. 19-31.

Tanaka, K., 1986, A Thermomechanical Sketch of Shape Memory Effect—One-Dimensional Tensile Behavior, *Acta Mechanica*, **18**, pp. 251-263.

Tyson W. R., and Davies G. J., 1965, A Photoelastic Analysis of the Shear Stresses Associated with the Transfer of Stress During Fibre Reinforcement, *British Journal of Applied Physics*, **16**, pp. 199-205.

Wake, W. C., 1978, Theories of Adhesion and Uses of Adhesives: A Review, *Polymer*, **19**, pp. 291-308.

Wayman, C. M., 1989, An Introduction to Martensite and Shape Memory, in *Engineering Aspects of Shape Memory Alloys*, ed. Deurig, T. W., Melton, K. N., Stockel, D., and Wayman, C.M., Butterworth-Heinemann, Boston, pp. 3-20.

Xu, Z. R., and Ashbee, K. H. G., 1994, Photoelastic Study of the Durability of Interfacial Bonding of Carbon Fibre-Epoxy Resin Composites, *Journal of Materials Science*, **29**, 394-403.

VITA

Krishna D. Jonnalagadda was born on September 4th, 1969, in Vishakhapatnam, India. He completed his high school studies at the Hyderabad Public School – Ramanthapur, Hyderabad, in 1987. He joined the Institute of Technology, Banaras Hindu University, in 1987 and graduated with a bachelor's degree in Mechanical Engineering in 1991. He completed his M.S. degree in Engineering Mechanics at the University of Kentucky, Lexington, in August 1993. The same year, he entered the doctoral program in the Department of Theoretical and Applied Mechanics at the University of Illinois at Urbana-Champaign, where he worked under the guidance of Prof. Nancy R. Sottos. He has been hired by the Materials Reliability Laboratory at the Motorola Corporate Research Center and will be relocating to Schaumburg, Ill., in September 1997.